

**Kinetics and Transport Phenomena in the Chemical Decomposition of  
Copper Oxychloride in the Thermochemical Cu-Cl Cycle**

By

Gabriel D. Marin

A Thesis Submitted in Partial Fulfillment  
of the Requirements for the Degree of  
Doctor of Philosophy in Mechanical Engineering  
in  
The Faculty of Engineering and Applied Sciences  
University of Ontario Institute of Technology

April 2012

© Gabriel Marin, 2012

## Abstract

---

The thermochemical copper-chlorine (Cu-Cl) cycle for hydrogen production includes three chemical reactions of hydrolysis, decomposition and electrolysis. The decomposition of copper oxychloride establishes the high-temperature limit of the cycle. Between 430 and 530 °C, copper oxychloride ( $\text{Cu}_2\text{OCl}_2$ ) decomposes to produce a molten salt of copper (I) chloride (CuCl) and oxygen gas. The conditions that yield equilibrium at high conversion rates are not well understood. Also, the impact of feed streams containing by-products of incomplete reactions in an integrated thermochemical cycle of hydrogen production are also not well understood. In an integrated cycle, the hydrolysis reaction where  $\text{CuCl}_2$  reacts with steam to produce solid copper oxychloride precedes the decomposition reaction. Undesirable chlorine may be released as a result of  $\text{CuCl}_2$  decomposition and mass imbalance of the overall cycle and additional energy requirements to separate chlorine gas from the oxygen gas stream.

In this thesis, a new phase change predictive model is developed and compared to the reaction rate kinetics in order to better understand the nature of resistances. A Stefan boundary condition is used in a new particle model to track the position of the moving solid-liquid interface as the solid particle decomposes under the influence of heat transfer at the surface. Results of conversion of  $\text{CuO} \cdot \text{CuCl}_2$  from both a thermogravimetric (TGA) microbalance and a laboratory scale batch reactor experiments are analyzed and the rate of endothermic reaction determined. A second particle model identifies parameters that impact the transient chemical decomposition of solid particles embedded in the bulk fluid

consisting of molten and gaseous phases at high temperature and low Reynolds number. The mass, energy, momentum and chemical reaction equations are solved for a particle suddenly immersed in a viscous continuum. Numerical solutions are developed and the results are validated with experimental data of small samples of chemical decomposition of copper oxychloride ( $\text{CuO} \cdot \text{CuCl}_2$ ). This thesis provides new experimental and theoretical reference for the scale-up of a  $\text{CuO} \cdot \text{CuCl}_2$  decomposition reactor with consideration of the impact on the yield of the thermochemical copper-chlorine cycle for the generation of hydrogen.

*To my wife*  
*Mimi*  
*and my beloved daughters*  
*Isabella and Valentina,*  
*for their unconditional patience and love*

## Acknowledgments

---

I look back to these great years at UOIT and I can only be grateful for all the great support and direction received. All these years have polished my spirit and made me a more conscious and learning oriented professional.

First, I want to acknowledge the professional and unconditional support received from my supervisors, Dr. Greg F. Naterer and Kamiel Gabriel. They have not only provided continuous guidance throughout my research, but also a reference to exemplary ethical values. This research could have not been possible without their continuous support and enthusiasm.

I also want to thank Dr. Zhaolin Wang for providing a stimulating and creative environment in addition to timely scientific insights in moments of difficult decisions. He promoted a scientific approach and professional perspective where learning experiences flourished.

This research also brought me close to great new friends from whom I am thankful for their support. Especially Dr. Venkata Daggupati had the patience to explain things clearly and repeat when necessary, helping me understand phenomena in the context of mathematical analysis. Also, thanks to my dear friend Dr. Juan Carlos Ramirez at Purdue University for being there whenever I needed direction. Their friendly support and patience made a difference in moments of uncertainty.

I also want to thank Ed Secnik for his commitment to a quiet and safe environment and call to discipline, and for his diligence with the lab infrastructure. His approach is a great reference for the future.

I am also very thankful with members of the committee, Dr. Ibrahim Dincer, and Dr. Liliana Trevani for the time and patience while reviewing my thesis and providing feedback when requested. Their input and direction brought additional meaning to this research. Similarly, I would like to thank you Dr. Antonio Mazza for volunteering his time as external reviewer of my thesis.

Thanks to Dr. Brad Easton for his kind support while facilitating his lab for a critical part of my experimental work with TGA, and for the timely training facilitated by Patrick Edge. Also, I could not have navigated successfully through the complexity of XRD analysis without the unconditional help from George Kretschmann at the Department of Geology of the University of Toronto. George made the learning experience enjoyable and efficient at all times.

Finally, my sincere thanks go to the people and organizations that support research at UOIT by providing critical financial resources. Support from the Natural Sciences and Engineering Research Council of Canada, the Ontario Research Fund, Atomic Energy of Canada Limited, and the Faculty of Engineering and Applied Science at UOIT are gratefully acknowledged.

# Table of Contents

Certificate of Approval.....	ii
Abstract.....	iii
Acknowledgments.....	vi
List of Figures.....	x
List of Tables.....	xv
Nomenclature.....	xvi
Chapter 1 – Introduction.....	1
<u>1.1</u> Background.....	1
<u>1.1.1</u> Hydrogen as an Energy Carrier.....	5
<u>1.1.2</u> Hydrogen from Thermochemical Cycles.....	11
<u>1.2</u> Motivation and Objectives of Thesis.....	14
Chapter 2 - Literature Review.....	16
<u>2.1</u> Thermochemical Cycles.....	16
<u>2.2</u> Thermochemical Cu-Cl Cycle.....	20
<u>2.3</u> Three Reactions Thermochemical Cu-Cl Cycle.....	27
<u>2.3.1</u> Electrolysis Reaction.....	27
<u>2.3.2</u> Hydrolysis Reaction.....	29
<u>2.3.3</u> Decomposition Reaction.....	33
<u>2.4</u> Experimental and Theoretical Models.....	38
<u>2.4.1</u> Moving Interface Models.....	39
<u>2.4.2</u> Chemical Reaction Models.....	43
<u>2.4.3</u> Experimental Data Fitting.....	46
<u>2.4.4</u> The Damkohler Number.....	50
<u>2.4.5</u> Momentum Analysis.....	51
<u>2.4.6</u> Dimensional Analysis.....	57
<u>2.5</u> Experimental Methods.....	58
<u>2.6</u> Uncertainty and Error.....	60
Chapter 3 – Experiments on the Decomposition Reactor.....	62
<u>3.1</u> Approaches to Experimental Work.....	62
<u>3.2</u> Experimental Apparatus and Set Up.....	63
<u>3.3</u> Chemicals and Materials.....	65
<u>3.4</u> Forward Reaction.....	67

<u>    </u> 3.5 Reverse Reaction.....	70
<u>    </u> 3.6 Uncertainty and Error.....	71
Chapter 4 - Model of the Decomposition Kinetics.....	80
<u>    </u> 4.1 Hydrolysis Reaction for Production of Copper Oxychloride.....	81
<u>    </u> 4.2 Thermodynamic Analysis of the Reverse Reaction .....	84
<u>    </u> 4.3 Copper Oxychloride Decomposition Reaction .....	93
<u>        </u> 4.3.1 Thermodynamic Equilibrium of the Decomposition Reaction.....	99
<u>    </u> 4.4 Experimental Rate of Reaction .....	102
Chapter 5 - Model of Moving Boundary Heat Transfer.....	107
<u>    </u> 5.1 Energy Equation.....	109
<u>    </u> 5.2 Dimensional Analysis .....	112
<u>    </u> 5.3 Resistances .....	114
Chapter 6 - Model of Thermochemical Decomposition.....	117
<u>    </u> 6.1 Physical Problem Description .....	117
<u>        </u> 6.1.1 Continuity Equation .....	117
<u>        </u> 6.1.2 Energy Equation.....	123
<u>        </u> 6.1.3 Momentum Equation.....	123
<u>        </u> 6.1.4 Boundary and Initial Conditions .....	125
<u>        </u> 6.1.5 Dimensional Analysis and Scaling.....	126
Chapter 7 - Results and Discussions .....	130
<u>    </u> 7.1 Pathways of Chemical Decomposition .....	130
<u>    </u> 7.2 Reversibility of Decomposition Reaction .....	150
<u>    </u> 7.3 Rate of Reaction.....	156
<u>    </u> 7.4 Phase Change Decomposition.....	169
<u>    </u> 7.5 Reactor Dynamics .....	173
Chapter 8 - Conclusions and Recommendations for Future Research .....	182
<u>    </u> 8.1 Conclusions.....	182
<u>    </u> 8.2 Recommendations for Future Research .....	187
References .....	189

## List of Figures

Fig. 1.1: World energy consumption projected to 2030 .....	3
Fig. 1.2: Weight and energy content of liquid fuels relative to liquid hydrogen.....	7
Fig. 1.3: Concentration range of flammability of hydrogen and conventional fuels in standard air at 25 °C and 1Atm.....	8
Fig. 2.1: Flow diagram of the three reaction thermochemical Cu-Cl cycle.....	25
Fig. 2.2: Typical path for thermodynamic calculations of reactions.....	36
Fig. 3.1: Experimental apparatus with vertical split reactor for chemical decomposition.....	65
Fig. 3.2: Experimental configuration for the reaction of molten CuCl and O <sub>2</sub> .....	69
Fig. 4.1: Paths for thermodynamic calculations of copper oxychloride.....	86
Fig. 4.2: Standard enthalpy ( $\Delta_r^T H^\theta$ ) and entropy ( $\Delta_r^T S^\theta$ ) of the reverse reaction at various temperatures.....	89
Fig. 4.3: Standard Gibbs free energy ( $\Delta_r^T G^\theta$ ) of the reverse reaction at various temperatures.....	90
Fig. 4.4: Gibbs free energy of CuCl + O <sub>2</sub> reaction at various operating conditions.....	91
Fig. 4.5: Vapour pressure of CuCl at various temperatures.....	92
Fig. 4.6: Gibbs energy of reactions of two pathways (path A in open markers) for decomposition of copper oxychloride at atmospheric pressure.....	96
Fig. 4.7: Effects of reactor pressure in the Gibbs energy of the copper oxychloride decomposition reaction.....	98

Fig. 5.1: Particle interface, species and temperature profiles during thermal decomposition.....	108
Fig. 7.1 Oxygen formation from decomposition of a 50 g. batch of $\text{CuO} \cdot \text{CuCl}_2$ at 570 °C and 1.003 atm.....	131
Fig. 7.2: Oxygen formation from decomposition of a 100 g. batch of $\text{CuO} \cdot \text{CuCl}_2$ at average temperature of 560 °C and 1.003 atm.....	132
Fig. 7.3: Oxygen formation from decomposition of a 100 g. batch of $\text{CuO} \cdot \text{CuCl}_2$ at average temperature of 530 °C and 1.003 atm.....	133
Fig. 7.4: Oxygen formation from decomposition of a 100 g batch of $\text{CuO} \cdot \text{CuCl}_2$ at average temperature of 490 °C and 1.003 atm.....	134
Fig. 7.5: Oxygen yield and $\text{CuCl}$ weight loss due to evaporation from samples of 100 g of $\text{CuO} \cdot \text{CuCl}_2$ at different temperatures.....	135
Fig. 7.6: Decomposition of $\text{CuO} \cdot \text{CuCl}_2$ in a semi-batch operation with a feed rate of 0.085 mol/min and average bath temperature of 490 °C.....	136
Fig. 7.7: Decomposition of $\text{CuO} \cdot \text{CuCl}_2$ in a semi-batch operation with a feed rate of 0.085 mol/min and average bath temperature of 510 °C.....	137
Fig. 7.8: Decomposition of $\text{CuO} \cdot \text{CuCl}_2$ in a semi-batch operation with a feed rate of 0.085 mol/min and average bath temperature of 530 °C.....	138
Fig. 7.9: Concentration of unreacted solids in molten salt at 490 °C vs. formation of molten $\text{CuCl}$ .....	139
Fig. 7.10: Concentration of unreacted solids in molten salt at 510 °C vs. formation of molten $\text{CuCl}$ .....	140

Fig. 7.11: Concentration of unreacted solids in molten salt at 530 °C with formation of molten CuCl.....	141
Fig. 7.12: Ratio of unreacted vs. fed CuO*CuCl <sub>2</sub> at several average temperatures of molten CuCl.....	142
Fig. 7.13: Partial pressure of chlorine at equilibrium with the decomposition of CuCl <sub>2</sub> . (Dokiya-Kotera at 92 mm Hg vs. Present study at atmospheric conditions).....	143
Fig. 7.14: Sample of products of copper oxychloride decomposition.....	146
Fig. 7.15: XRD Reflections of products of decomposition of copper oxychloride at 550 °C.....	147
Fig. 7.16: Equilibrium analysis of extent of reaction vs. experimental results for the decomposition of copper oxychloride at temperatures from 450 °C to 560 °C, and atmospheric pressure.....	148
Fig. 7.17: Theoretical evolution of residual chlorine from excess CuCl <sub>2</sub> using proposed mechanistic analysis of reactions vs. experimental results in the range of 450 °C to 560 °C; 1 mol/L oxygen, and atmospheric pressure.....	149
Fig. 7.18: XRD results of products of CuCl + O <sub>2</sub> at 450 °C, 1-hour test (experiment set #1 in Table 7.1).....	152
Fig. 7.19: XRD results of products of CuCl + O <sub>2</sub> at 500 °C, 1 hour test (experiment set #2 in Table 7.1).....	153
Fig. 7.20: XRD results of CuCl and O <sub>2</sub> at 500 °C, 1-hour test (experiment set #3 in Table 7.1).....	154
Fig. 7.21: Impurities in the CuCl reactant, molten at 500 °C (experiment set #4 in Table 7.1).....	155

Fig. 7.22: X-Ray diffraction analysis of a standard sample of stoichiometric CuO*CuCl <sub>2</sub> .....	156
Fig. 7.23: Proportion of solids from Rietveld quantification of XRD analysis. Samples of decomposition of CuO*CuCl <sub>2</sub> at different temperatures.....	157
Fig. 7.24: Measured weight percent of thermogravimetric decomposition vs. change of heat flow.....	159
Fig. 7.25: Stages of weight losses from TGA experiments during decomposition of samples of CuO*CuCl <sub>2</sub> at 430 °C.....	160
Fig. 7.26: Total experimental heat of decomposition of CuO*CuCl <sub>2</sub> and evaporation of CuCl, and energy of reaction of CuO chlorination as reported by Serban et al. ....	161
Fig. 7.27: Comparison of thermogravimetric decomposition of CuO*CuCl <sub>2</sub> at several temperatures.....	162
Fig. 7.28: Rate of reaction of CuO and Cl <sub>2</sub> vs. rate of release of Cl <sub>2</sub> from CuO*CuCl <sub>2</sub> (TGA experiments [44, 55]).....	163
Fig. 7.29: Reduced time plot of decomposition rates of CuO*CuCl <sub>2</sub> at 530 °C (TGA and batch reactor experiments).....	166
Fig. 7.30: Curve fitting of experimental data from conversion of CuO*CuCl <sub>2</sub> vs. time.....	167
Fig. 7.31: Curve fitting of conversion data at different temperatures.....	168
Fig. 7.32: Solid-liquid interface tracking for several Stefan numbers.....	170
Fig. 7.33: Rates of reaction compared to experimental data.....	171
Fig. 7.34: Solid particle shrinking radius and temperature profile for several initial diameters.....	174

Fig. 7.35: Impact of liquid temperature on the dynamics of decomposition for 0.5 mm particles.....	175
Fig. 7.36: Sensitivity to the differential of initial temperature of the solid particle and the molten continuum.....	176
Fig. 7.37: Effects of the difference of temperature between the particle and the continuum on the dynamics of decomposition.....	178
Fig. 7.38: Dynamics of reaction and concentration of solids for particles of 0.2 mm, at full conversion and average $\xi = 1$ .....	179
Fig. 7.39: Dimensionless residence time of decomposition of particles and experimental results of the normalized time at 50% conversion, versus average temperature of the molten medium.....	180
Fig. 7.40: Evolution of the overall Nusselt number as a result of varying radius of a particle of $\text{CuO} \cdot \text{CuCl}_2$ undergoing chemical decomposition.....	181

## List of Tables

Table 1.1: Physical properties of hydrogen, air and conventional fuels.....	6
Table 1.2: Traditional and novel methods for hydrogen production.....	12
Table 2.1: Summary of Ispra recommended thermochemical cycles.....	16
Table 2.2: Thermochemical cycles proposed for integration with nuclear reactors. Lewis et al. [30-32].....	19
Table 2.3: Proposed variations of the Cu-Cl cycle.....	21
Table 2.4: Processes and reactions in the thermochemical Cu-Cl cycle <sup>[44]</sup> .....	26
Table 3.1: Chemicals used in experiments.....	65
Table 3.2: Materials used in the vertical reactor.....	67
Table 3.3: Summary of measurement assumptions and uncertainties.....	72
Table 3.4: Enthalpy of formation of compounds in the Cu-Cl Cycle at 298.15 K.....	74
Table 3.5: Thermo-physical properties of species.....	75
Table 4.1: Gibbs equilibrium constants for potential decomposition paths.....	101
Table 6.1: Partial pressure of oxygen at equilibrium.....	122
Table 7.1: Experimental conditions for the reaction of copper (I) chloride and oxygen.....	151
Table 7.2: Weight losses measured in TGA experiments.....	165
Table 7.3: Deviation of conversion dependent terms with temperature ( $k_1$ ).....	169
Table 7.4: Conversion rates at different temperatures.....	172

## Nomenclature

a	Kinetics: Diameter [ $m$ ], Chemistry: Activity
A	Analyzer percent reading
$A_c$	Actual capacity [ $kg/h$ ]
B	Bias
b	Constant
C	Concentration [ $mol/m^3$ ]
c	Constant
$C_p$	Specific heat capacity [ $J/mol.K$ ]
$C_k$	Capital cost [ $\$$ ]
D	Diffusivity [ $m^2/s$ ]
d	Distance [ $m$ ], diameter [ $m$ ]
$Da$	Damkohler number = $\frac{Rr.\tau}{C_o}$ ; $\left(\frac{Rr.a^2}{C_o D_{sl}}\right)^{1/2}$
$D_p$	Distance from plant [ $km$ ]
$D_y$	Days of operation [ $days/year$ ]
E	Activation Energy [ $J/mol.K$ ]
F	Force [ $kg.m/s^2$ ], Flow [ $l/s$ ]
f	Thermodynamics: Fugacity , Concentration: Volume fraction
G	Gibbs free energy [ $J/mol$ ]
g	Gravity acceleration [ $m/s^2$ ]
H	Enthalpy [ $J/mol$ ]
$H_c$	Capital cost factor [ $\$/kg$ ]
$H_t$	Transportation cost factor [ $\$/kg$ ]

h	Thermodynamics: Latent heat [ $J/mol$ ], Numerical: Integration step
i	Interest rate [%]
j	Species
K	Equilibrium constant
k	Kinetics: Reaction rate constant, Numerical: Integration constant
Lew	Lewis number = $\frac{k}{D_{st}}$
L	Length [ $m$ ]
M	Chemistry: Molecular weight [ $kg/mol$ ], Kinetics: Mass [ $kg$ ]
m	Mass [ $kg$ ]
N	Nitrogen
n	Mols
O	Oxygen
P	Precision
P	Pressure [ $bar$ ], [ $Pa$ ]
Q	Reaction quotient
Pe	Peclet number = $\frac{Lu}{D}$ ; $\frac{Lu}{k}$
Pr	Reduced pressure [ $bar$ ]
Re	Reynolds number = $\frac{\rho Lu}{\mu}$
Rr	Rate of reaction [ $mol/m^3.s$ ]
Rh	Production rate [ $kg/h$ ]
R	Radius [ $m$ ], Ideal gas constant [ $J/mol.K$ ]
r	Numerical: Dimensionless radius, Kinetics: Rate of reaction

S	Molar entropy [ $J/mol.K$ ]
s	Tensor
Ste	Stefan number = $\frac{h_{sl}}{C_{ps}(T_o - T_m)}$
T	Temperature [ $K$ ]
Tr	Reduced Temperature [ $K$ ]
t	Time [ $s$ ]
t*	Dimensionless time = $\frac{\lambda}{\rho C_p} \frac{t}{a^2}$
u	Velocity [ $m/s$ ]
U*	Dimensionless velocity
U	Uncertainty
V	Volume [ $m^3$ ], constant
X	Species conversion
y	mol fraction, species
z	Variable
Z	Volumetric factor

### Greek Letters

$\alpha$	Stefan Number = $\frac{C_{ps}(T_o - T_m)}{h_{sl}}$
$\lambda$	Energy: Thermal Conductivity [ $W/m.K$ ], Spectrometry: Wavelength [ $m$ ]
$\Delta$	Delta
$\xi$	Thermal: Dimensionless temperature = $\frac{T_l - T_m}{T_o - T_m}$
	Kinetics: Extent of reaction

$\theta$	Energy: Dimensionless temperature = $\frac{T_s - T_m}{T_o - T_m}$ , Crystallography: Angle of scattering
$\Psi$	Dimensionless radius
$\varphi$	Fugacity coefficient
$\kappa$	Thermal diffusivity [ $m^2/s$ ]
$\eta$	Efficiency
$\sigma$	Parameter
$\mu$	Dynamic viscosity [ $kg/m.s$ ]
$\bar{\rho}$	Molar Density [ $mol/m^3$ ]
$\rho$	Density [ $kg/m^3$ ]
$\nu$	Momentum: Kinematic viscosity [ $m^2/s$ ], Chemistry: Stoichiometric coefficient

### Subscripts

D	drag
f	fluid
g	gas
i	initial condition
l	liquid
L	lift
m	mass, particle
n	new condition
o	initial, bulk
s	solid
T	thermal, total
V	virtual

## **Abbreviations**

ANL	Argon National Laboratories USA
CFD	Computational Fluid Dynamics
CANDU	Canadian Deuterium Uranium
ICE	Internal Combustion Engine
IEA	International Energy Agency
NO <sub>x</sub>	Nitrogen Oxide
NHI	National Hydrogen Initiative USA
NIST	National Institute of Standards and Technology USA
PEM	Proton Exchange Membrane
RKF	Runge-Kutta-Fehlberg
SCWR	Supercritical Water Reactor
XRD	X-ray Diffraction

## Chapter 1 – Introduction

---

This thesis provides new contributions to the state of the art of the thermochemical Cu-Cl cycle for hydrogen production. The experiments and theoretical models complement previous proof of concept experiments and add to the existing understanding of key aspects of the cycle. The results will help move forward the effort to implement a scale-up version of the Cu-Cl cycle for hydrogen production.

### 1.1 Background

The history of hydrogen analysis starts when it was first recognized as a distinct element in 1766 by the British scientist Henry Cavendish (as cited in Nyserda [1]) by reacting zinc metal with hydrogen chloride. Then in 1800, English scientist William Nicholson and Sir Antony Carlisle discovered that applying electric current to water produced hydrogen and oxygen gases through a process known as electrolysis. Opposite to the electrolytic cell, a galvanic cell, known today as the fuel cell, combines hydrogen and oxygen gases to produce water and electricity. The galvanic effect was first discovered in 1845 by Swiss chemist Christian Friedrich Schoenbein. This discovery inspired Jules Verne in 1874 who prophetically examined the potential use of hydrogen in his fiction book entitled “The Mysterious Island” and pronounced: *“I believe that water will one day be employed as fuel, that hydrogen and oxygen which constitute it, used singly or together, will furnish an inexhaustible source of heat and light, of an intensity of which coal is not capable”*.

These meaningful events occur parallel to the need of humanity for energy sources and carriers that contain less carbon at each stage of civilization. Wood, coal, oil, and natural gas have preceded the growing quest for energy from cleaner sources, where

hydrogen can have an important role of carrying it to where it is needed and from sustainable, clean sources. To be considered clean, hydrogen must be produced from non-carbon primary energy sources such as nuclear, hydro, wind, solar, geothermal, wave and tidal, and to some extent biomass. Thus, since hydrogen can be produced from clean sources, the role of hydrogen has been widely accepted as important for a sustainable energy future. Therefore, the strategies for implementation of a hydrogen based economy that competes with the established fossil-fuel economy are tightly connected to the development of renewable energy.

The role of renewable energy and its introduction into the fossil fuel based energy system has been actively researched and debated in the political, scientific and economic areas. Furthermore, there has been some action from governments to promote renewables in response to scientific concerns of global warming, commercial interest for new business opportunities justified by high prices of fossil fuels, and technological challenges associated to the development of renewable energies. A more pragmatic approach recognizes that the economic participation of clean energy technologies in the bulk of the economic activity that derives from the energy business is still incipient, that fossil fuels overwhelmingly dominate the market, and that this situation will prevail for the years to come. Analysis of historical data published by BP Statistical Review in June 2011 [2] and projections from BP Energy Outlook 2030 [3] and the International Energy Agency [4] on world energy consumption indicated that the participation of renewables in 2010 was 1.3 % with hydro at 6.5 %, and that by 2030 the participation will grow to 4.8 and 7.0% respectively.

Figure 1.1 indicates the participation of all forms of energy in the global spectrum of consumption to 2030. In the figure, the total energy consumption is normalized to the levels of 2030. Even though the growth of renewable energy has been almost exponential during the last 10 years, its participation in the global energy supply is still low, on the order of 1%. The relatively increasing numbers are stimulated by high prices and the implementation of efficiency measures that reduce the rate of consumption of fossil fuels and coal, thus making the proportion of renewables more significant.

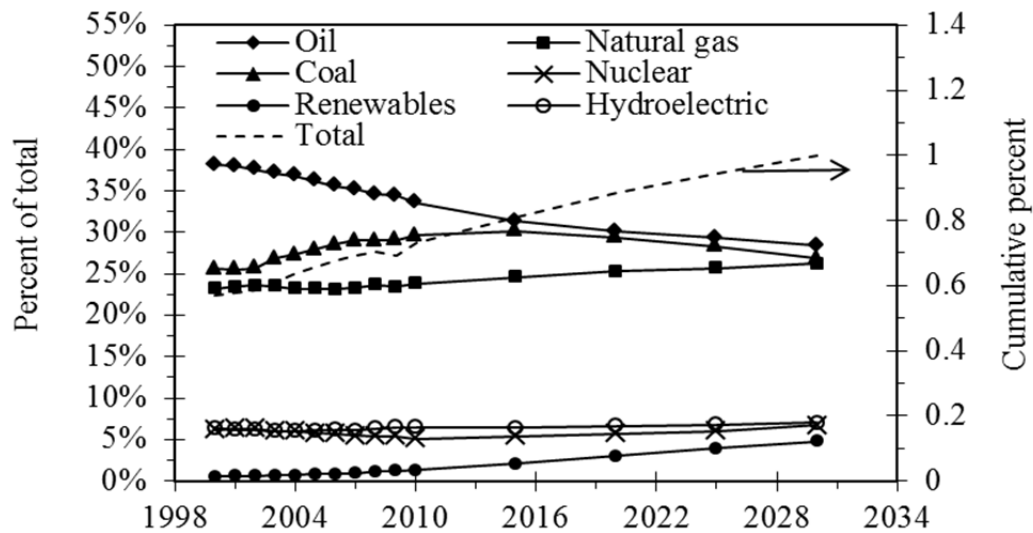


Fig. 1.1: World energy consumption projected to 2030 [3]

The growth in participation of renewable energy does not necessarily indicate that the hydrogen economy is moving ahead. Renewable sources are being used directly for the generation and utilization of electricity, or in the case of liquid fuels from renewable sources such as biomass or some biofuels, directly injected in burners for industrial application. This leads to an ease of transportation of energy. It is easier to transfer the energy from the source as electricity or as liquid than it is in any form of hydrogen.

Furthermore, the immediate utilization of the forms of renewable energy makes it unnecessary for the hydrogen transformation, a transition that contrasts with the versatility of fossil fuels that can be easily stored and transported. To compete with this unique characteristic, a replacement fuel must provide similar characteristics or be supported by the appropriate infrastructure.

Electricity is relatively easy to transport but hard to store, thus it must be used when it is produced. The ideal energy carrier is easy to transport and easy to store. Hydrogen has been recognized as an energy carrier for over a century now, however, its main utilization today is for the refinement and upgrading of fossil fuels as a fundamental component of the liquid fuels where natural gas has been the main feedstock for its production. More than 96% of the hydrogen produced in the world today results from transformation of natural gas and light hydrocarbons as indicated by Ball and Wietschel [5] and the Gas Encyclopaedia [6], a process that also produces significant amounts of greenhouse gas.

Hydrogen was used in the 1860s and mixed with carbon monoxide, methanol and other hydrocarbons to produce town-gas for street lighting as well as for cooking and heating. Hydrogen offers a number of advantages in synergy with the need for sustainable growth in balance with nature if it is produced from clean and renewable sources. The utilization of hydrogen is also an emission free process that results in the production of water at the point of use. Except for electricity, hydrogen is the only energy carrier that can be produced from any local primary energy source. Produced in parallel with the generation of electricity from renewable resources, hydrogen can be used to smooth out

the intermittent and unpredictable nature of those primary energy sources and store energy for use when it is most needed. Unlike other electric energy storage systems, stored hydrogen does not vanish and the storage systems do not lose retention capability with time and/or temperature. Thus, hydrogen is a secondary energy carrier in the sense that it needs to be produced from a primary energy source, like electricity. It offers the unique possibility of being produced and consumed without polluting the environment, but the challenges of producing, storing and transporting hydrogen are also unique due to its differentiating physical properties.

### **1.1.1 Hydrogen as an Energy Carrier**

Hydrogen is second only to uranium in gravimetric energy density and at least 2.5 times larger than gasoline and about three times larger than methanol. Table 1.1 details the physical characteristics of hydrogen and compares it with air and fuels of common use. In addition to being produced from clean renewable energy, hydrogen is attractive for its high energy content (Higher Heating Value).

Hydrogen contains the highest energy to weight ratio, thereby making it the preferable fuel for space exploration where weight has critical importance. Unfortunately, its volumetric energy density is the lowest at atmospheric conditions and must be liquefied, reaching up to  $8.5 \times 10^6$  kJ/L while consuming about 30% of the energy contained in the hydrogen. The low energy density of hydrogen at atmospheric conditions implies that additional energy must be used to compress or liquefy the gas to increase its volumetric energy density before it can be used in applications similar to those of conventional fuels.

Table 1.1: Physical properties of hydrogen, air and conventional fuels

Property	Units	Hydrogen	Propane	Methane	Gasoline *	Air	Uranium**
Molecular Weight	g/mol	2.016	44.096	16.043	100 - 105	28.95	238.03
Boiling Point	°C	-253	-42	-161.6		-194	4404
Melting point	°C	-259	-187.7	-182.5		-213	1132
Density (vapour)	kg/m <sup>3</sup>	0.08376	2.423	0.65	4.4	1.203	
Density (liquid)	kg/m <sup>3</sup>	70.8	582	422.8	700	875	18,950
Specific Volume (gas)	m <sup>3</sup> /kg	11.939	0.41	1.5385	0.2273	0.8313	
Specific Volume (liquid)	m <sup>3</sup> /kg	0.0141	0.0017	0.0024	0.0014		
Specific Gravity	-	0.0696	1.55	0.5403	3.6575	1.0	
Expansion Ratio liq/gas		1:848	1:240	1:650			
Latent Heat Vapourization	kJ/kg	454.3	425.31	510		198.7	
Latent Heat of Fusion	kJ/kg	58.158	94.98	58.68			
Heat Capacity (Cp)	kJ/mol.K	0.029	0.075	0.035		0.029	
Heat Capacity (Cv)	kJ/mol.K	0.021	0.066	0.027		0.02	
Viscosity	Poise	8.65E-05		0.0001027		0.00017	
Thermal Conductivity	mW/m.K	168.35	15.198	32.81		23.94	2.75E+04
Compressibility factor (z)		1.001	0.9821	0.998		0.9992	
Critical Temperature	°C	-240	96.6	-82.7		-140.5	
Critical Pressure	bar	12.98	42.5	45.96		37.71	
Auto-ignition Temperature	°C	585	490	540	230 -480		
Energy Content	kJ/kg (H)	141.86	50.35	55.53	47.3		7.95E+07
	kJ/kg (L)	119.93	46.35	50.02	44.4		
Energy Density	kJ/m <sup>3</sup> (L)	10,050	86,670	32,560	3.12E+07		1.53E+09
	kJ/m <sup>3+</sup>	1.83E+06		6.86E+06			
	kJ/m <sup>3++</sup>	5.60E+06					
	kJ/m <sup>3+++</sup>	8.49E+06	2.35E+07	2.09E+07			
All values at 25 °C and 1 Atm. unless specified otherwise							
* C4 to C12; ** Averages; +200 bar; ++700 bar; +++Liquid; (H) = Higher heating value; (L) = Lower heating value							

Figure 1.2 indicates the normalized weight and energy contents of fuels relative to hydrogen. The weight of gasoline is 9.9 times that of hydrogen, while the energy content is only 3.3 times the energy content of hydrogen. Thus, for each kilogram, hydrogen can release up to 2.5 times the energy released by other conventional fuels. An important consequence of the high energy content implies that the energy released during a catastrophic event is about 2.5 times larger when the fuel is hydrogen. However, the duration tends to be inversely proportional to the energy in the combustible fuel so that hydrogen fires extinguish faster than hydrocarbon fires, as indicated in Hydrogen Properties [7].

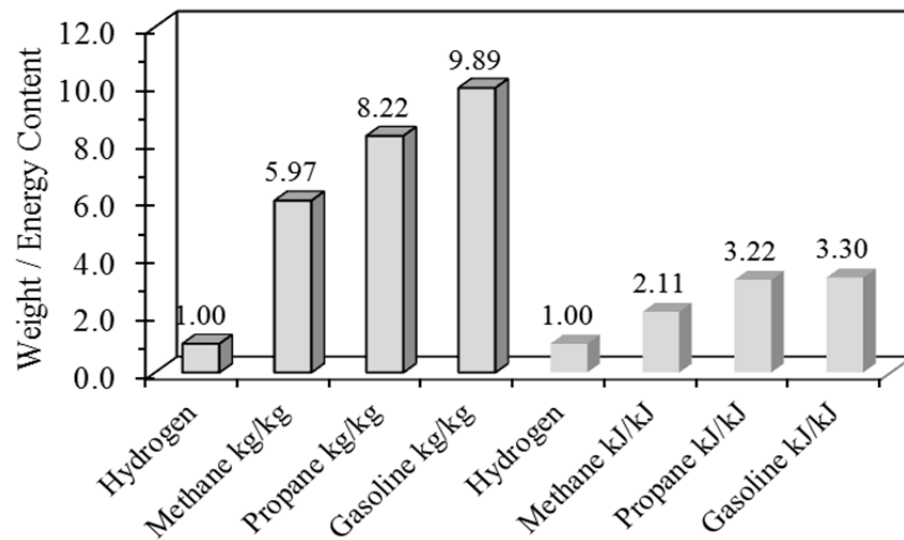


Fig. 1.2: Weight and energy content of liquid fuels relative to liquid hydrogen

Hydrogen has been pointed as the reason of accidents where the presence of the gas made it the potential cause despite a lack of understanding of its properties. Pure

hydrogen is odourless, colorless and tasteless making it almost undetectable from leaks in daylight. Like any other gas, hydrogen may produce asphyxiation by displacing oxygen to concentration levels that possess risk for human breathing. Levels of oxygen below 19.5% result in asphyxiation, and concentrations below 12% produce unconsciousness without prior warning symptoms. However, hydrogen is approximately 14 times lighter than atmospheric air, such that when leaks occur, hydrogen rises rapidly and it moves away from the leaking zone.

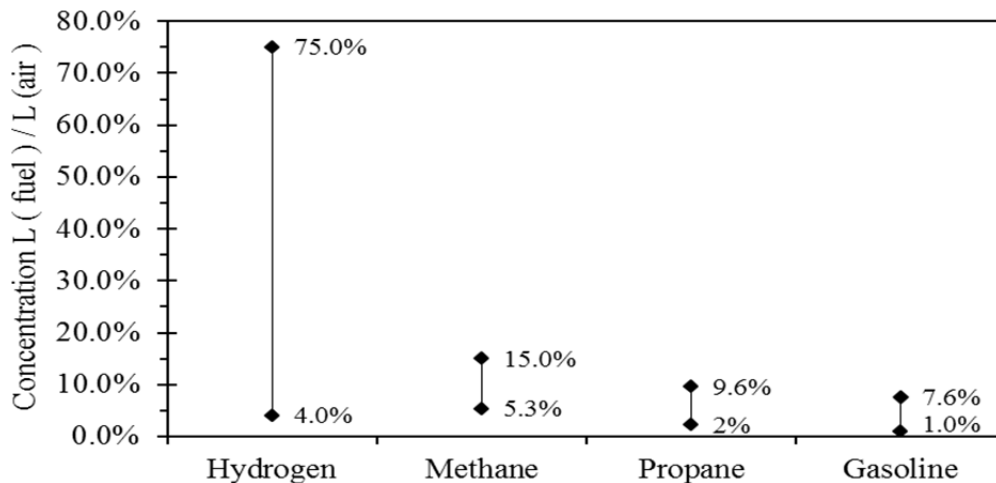


Fig. 1.3: Concentration range of flammability of hydrogen and conventional fuels in standard air at 25 °C and 1Atm.

Methane is approximately 2 times lighter than air, thus it does not move away as fast, and gasoline and propane are several times heavier than air and will follow the shape of the terrain and form pools upon leaking. Hydrogen remains flammable in air at concentrations between the limits of 4% and 75%, and it is explosive in the range of 15 to 59%. Methane is flammable in the range of 5.3 to 15% and gasoline in the range of 1.0 to 7.6%. The relative ranges of flammability are indicated in Fig. 1.3. However, in the

absence of sparks or sources of ignition, hydrogen in the range of flammability concentrations does not initiate self-sustained combustion before reaching a temperature of 585 °C, while methane will self-ignite at 540 and gasoline at 240 °C when in the flammability concentrations. Although hydrogen has a higher auto-ignition temperature, it requires very low ignition energy of 0.02 mJ, about one order of magnitude lower than methane or gasoline.

Because of the high energy content, hydrogen is very attractive to the transportation industry especially with fuel cells. Fuel cells, namely the Proton Exchange Membrane (PEM) fuel cell operate at efficiencies as high as 60% as indicated by Mert et al. [8]. They have been proposed as a substitute for the internal combustion engine (ICE) in automobiles. On the other hand, the automotive industry has been developing the ICE for the last 100 years. The ICE operates on the principle of the Otto cycle, which engineers have endeavoured to improve by challenging the thermodynamic limits. High temperature limits of materials, concerns about formation and emission of nitrogen oxides (NO<sub>x</sub>) and auto-ignition issues impose additional limits.

The overall efficiency of the Otto cycle is in the range of 25% to a maximum of 32% when using anhydrous alcohol fuels as indicated in Economy and Energy [9]. Thus it indicates that a vehicle using a PEM fuel cell requires approximately half the weight of fuel to perform the same amount of work when using hydrogen. However, the volume of this mass of hydrogen is substantially larger than gasoline. The automotive fuel cells have progressed significantly in recent years, but technical developments are still necessary to achieve the performance and cost goals necessary to compete with the ICE. A study by

Hooks and Jackson [10] on analysis of the challenges for implementation of fuel cell vehicles and fuelling stations in California indicated that the primary improvements include simultaneously increasing the power density of the membrane-electrode assemblies (MEAs) to reduce the overall size of the fuel cell stack, reducing the catalyst loading and associated cost, increasing the operating life, and expanding the operational temperature range of the cell.

Frenette and Forthoffer [11] reported the result of experiences with a fleet of fuel cell vehicles by Ford Company over more than one million miles or 30,000 hours in different environments. Several aspects of the experience and technology issues were discussed. Among them, storage of hydrogen on-board remains an issue. The study concluded that major technological improvements are needed for on-board hydrogen storage to enable a travel range equivalent to conventional combustion engines.

With today's state of the art technology, the required volume of a gaseous hydrogen tank to contain the equivalent energy of a conventional gasoline tank varies depending on storage pressure. For the same vehicle range, the volume of a hydrogen tank at 10,000 psi (700 bar) would be nearly 5 times larger than a conventional gasoline tank; while at 5,000 psi (350 bar) the volume would be approximately 7.5 times larger than a conventional tank. No near-term solution for improved storage has been identified to provide a competitive operating range without compromising existing vehicle platforms. Thus, significant technology challenges exist for the deployment of fuel cell vehicles from the perspective of the vehicle platform itself. Additional challenges exist for the development of the appropriate infrastructure to support hydrogen fuelling of vehicles. In

general, a hydrogen infrastructure will arise naturally as long as the cost of hydrogen is competitive in the fuels market.

A different scenario for the deployment of hydrogen is present when stationary applications are considered. Hydrogen produced from renewable resources can be utilized directly in many stationary applications where weight and space are not a significant constraint. Hydrogen generation plants working in tandem with nuclear plants, solar plants, geothermal or wind can be used to produce clean hydrogen and smooth the peaks and valleys of power generation by storing energy in the form of hydrogen and generating power when it is needed and price competitive. Several methods of clean hydrogen production exist today, differentiated by the source of primary energy, level of maturity of the technology, and overall efficiency.

About 96% of today's hydrogen is produced from fossil fuels and the remaining portion is produced via electrolysis or a sub-product of chloralkaly plants. Technologies using fossil fuels have been proposed as a means of producing clean hydrogen based on the assumption of integrated Carbon Capture and Storage (CCS), such that power plants operate on hydrogen rich fuels following a CO<sub>2</sub> separation process, as indicated in the International Energy Agency Task 16 [12]. Thus, the concept of clean hydrogen is subject to the premise of capturing and storing CO<sub>2</sub>, a concept frequently questioned because of the probability of stored CO<sub>2</sub> leaking back to the atmosphere.

### **1.1.2 Hydrogen from Thermochemical Cycles**

Thermochemical cycles have been identified as a potential technology to compete with the traditional and mature electrolysis technology for hydrogen generation.

Table 1.2: Traditional and novel methods for hydrogen production

Method	Ref.	Constraints	State	T (°C)	Description
Steam Methane Reforming	15	CCS	Mature	700 - 1100	Reaction of steam at high temperature with natural gas.
Photo-biological	16	Low Efficiency	Early R & D	Ambient	Photo-biological water splitting based on cyanobacteria and green algae deprived of sulphur.
Pyrolysis of Biomass	17	CCS	Mature	200-300	Thermal decomposition of organic matter in the absence of oxygen.
Electrolysis of Water	18	Capital Intensive	Mature	60 - 85	Electrochemical decomposition by electrical current circulating through an electrolytic solution.
Ethanol Reforming	19	Biomass sources	Mature	300 - 600	Steam reforming of bio-fuel that relies on a closed carbon cycle.
Methanol Reforming	20	Toxicity	Mature	250 - 350	A mixture of methanol and water in molar concentrations of 1:1.5 is vaporized and separated in the presence of a catalyst.
Coal Gasification	21	CCS	Mature	700 - 900	Coal, oxygen and water molecules oxidize to produce a mix of CO <sub>2</sub> , CO and H <sub>2</sub> gases.
Thermochemical S-I cycle	22	Materials	Pilot Plant	850 - 1000	Three reactions in a sulphur and iodine closed cycle.
Thermochemical Cu-Cl cycle	23, 24	Solids handling	R & D	500 -700	Three reactions in a copper and chlorine closed cycle.
Steam Electrolysis	25	Materials	Mature	100 - 850	High temperature electrolysis.
Solid Oxide Water Electrolysis	26	Materials	Mature	500 - 800	High temperature electrolysis using solid oxide or ceramic electrolyte.
Photolysis of Water	27	Materials	Early R & D	Ambient	Photo-electrochemical cells immersed in aqueous electrolyte use solar light to split water.
CCS = carbon capture and storage					

Several technologies for the generation of clean hydrogen have been proposed and presented and are found at different stages of development as indicated in Table 1.2. The Thermochemical Cu-Cl cycles have been proposed for integration with any of the Generation IV nuclear reactors currently under consideration as discussed by M.A. Rosen [13] and Elder and Allen [14].

The cycles are based on chemical reactions using familiar concepts of chemistry and chemical engineering and supported, in most cases, by technologically mature physical processes. Proof of concept experimental work and analysis has been implemented in several cycles as indicated in Table 1.2 [15 – 27], from which the Sulfur-Iodine (S-I) and Copper-Chlorine (Cu-Cl) cycles are at the most advanced phase of development.

The possibility of integrating hydrogen production with nuclear power generation has been discussed for a long time and thermochemical cycles are an attractive option because of high thermodynamic efficiency, as discussed by Naterer et al. [23]. The Cu-Cl cycle operates at a maximum temperature of 550 °C and separates water through three reactions complemented by several physical steps that use mature, commercial technology as discussed by Wang et al. [24].

The lower temperature and less corrosive species in the Cu-Cl cycle, when compared to the Sulphur-Iodine cycle at 850 °C, facilitate the design of heat exchangers and reactors with potentially fewer material corrosion challenges.

The Cu-Cl cycle is the subject of this thesis specifically with detailed experimental work on the chemical decomposition reaction. This thesis provides new understanding

that allows the safe design of a reactor for integration with the hydrolysis and electrolysis reactions in the Cu-Cl cycle.

## **1.2 Motivation and Objectives of Thesis**

This thesis focuses on selected key questions that must be answered for the effective design of a reactor used in the decomposition of  $\text{CuO} \cdot \text{CuCl}_2$ . In particular, the main hypothesis to be tested is that the yield from samples of  $\text{CuO} \cdot \text{CuCl}_2$  undergoing thermal decomposition is impacted by the concentration of solids in the molten  $\text{CuCl}$  and the difference of temperatures between the solid and the molten bath. For a given temperature, the rate of solids fed to the reactor must be maintained below a critical concentration. This hypothesis will be examined in detail in this thesis.

The main objective of this research is to develop and validate new predictive models and experimental methods of transport phenomena of the physical processes of decomposition in the copper oxychloride reactor, as follows.

1. Assemble relevant mass, momentum and energy equations and develop mathematical models for the analysis of the convection and diffusion phenomena for a solid particle submerged in molten salt, and with chemical decomposition occurring in a transition layer at the particle surface.
2. Develop new semi-analytical solutions to the mathematical models and implement numerical solutions via a computer simulation method for design purposes.
3. Analyze and validate the predictions of theoretical models using experimental results of the chemical decomposition.

4. Determine concentration vs. time correlations and develop a reaction rate equation. Recommend implications on the scale-up of the thermochemical Cu-Cl cycle.

## Chapter 2 - Literature Review

---

### 2.1 Thermochemical Cycles

Thermochemical cycles have been proposed as an alternative and potentially more efficient method to produce hydrogen from water. The International Round Table on Direct Production of Hydrogen with Nuclear Heat held in Ispra, Italy in 1969 set the criteria for evaluation of thermochemical cycles as discussed by Beghi [28].

Table 2.1: Summary of Ispra recommended thermochemical cycles

Mark	Chemicals	Temperature (°C)	No. of reactions
Mark 1	Hg, Ca, Br	780	4
Mark 1B	Hg, Ca, Br	780	5
Mark 1C	Cu, Ca, Br	770	4
Mark 1S	Hg, Sr, Br	770	3
Mark 2	Mn, Na, (K)	770	3
Mark 2C	Mn, Na, (K), C	750	4
Mark 3	V, Cl, O	800	4
Mark 4	Fe, Cl, S	800	4
Mark 5	Hg, Ca, Br, C	850	5
Mark 6	Cr, Cl, Fe, (V)	800	4
Mark 6C	Cr, Cl, Fe, (V) Cu	800	5
Mark 7	Fe, Cl	800	5
Mark 7A	Fe, Cl	800	5
Mark 7B	Fe, Cl	850	5
Mark 8	Mn, Cl	850	3
Mark 9	Fe, Cl	650	3
Mark 10	I, S, N	850	6
Mark 11	S (hybrid)	850	2
Mark 12	I, S, N, Zn	850	4
Mark 13	Br, S (hybrid)	850	3
Mark 14	Fe, Cl	650	5
Mark 15	Fe, Cl	730	4
Mark 16	S, I	850	3
Mark 17	Sulfur-Iodine	850	3

A list of proposed cycles then emerged as indicated in Table 2.1 (Mark 1 to 17) and a three stages process of evaluation was initiated. Thermochemical decomposition of water for hydrogen production was transformed from theoretical concept to a promising reality. Since then, over 350 potential cycles have been identified. At the end of the 1990s, Brown et al. [29], a group of researchers working under the Nuclear Energy Research Initiative (NERI) Program of the U.S. Department of Energy, applied screening criteria to over 115 cycles. They scored the cycles based on the number of chemical reactions, number of separation steps, maximum temperature and number of published references, among others, to arrive at 40 cycles.

A second screening with consideration for environmental, safety and health aspects reduced the number to 25 cycles. More recently the Nuclear Hydrogen Initiative (NHI) of the U.S. Department of Energy, Office of Nuclear Energy Science and Technology supported the re-evaluation of thermochemical cycles in the literature having both promising efficiencies and proof-of-concept. The NHI program is connected to the Next Generation Nuclear Plant (Gen IV) program to develop a reactor capable of providing high-temperature process heat. Because high-temperature processes that use high temperature heat achieve higher efficiency, R&D has been focused on thermochemical cycles, hybrid thermochemical cycles, and high-temperature electrolysis.

The focus of the NHI initiative was to identify and develop nuclear technologies that produce hydrogen from water feedstock at prices that are competitive with other fuels and using domestic process materials by 2019. Lewis et al. [30-32], working under the NHI program, and with focus on the first two categories of high-temperature processes,

applied new screening criteria to recently published literature on thermochemical cycles in Table 2.2. The program had an objective to determine cycles that justify additional research and complement the NHI portfolio of hydrogen technologies that can operate with nuclear reactors. The maximum temperature of the cycle determines the type of heat source required. This parameter was used as part of the criteria for selection, with the baseline Sulfur-Iodine cycles setting the limit at 825-850 °C.

The Sulfur-Iodine cycle consists of three reactions. It has been developed extensively with the design and construction of a lab scale cycle to investigate the potential of using nuclear energy. Analysis and experiments performed at the Sandia National Lab with participation of General Atomics between 2002 and 2008 and discussed by Russ and Pickard [33] found many challenges associated with complex multiphase reaction equilibrium, high temperatures, strong acids and materials requirements. The experimental work has not yet conclusively answered questions on preferable technologies, sources of energy and disposal of products of side reactions as reported by Russ and Pickard [33].

The study by Lewis et al. [30-32] recommended the Cu-Cl cycle for additional research and discarded the others based on criteria of low yield equilibrium due to competing product formation, requirements to develop new technologies to improve yields in reverse reactions, high maximum temperatures, difficult separation of gas, solid or liquid phases, slow kinetics, proof of concept experimental work, and missing data, among others.

Table 2.2: Thermochemical cycles proposed for integration with nuclear reactors. Lewis et al. [30-32]

Cycle	#	Reactions	T (°C)
Hybrid Chlorine	1	$\text{Cl}_{2(\text{g})} + \text{H}_2\text{O}_{(\text{g})} \rightarrow 2\text{HCl}_{(\text{g})} + 0.5\text{O}_{2(\text{g})}$	850
		$2\text{HCl}_{(\text{g})} \rightarrow \text{H}_{2(\text{g})} + \text{Cl}_{2(\text{g})}$ (electrolytic)	75
Magnesium-Iodine	2	$6/5\text{MgO}_{(\text{s})} + 6/5\text{I}_{2(\text{l})} \rightarrow 1/5\text{Mg}(\text{IO}_3)_2_{(\text{s})} + \text{MgI}_{2(\text{a})}$	120
		$1/5\text{Mg}(\text{IO}_3)_2_{(\text{s})} \rightarrow 1/5\text{MgO}_{(\text{s})} + 1/5\text{I}_{2(\text{g})} + 1/2\text{O}_{2(\text{g})}$	600
		$\text{MgI}_2 \cdot 6\text{H}_2\text{O}_{(\text{s})} \rightarrow 5\text{MgO}_{(\text{s})} + 5\text{H}_2\text{O}_{(\text{g})} + 2\text{HI}_{(\text{g})}$	450
		$2\text{HI}_{(\text{g})} \rightarrow \text{I}_{2(\text{g})} + \text{H}_{2(\text{g})}$	500
Copper-Sulphate	3	$2\text{H}_2\text{O}_{(\text{l})} + \text{SO}_{2(\text{g})} \rightarrow \text{H}_2\text{SO}_{4(\text{a})} + \text{H}_{2(\text{g})}$ (electrolytic)	25
		$\text{CuO}_{(\text{s})} + \text{H}_2\text{SO}_{4(\text{a})} + x\text{H}_2\text{O} \rightarrow \text{CuSO}_4 \cdot (x-1)\text{H}_2\text{O}_{(\text{s,a})}$	25
		$\text{CuSO}_4 \cdot (x-1)\text{H}_2\text{O} \rightarrow \text{CuSO}_4 + 4\text{H}_2\text{O}$	525
		$\text{CuSO}_{4(\text{s})} \rightarrow \text{CuO}_{(\text{s})} + \text{SO}_{2(\text{g})} + 0.5\text{O}_{2(\text{g})}$	825
Iron-Chlorine	4	$3\text{FeCl}_{2(\text{s})} + 4\text{H}_2\text{O}_{(\text{g})} \rightarrow \text{Fe}_3\text{O}_{4(\text{s})} + 6\text{HCl}_{(\text{g})} + \text{H}_{2(\text{g})}$	925
		$\text{Fe}_3\text{O}_{4(\text{s})} + 8\text{HCl}_{(\text{g})} \rightarrow \text{FeCl}_2 + 2\text{FeCl}_3 + 4\text{H}_2\text{O}_{(\text{g})}$	125
		$2\text{FeCl}_{3(\text{s})} \rightarrow 2\text{FeCl}_{2(\text{s})} + \text{Cl}_{2(\text{g})}$	425
		$\text{Cl}_2 + \text{H}_2\text{O}_{(\text{g})} \rightarrow 2\text{HCl}_{(\text{g})} + 0.5\text{O}_{2(\text{g})}$	925
Vanadium-Chloride	5	$2\text{VCl}_{2(\text{s})} + 2\text{HCl}_{(\text{a})} \rightarrow \text{VCl}_{3(\text{s})} + \text{H}_{2(\text{g})}$	120
		$4\text{VCl}_{3(\text{s})} \rightarrow 2\text{VCl}_{4(\text{g})} + 2\text{VCl}_{2(\text{s})}$	766
		$2\text{VCl}_{4(\text{l})} \rightarrow 2\text{VCl}_3 + \text{Cl}_2_{(\text{g})}$	200
		$\text{Cl}_{2(\text{g})} + \text{H}_2\text{O}_{(\text{g})} \rightarrow 2\text{HCl}_{(\text{g})} + 0.5\text{O}_{2(\text{g})}$	875
Cerium-Chlorine	6	$2\text{CeO}_{2(\text{s})} + 8\text{HCl}_{(\text{g})} \rightarrow 2\text{CeCl}_{3(\text{s})} + \text{Cl}_{2(\text{g})}$	110
		$2\text{CeCl}_{3(\text{s})} + 4\text{H}_2\text{O}_{(\text{g})} \rightarrow 2\text{CeO}_{2(\text{s})} + 6\text{HCl}_{(\text{g})}$	925
		$\text{Cl}_{2(\text{g})} + \text{H}_2\text{O}_{(\text{g})} \rightarrow 2\text{HCl}_{(\text{g})} + 0.5\text{O}_{2(\text{g})}$	850
Copper - Chlorine (Dokiya and Kotera)	7a	$2\text{CuCl}_2 + \text{H}_2\text{O}_{(\text{g})} \rightarrow 2\text{CuCl}_{(\text{l})} + 0.5\text{O}_{2(\text{g})} + 2\text{HCl}_{(\text{g})}$	700
		$2\text{CuCl}_{(\text{a})} + 2\text{HCl}_{(\text{g})} \rightarrow \text{H}_{2(\text{g})} + 2\text{CuCl}_{2(\text{s})}$ (electrolytic)	25
Copper - Chlorine (University of Illinois, Argon National Labs)	7b	$4\text{CuCl}_{(\text{a})} \rightarrow 2\text{CuCl}_{2(\text{a})} + 2\text{Cu}_{(\text{s})}$ (electrolytic)	25
		$2\text{Cu}_{(\text{s})} + 2\text{HCl}_{(\text{g})} \rightarrow 2\text{CuCl}_{(\text{l})} + \text{H}_{2(\text{g})}$	425
		$2\text{CuCl}_{2(\text{s})} + \text{H}_2\text{O}_{(\text{g})} \rightarrow \text{Cu}_2\text{OCl}_{2(\text{s})} + 2\text{HCl}_{(\text{g})}$	425
		$\text{Cu}_2\text{OCl}_2 \rightarrow 2\text{CuCl}_{(\text{l})} + 0.5\text{O}_{2(\text{g})}$	535
Copper – Chlorine (Argonne National Lab)	7c	$2\text{CuCl} + 2\text{HCl}_{(\text{a})} \rightarrow 2\text{CuCl}_2 + \text{H}_{2(\text{g})}$ (electrolytic)	80
		$2\text{CuCl}_{2(\text{s})} + \text{H}_2\text{O}_{(\text{g})} \rightarrow \text{Cu}_2\text{OCl}_{2(\text{s})} + 2\text{HCl}_{(\text{g})}$	425
		$\text{Cu}_2\text{OCl}_2 \rightarrow 2\text{CuCl}_{(\text{l})} + 0.5\text{O}_{2(\text{g})}$	535
Hybrid Calcium-Bromide	8	$\text{CaBr}_2 + \text{H}_2\text{O}_{(\text{g})} \rightarrow \text{CaO} + 2\text{HBr}_{(\text{g})}$	770
		$2\text{HBr}_{(\text{g})} \rightarrow \text{H}_{2(\text{g})} + \text{Br}_{2(\text{g})}$ (Plasma)	50
		$\text{CaO} + \text{Br}_{2(\text{g})} \rightarrow \text{CaBr}_2 + 0.5\text{O}_{2(\text{g})}$	550

## 2.2 Thermochemical Cu-Cl Cycle

The Cu-Cl cycle is characterized by a lower maximum temperature, no catalyst required for thermal reactions (e.g. low energy of reaction), all reactions already demonstrated at a laboratory scale, and efficiency and hydrogen costs within DOE's targets. Naterer et al. [34] provided a cost comparison for hydrogen produced through electrolysis and the thermochemical Cu-Cl cycle. The study assumed similar conditions for hydrogen transportation and electrolysis operation outside peak hours. At 10 tons/day, electrolysis yields a total hydrogen cost of 2.69 \$/kg, while hydrogen produced through a thermochemical Cu-Cl cycle results in a total cost of 2.71 \$/kg. At a larger capacity of 200 ton/day, the thermochemical cycle results in a hydrogen cost of 2.00 \$/kg. The advantage occurs from the intensive capital requirement for electrolysis at higher capacities. The cost of hydrogen from the thermochemical cycle is consistent with the goals set by DOE at US 3.80 \$/kg (delivered, untaxed) in its Hydrogen Posture Plan [35].

Lower temperatures and mildly aggressive chemicals result in lower technological and economic challenges. The Cu-Cl cycle, with a thermodynamic limit at 530 °C, has been proposed as a candidate for integration with a Supercritical Water Reactor (SCWR), Canada's generation IV nuclear reactor as discussed by Wang et al. [36].

Further integration with nuclear reactors including traditional water electrolysis that uses off-peak electricity was discussed by Naterer et al. [37]. Hydrogen can provide both benefits of carrying and storing energy. It was proposed that the base load of the reactor can be used in the thermochemical Cu-Cl cycle and that remaining energy is used to produce electricity for regular consumption. Thus, peaks and valleys of electric power

consumption can be smoothed out through the generation of electrolytic hydrogen. This concept takes advantage of the fast response capability of electrolytic hydrogen plants. Furthermore, the relatively low temperatures of operation of the Cu-Cl cycle open the possibility to obtain heat from other sources such as surplus heat from industrial processes, solar energy, geothermal or upgraded heat from other clean thermal sources.

Table 2.3: Proposed variations of the Cu-Cl cycle

No.	Ref.	Type	T °C	Reactants				Products						ΔH (kJ/mol)						
1	Wang et al.	C, x	450	2Cu	(s)	+	2HCl	(g)	→	2CuCl	(m)	+	H <sub>2</sub>	(g)					N/A	
	[36]	E	80	4CuCl	(aq)	+	2Cu	(s)	→	2CuCl <sub>2</sub>	(aq)								N/A	
		Dr, e	150	CuCl <sub>2</sub>	(aq)	+	2H <sub>2</sub> O	(l)	→	CuCl <sub>2</sub> *H <sub>2</sub>	(s)	+	H <sub>2</sub> O	(g)					165.2*	
		H, e	375	2CuCl <sub>2</sub> *H <sub>2</sub> O	(s)	+	H <sub>2</sub> O	(g)	→	CuO*Cu	(s)	+	2H <sub>2</sub> O	(g)	+	2HCl	(g)			N/A
		D, e	530	CuO*CuCl <sub>2</sub>	(s)				→	2CuCl	(m)	+	0.5O <sub>2</sub>	(g)					129.3*	
2	Wang et al.	C, x	450	2Cu	(s)	+	2HCl	(g)	→	2CuCl	(m)	+	H <sub>2</sub>	(g)					-1.7*	
	[36]	E	80	4 CuCl	(aq)				→	2Cu	(s)	+	2CuCl <sub>2</sub>	(aq)					96.2*	
		H, e	375	2CuCl <sub>2</sub>	(aq)	+	H <sub>2</sub> O	(g)	→	CuO*Cu	(s)	+	H <sub>2</sub> O	(g)	+	2HCl	(g)			N/A
		D, e	530	CuO*CuCl <sub>2</sub>	(s)					2CuCl	(m)	+	0.5O <sub>2</sub>	(g)					129.3*	
3	Wang et al.	C, x	450	2Cu	(s)	+	2HCl	(g)	→	2CuCl	(aq)	+	H <sub>2</sub>	(g)					-1.7*	
	[36]	E	80	4CuCl	(aq)				→	2Cu	(s)	+	2CuCl <sub>2</sub>	(aq)					96.2*	
		D, e	600	CuCl <sub>2</sub>	(aq)	+	H <sub>2</sub> O	(g)	→	2CuCl	(m)	+	H <sub>2</sub> O	(g)	+	2HCl	(g)	+	0.5O <sub>2</sub> (g)	N/A
4	Dokiya	H, e	700	2CuCl <sub>2</sub>	(s)	+	H <sub>2</sub> O	(g)	→	2CuCl	(m)	+	2HCl	(g)	+	0.5O <sub>2</sub> (g)			148**	
	[38]	E	25	2CuCL	(aq)				→	2CuCl <sub>2</sub>	(s)	+	2HCl	(g)	+	H <sub>2</sub>	(g)		75**	
5	Carty et al.	E	80	4CuCl	(aq)				→	2Cu	(s)	+	2CuCl <sub>2</sub>	(aq)	+	2HCl	(g)		96.2*	
	[40]	C, x	425	2Cu	(s)	+	2CuCl	(m)	→	H <sub>2</sub>	(g)								-1.7*	
	UI/ANL	H, e	425	2CuCl <sub>2</sub>	(s)	+	H <sub>2</sub> O	(g)	→	Cu <sub>2</sub> OCl <sub>2</sub>	(s)	+	2HCl	(g)					N/A	
		D, e	535	Cu <sub>2</sub> OCl <sub>2</sub>	(s)	+			→	2CuCl	(m)	+	0.5O <sub>2</sub>	(g)					129.3*	
6	Lewis et al.	E	80	2CuCl	(aq)	+	2HCL	(aq)	→	2CuCl <sub>2</sub>	(aq)	+	H <sub>2</sub>	(g)					93.7*	
	[32]	H, e	425	2CuCL <sub>2</sub>	(s)	+	H <sub>2</sub> O	(g)	→	Cu <sub>2</sub> OCl <sub>2</sub>	(s)	+	2HCL	(g)					116.7*	
	ANL/UOIT	D,e	535	Cu <sub>2</sub> OCl <sub>2</sub>	(s)				→	2CuCl	(m)	+	0.5O <sub>2</sub>	(g)					129.3*	
R = Reagent; P = Product; m = molten; aq = aqueous; l = liquid; s = solid; g = gas																				
E = Electrolysis; H = Hydrolysis; C = Chlorination; D = Decomposition; Dr = Drying; e = endothermic; x = exothermic																				
* Lewis et al. [32]																				

Variations of the thermochemical Cu-Cl cycle as indicated in Table 2.3 have been proposed and discussed in the literature. It is important to clarify that the past literature

refers to steps and reactions in a mixed manner that does not differentiate physical from chemical process.

The analysis presented here differentiates the physical (step) that affects the form but not the chemical composition from the chemical (reaction) where the transformation of species occurs. Table 2.3 presents a summary of six versions of the Cu-Cl cycle that include cycles of five, four, three and two cyclic reactions and steps as presented by Wang et al. [38]; Naterer et al. [39]; Dokiya and Kotera [40] and Lewis et al. [31].

The four reactions cycle, No. 1, discussed by Wang et al. [38] and Naterer et al. [39] starts with solid copper reacted exothermically in a chlorination reaction with hydrogen chloride at 450 °C to produce hydrogen gas and molten CuCl. The temperature differential with the subsequent electrolysis reaction opens the possibility for significant heat recovery within the cycle. Experimental work to recover heat from molten CuCl is currently under investigation at UOIT. The second reaction of this proposed cycle uses the electrolytic oxy-reduction (also known as dismutation) of CuCl that results in solid copper and aqueous copper (II) chloride as products. Handling of the mixture of solids and aqueous products from electrolysis is a major technological challenge. A third step uses a drying process to produce partially hydrated copper (II) chloride particles and evaporated water.

Preliminary experimental work reported by Naterer et al. [41] indicated that drying of CuCl<sub>2</sub> is an energy intensive process that impacts the efficiency and cost of the cycle. The experimental work used a spray dryer to process CuCl<sub>2</sub> with a water content of 8.2 and 2.0 mol-water/mol-CuCl<sub>2</sub> and obtained particles in the range of 100 to 200 microns.

The drying process is challenging because of the large volume of atmospheric air and energy required. The water splitting reaction occurs in a fluidized bed reactor at 375 °C where the solid particles in contact with superheated steam produce a solid mixture of CuO and CuCl<sub>2</sub> and a gaseous stream of vapor and hydrogen chloride. Further separation of the gas streams is required. The last reaction in the cycle results from the decomposition of CuO·CuCl<sub>2</sub> and results in molten CuCl and oxygen gas.

The four-one cycle (No. 2) was replaced with a four-step cycle that combines step 3 and reaction 4. Since reaction four implies hydrolysis of CuCl<sub>2</sub>, there is no need to completely dry the products in step 3. Preliminary research and thermodynamic analysis indicated that hydrolysis requires water in excess of the stoichiometric quantity. However, this change results in a requirement of a larger quantity of high quality heat for the combined process. The analysis reported by Wang et al. [38] indicated that the reactor for the combined chemical reaction must process five times more heat than the reactor for the chemical reaction of step 4 in the four-one cycle. Combination of step 3 into the chemical reaction results in more heat requirements. The increased heat load leads to larger engineering challenges for the reactor design and lower overall efficiency of the Cu–Cl cycle. This option has not been pursued further beyond this publication.

A three-reaction cycle (No. 3) was also discussed by Wang et al [38]. Starting with the chlorination of copper and following with the oxy-reduction of CuCl, the cycle closes with the direct decomposition of CuCl<sub>2</sub> at 600 °C. The decomposition reaction results in the production of vapor, hydrogen chloride and oxygen. The three gases must follow a separation process, which is energy intensive and results in further challenges and lower

overall efficiency of the cycle. The higher temperature requirement separated this option from possible integration with Canada's Gen IV Supercritical Water Reactor and hence it has been set aside.

Dokiya and Kotera [40] proposed a two reaction cycle (No. 4). The first reaction is the hydrolysis of  $\text{CuCl}_2$  at  $700\text{ }^\circ\text{C}$ . They performed proof of concept experiments, and further development resulted in a division of the hydrolysis reaction into two separate reactions to facilitate the separation of gases. The challenges of gas separation, reversible reactions and higher temperature requirements resulted in no further research. The elevated temperature results in the production of molten  $\text{CuCl}$  and a mixture of hydrogen chloride and oxygen gases. The requirement for separation of gases at higher temperatures resulted in additional engineering challenges and neglected the possibility of integration with the SCWR as discussed before. Although it is attractive because of its simplicity, this possibility has not been further investigated.

The University of Illinois at Chicago (UIC) and the Argonne National Lab (ANL) performed studies intended to demonstrate the feasibility of a four reaction hybrid Cu-Cl cycle (No. 5). Carty et al. [42] recommended this cycle as one of the most promising cycles after analyzing thermochemical cycles for hydrogen production based on the criteria of reactions whose free energy change lies within 10 kcal for a given temperature.

Following the proof of concept experiments and analysis from UIC and ANL, the cycle was recommended for further R&D, while major challenges were identified for the development of the copper electrolyzer. In the electrolysis reaction, an aqueous solution of 10 to 11 mol/L of  $\text{CuCl}$  and water results in the formation of solid copper and  $\text{CuCl}_2$  in

aqueous form. The chlorination of solid copper in contact with hydrogen chloride results in the release of gaseous hydrogen and molten  $\text{CuCl}$ .  $\text{HCl}$  and copper oxychloride are produced as a result of chemical hydrolysis of  $\text{CuCl}_2$ . Oxygen is then released in the decomposition reaction that results in the formation of molten  $\text{CuCl}$ . The proposed four-step cycle did not provide new venues to the challenges of electrolysis with solid products and hence it has not been pursued further. Nixon et al. [43] synthesized samples of  $\text{Cu}_2\text{OCl}_2$  by using  $\text{CuCl}$  or  $\text{CuCl}_2$  in contact with air between 325 and 400 °C. The synthesis was followed by further thermogravimetric decomposition at temperatures up to 580 °C. The experiments indicated a two-step reaction mechanism followed by vaporization of  $\text{CuCl}$ . Preliminary research and proof of concept experiments of a three reaction cycle were carried out at the Argonne National Lab and reported by Lewis et al. [32]. The new proposed cycle (No. 6) in Fig. 2.1 simplifies the process and reduces the capital cost while operating at a lower efficiency.

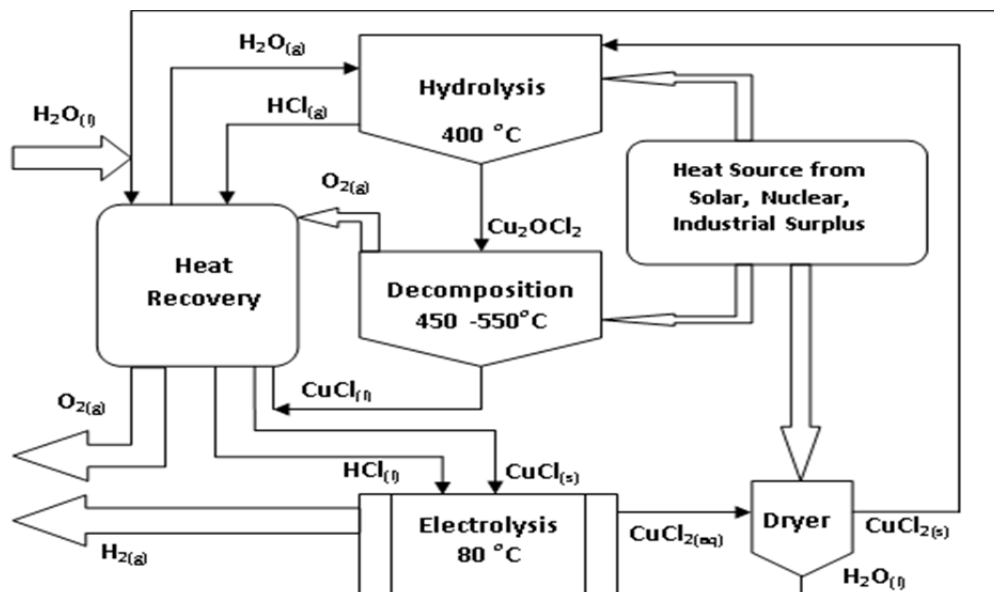


Fig. 2.1: Flow diagram of the three reaction thermochemical Cu-Cl cycle [44]

Additional research and recent development at UOIT has been reported by Naterer et al. [45, 46], Wang et al. [47], Daggupati et al. [48], and Marin et al. [44]. The proposed three chemical reactions cycle departs from the variations discussed before in that the electrolysis reaction did not include the formation of solid products. The three reaction cycle still presents a requirement for a drying step after aqueous  $\text{CuCl}_2$  is produced in the electrolytic reaction, although the possibility of integrating this step within the hydrolysis reaction is still under consideration.

Details of the three reactions of electrolysis, hydrolysis and thermal decomposition are indicated in Table 2.4. In contrast to the Sulfur-Iodine cycle where all reactants and products recycle in liquid and gaseous phases, the Cu-Cl cycle combines reactions where three phases are present, thus adding challenges to the continuity of the cycle.

Table 2.4: Processes and reactions in the thermochemical Cu-Cl cycle<sup>[44]</sup>

Step	Reaction	Step	T (°C)	Feed/Output*	
1	$\text{CuCl}_{(aq)} + 2\text{HCl}_{(g)} \rightarrow \text{CuCl}_{2(aq)} + \text{H}_{2(g)}$	Electrolysis, Exothermic	30 to 80	Feed:	$\text{CuCl}_{(l)} \text{ salt} + \text{HCl}_{(aq)} + \text{H}_2\text{O}_{(l)} + \text{V}$
				Output:	$\text{H}_{2(g)}$ and $\text{CuCl}_{2(aq)}$ , $\text{H}_2\text{O}_{(l)}$ , $\text{HCl}_{(aq)}$ [46]
2	$\text{CuCl}_{2(aq)} + n\text{fH}_2\text{O}_{(l)} = \text{Cu}_2\text{OCl}_{2(s)} + 2\text{HCl}_{(g)} + (n-1)\text{H}_2\text{O}_{(g)}$ $5 < n < 30$	Hydrolysis, Endothermic	375	Feed:	Slurry containing $\text{HCl}_{(aq)}$ and $\text{CuCl}_{2(s)}$ + Q
				Output:	Powder $\text{CuO} \cdot \text{CuCl}_{2(s)} + 2\text{HCl}_{(g)}$
3	$\text{CuO} \cdot \text{CuCl}_{2(s)} = 2\text{CuCl}_{(molten+vapour)} + 0.5\text{O}_{2(g)}$	Decomposition, Endothermic	530	Feed:	Powder/granular $\text{CuO} \cdot \text{CuCl}_{2(s)} + \text{Q}$
				Output:	$\text{CuCl}_{(molten)} + \text{O}_{2(g)}$
* Q = thermal energy, V = electrical energy					

The hydrolysis reaction of the three reaction cycle uses an aqueous solution of solid  $\text{CuCl}_2$  to react with steam at temperatures of 370 to 400 °C. This approach requires a previous step where the aqueous solution is preheated or the water is removed so that it does not inhibit contact with superheated steam in the hydrolysis reactor. The three reaction cycle thus requires an additional step where  $\text{CuCl}_2$  is dried by using low quality heat and then solid particles are fed into the hydrolysis reactor. Other physical steps may be required to support the reactions in the cycle including heat recovery, gas separation, water removal and separation of solids.

## **2.3 Three Reactions Thermochemical Cu-Cl Cycle**

### **2.3.1 Electrolysis Reaction**

The three reaction thermochemical cycle includes an electrolytic reaction at approximately 80 °C where the products are a solution of aqueous  $\text{CuCl}_2$ ,  $\text{H}_2\text{O}$ ,  $\text{HCl}$  and gaseous hydrogen. The design of the electrolyzer is expected to be simpler since a liquid is split to produce a mixture of gas and liquid, which is a mature technology and the capital cost is expected to be lower than electrolysis with solid products. Proof of concept experiments have been completed successfully and the electrolyzer is subject to further development at AECL (Stolberg et al. [49]) and UOIT where Naterer et al. [41] discussed recent advances in the electrolysis process. Furthermore, Ranganathan and Easton [50] performed electrochemical experiments to determine the suitability of materials for use in the electrolysis step of the cycle. The study characterized Amionisilane-based electrodes for use as anodes in the electrolyser and concluded that ceramic carbon electrodes (CCE) are a promising alternative for anode materials with good thermal stability.

At the electrolyser, the copper (I) ion is oxidized in the presence of hydrogen chloride to copper (II) at the anode, while the hydrogen ion is reduced at the cathode. The majority of copper species is anionic and thus cannot permeate through the cationic membrane. However, it has been reported that a considerable amount of neutral copper species exists and permeates through the membrane creating metallic deposits at the cathode, resulting in significant reduction of hydrogen production.

AECL has demonstrated the experimental operation of a CuCl / HCl electrolyzer while operating at current density of  $0.1 \text{ A/cm}^2$  and cell voltages in the range 0.6 to 0.7 V. Lewis et al. [51] reported results at the Pennsylvania State University of electrolyzer experiments operating at  $80 \text{ }^\circ\text{C}$  for 36 hours with  $0.25 \text{ A/cm}^2$  and 0.7 V. The results indicated hydrogen production in agreement with Faraday's Law. The goal was to achieve stable long term performance of the electrolyzer.

DOE proposed a milestone date of 2012 to optimize the electrolyzer design and reach a target of 0.6-0.7 V at  $0.5 \text{ A/cm}^2$  while operating a membrane electrode assembly (MEA) for at least one week. The objectives also specify that copper permeation should be reduced to 10% of that of Nafion® membranes at  $80 \text{ }^\circ\text{C}$ . The reported experimental results at AECL, UOIT and Penn State University have provided a lifetime expectation in agreement with the above goals, with a report on two membranes identified with copper diffusivity <10% of Nafion® and chemically and thermally stable at  $80 \text{ }^\circ\text{C}$  for over 40 hours.

However, longer duration experiments are required since electrolyzers tend to suffer slow degradation over time making lifetime projection experiments a critical aspect

in the determination of the best technology for this particular application. One particular challenge for the development will be the determination of the level of impurities that can be tolerated from the incoming stream of aqueous CuCl/HCl. A typical electrolyzer operation requires high levels of purification of the species before they enter the MEA, adding substantial cost and complexity to the operation.

### **2.3.2 Hydrolysis Reaction**

Significant challenges have been identified for the hydrolysis reaction. The stoichiometric reaction indicates that a half mole of water is required for each mole of copper (II) chloride to produce one mole of copper oxychloride ( $\text{Cu}_2\text{OCl}_2$ ) and two moles of hydrogen chloride (HCl). In a detailed kinetics analysis of the hydrolysis reaction, Daggupati et al. [48, 52] reported the occurrence of parallel competing reactions. In addition to producing  $\text{Cu}_2\text{OCl}_2$ , the reaction of  $\text{CuCl}_2$  and  $\text{H}_2\text{O}$  resulted in the production of CuCl and the release of oxygen and chlorine gas. The theoretical analysis concluded that high temperature favors higher equilibrium conversions, increased the decomposition of solid  $\text{CuCl}_2$  and the formation of free chlorine, a non-desirable condition for efficient operation of the cycle.

Experimental studies reported by Ferrandon et al. [53] confirmed the theoretical analysis and the need for water vapor in excess of the reaction stoichiometry. Experiments with molar ratios of steam to copper ( $\text{H}_2\text{O} / \text{Cu}$ ) above 20 resulted in conversions up to 92%. Thermodynamic simulations using Aspen Plus<sup>®</sup> indicated yields of 95%  $\text{Cu}_2\text{OCl}_2$  required the steam to copper molar ratio to be maintained near 17 with temperatures at 380-390 °C. At a steam to copper ratio of 5, the yield was only 30%. This

effect conflicts from an energy utilization perspective with a result that a higher ratio steam / Cu, yields a larger energy required for vaporization. Thus, there is a compromise between high yield and low energy consumption. The experiments were conducted with a carrier gas to remove HCl gas from the reaction zone.

The presence of a carrier gas in the hydrolysis reaction contributes to the removal of free chlorine and hence the incomplete conversion of  $\text{CuCl}_2$ . In a real situation, there is no carrier gas that will remove chlorine from the reaction zone and conversion rates should be higher. However, as the steam to copper ratio was allowed to decrease, more  $\text{CuCl}_2$  was available for decomposition, resulting in the production of  $\text{CuCl}$  and release of chlorine. In past experimental work by Ferrandon et al. [53] the phase composition of products was determined by powder X-ray diffraction. A quantitative analysis was performed and indicated the presence of  $\text{CuCl}$  and un-reacted  $\text{CuCl}_2$  in the solids. The amount of  $\text{Cu}_2\text{OCl}_2$  was determined based on the oxygen evolution from decomposition of the solid products in a catalytic reactor. At atmospheric pressure and a molar ratio of steam to  $\text{CuCl}_2$  of 10, the reaction yielded 60%  $\text{Cu}_2\text{OCl}_2$  and 7%  $\text{CuCl}$ . Reducing the reactor pressure to 0.4 bar resulted in a yield of 75%  $\text{Cu}_2\text{OCl}_2$  and 4%  $\text{CuCl}$ , with the balance of un-reacted  $\text{CuCl}_2$ . The experimental and theoretical studies indicated that the reaction can be achieved with high yields (of copper oxychloride and hydrochloric acid) when the molar steam to copper ratio is increased to between 7 and 20.

Daggupati et al. [52, 54] performed a chemical equilibrium analysis of the hydrolysis reaction to determine the impact of temperature, pressure and excess steam on the extent of reaction, and confirmed that low pressures result in higher conversion of

CuCl<sub>2</sub>. The thermodynamic analysis indicated that the steam to copper ratio can be reduced by decreasing the reaction pressure but this implies significant additional energy to balance the benefit of a reduced steam to copper ratio. The studies also concluded that the hydrogen chloride production step favours higher temperatures, excess steam and lower pressures. The study also suggested that the best operating conditions for complete consumption of chlorine during the hydrolysis reaction and minimization of excess steam occurs at temperatures of about 400 °C. Also, the partial pressure differences between the copper (II) chloride decomposition and the chlorine reverse reaction should be positive to facilitate the consumption of free chlorine. Under all circumstances, the presence of free chlorine needs be averted by a rapid reaction with CuO before it exits the reaction zone mixed with oxygen product.

Further thermal analyses of mixtures of CuCl and CuCl<sub>2</sub> by Biltz and Fisher (cited by Levy and Goreaud [55]) indicated a melting point of 422°C for CuCl and 630°C for CuCl<sub>2</sub>. According to the authors, the equilibrium of the reaction  $\text{CuCl}_2 \leftrightarrow \text{CuCl} + \frac{1}{2} \text{Cl}_2$  would lead to saturated vapor at 500°C of 133 Pa CuCl and 13 Pa CuCl<sub>2</sub> in a closed vessel. If the decomposition reaction is conducted in open atmosphere, a significant amount of chlorine would be released when above 380 °C. Lewis et al. [56] reported results of experimental hydrolysis in a fixed bed micro-reactor system. The focus of the experimental work was to find the parameters that maximize the yield of CuO\*CuCl<sub>2</sub> while minimizing the formation of CuCl. The hydrolysis reaction reaches equilibrium at conversion stages that vary depending upon the combination of temperature, steam ratio and pressure. Despite these advances, it is still not well understood what are the ideal conditions for hydrolysis to yield high conversion to Cu<sub>2</sub>OCl<sub>2</sub> and minimize side reactions

or unreacted products. The past literature indicated that incomplete hydrolysis reactions are expected at equilibrium with the presence of free chlorine,  $\text{CuCl}_2$  and  $\text{CuCl}$  in addition to  $\text{Cu}_2\text{OCl}_2$  in the products.

Removing chlorine gas from the  $\text{HCl}$  stream in hydrolysis and from oxygen in the decomposition reactor requires cryogenic processes that are energy intensive. Other technologies for removal of chlorine from a stream of gases have been reported in the literature. Lindbråthen et al. [57] examined low cost Polydimethylsiloxane (PDMS) membranes for the recovery of chlorine gas from gas streams in chloralkaly plants. The theoretical modeling of three different membrane materials including PDMS, surface modified glass and glass hollow fiber concluded that more research is required before membranes can economically substitute cryogenic processes for separation of chlorine from tail gas.

By-products of the hydrolysis reaction impact the operation further ahead within the cycle. The presence of chlorine with  $\text{HCl}$  gases may impact the operation of the electrolyzer. Free chlorine in the aqueous solution of  $\text{CuCl}$  may be a problem for the electrolytic reaction, shortening the life of the membrane and electrodes, or resulting in side reactions. The presence of  $\text{CuCl}$  does not impact the decomposition reaction further ahead since  $\text{CuCl}$  is a product of the decomposition of  $\text{Cu}_2\text{OCl}_2$  and therefore it is naturally present in the products. However, the presence of unreacted  $\text{CuCl}_2$  with the incoming  $\text{Cu}_2\text{OCl}_2$  results in decomposition of  $\text{CuCl}_2$  and further release of chlorine. Chlorine mixes with the oxygen product of decomposition and must be separated and captured before oxygen can be used or released to the atmosphere. Also, the continuous

loss of chlorine results in mass imbalances of the entire cycle requiring the addition of fresh HCl to the stream. Current research at UOIT is aimed at determining the equilibrium conditions of the hydrolysis reaction as a function of steam / copper ratios. Preliminary results suggest the possibility of obtaining high yields with ratios below 5, but this is still to be confirmed.

### **2.3.3 Decomposition Reaction**

The thermal decomposition of materials is usually called thermolysis in the literature involving calorimetric studies of materials. Thermolysis is commonly used in physicochemistry studies involving the relationship between intermolecular forces, reaction kinetics, chemical and physical properties. Thermal decomposition of materials is also associated with pyrolysis, the oxidation of materials at high temperature, and also associated to thermal degradation.

The influence of heat and mass transfer effects and the impact of temperatures, pressures, concentrations and mechanism of chemical decomposition are of major interest. The phenomena associated with chemical decomposition of solid particles that results in liquid and gaseous species with heat and mass transfer are complex. Few or no past studies address it in a comprehensive manner. A common approach uses a two phase analysis that oversimplifies the phenomena.

Naterer et al. [58] conducted a preliminary analysis of the integrated cycle with emphasis on heat recovery and overall resistances. They described the decomposition of copper oxychloride particles into molten salt and oxygen as a result of heat absorption

from the surrounding molten bath. The analysis considered solid particles descending in molten CuCl while experiencing thermochemical decomposition and oxygen gas bubbles ascending through the molten salt. Simultaneously, the liquid CuCl formed flows into the bulk of molten salt. The model described a particle that vanishes as the decomposition progresses. The analysis assumed that oxygen bubbles leave the molten salt immediately suggesting that resistances due to increased void fraction of gas in the thermally conductive molten salt may be negligible.

The decomposition of  $\text{Cu}_2\text{OCl}_2$  can occur through different competing reactions. Except for the two reaction variation discussed by Dokiya and Kotera [40] and the three reaction cycle suggested by Wang et al. [38], the cycles include the thermal decomposition of either  $\text{CuO}\cdot\text{CuCl}_2$  or  $\text{Cu}_2\text{OCl}_2$ . In both cases, the thermodynamic analysis indicated that maximum conversion and equilibrium is achieved around 530 or 535 °C. In all cases, the decomposition resulted in production of molten CuCl and gaseous  $\text{O}_2$  according to stoichiometric proportions. The decomposition of  $\text{Cu}_2\text{OCl}_2$  and the possible competing reactions were first discussed by Levy and Goreaud [55] and two possible reaction paths were identified. The analysis concluded that the thermal decomposition occurs as a combination of these paths where copper oxychloride undergoes an intermediate path with CuO and  $\text{CuCl}_2$  present. Experimental results reported by Marin et al. [44] indicated that the decomposition reaction of  $\text{CuO}\cdot\text{CuCl}_2$  occurs in at least two steps and that the temperature and pressure of the system impact the presence of chlorine in the products. Preliminary experiments confirmed that when a mixture of  $\text{CuO}\cdot\text{CuCl}_2$  and  $\text{CuCl}_2$  product of hydrolysis is present in the oxygen reactor, chlorine is also released.

More modeling and experimental work is required in order to understand the parameters that determine the optimum yield of decomposition of  $\text{CuO}\cdot\text{CuCl}_2$ . Serban et al. [59] performed proof of concept experiments of the decomposition in cycle No. 6 of Table 2.3 by using  $\text{CuO}\cdot\text{CuCl}_2$ . Since this reagent can be synthetically obtained from stoichiometric amounts of  $\text{CuCl}_2$  and  $\text{CuO}$  at temperatures between 370 and 470 °C, the subsequent kinetic study was performed using mixtures of  $\text{CuO}$  and  $\text{CuCl}_2$ . Further thermogravimetric experiments assumed that the decomposition occurs as a two competing reactions where  $\text{CuCl}_2$  releases chlorine and then reacts with copper oxide to release oxygen. The decomposition occurred with intermediate release of  $\text{CuCl}$  and  $\text{Cl}_2$  first, followed by the production of  $\text{CuCl}$  and oxygen after the chlorination reaction of  $\text{CuO}$ .

A comparison of thermogravimetric curves with experiments of decomposition of  $\text{Cu}_2\text{OCl}_2$  reported by Levy and Goreaud [55] indicated that the decomposition of  $\text{CuO}\cdot\text{CuCl}_2$  behaves in a similar manner to decomposition of  $\text{Cu}_2\text{OCl}_2$ , with a Gibbs energy of reaction of 61.3 and 68.7 kJ/mol (25 °C) and equilibrium at 530 and 610 °C, respectively. These results agree with the Hess law for the enthalpy change, where the enthalpy of reaction for the production of either species results in the same enthalpy change and it is independent of the path of reaction as indicated in Fig. 2.2. The thermo-physical properties of  $\text{Cu}_2\text{OCl}_2$  were calculated from the properties of compounds and elements using regression constants and known data of the specific heat, enthalpy and entropy at the ambient temperature from NIST [60]. These studies suggest that the results of theoretical and experimental analysis of thermal decomposition of  $\text{CuO}\cdot\text{CuCl}_2$  provide

the adequate frame of reference for further development of the cycle, although further research is recommended.

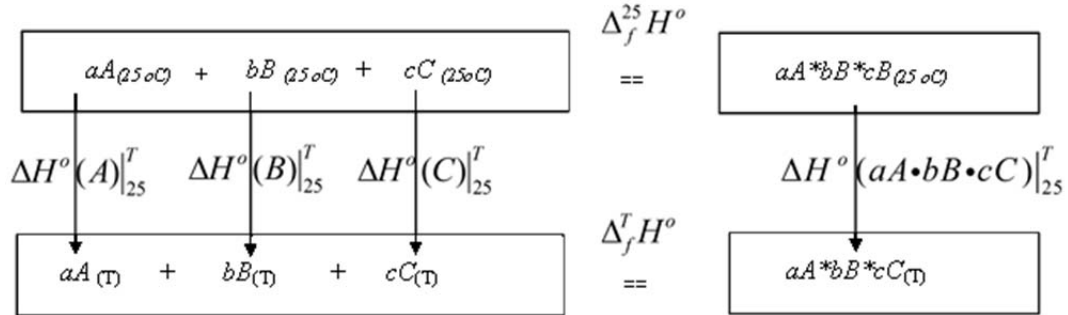


Fig. 2.2: Typical path for thermodynamic calculations of reactions

The thermodynamic path in Fig 2.2 and used in this thesis is applied to the endothermic decomposition of well-mixed, dehydrated, equi-molar samples of solid  $\text{CuO} + \text{CuCl}_2$ . It was assumed that the mixture decomposes through a first order reaction that resulted in gas and liquid release.

The experimental decomposition of  $\text{CuO} * \text{CuCl}_2$  resulted invariably in an equilibrium mixture of products indicating some degree of reverse reaction. Depending on the average temperature of the reaction, conversions of 60 to 95% were obtained. The conversion rate was confirmed via XRD analysis and quantification of the products of decomposition. There is no evidence in the past literature of experimental work on the reverse reaction in isolation. The reverse reaction was reported by Lamberti et al. [61] as one of three reactions in a process of oxychlorination for the recovery of HCl produced by the cracking of 1,2-dichloroethane. Although no experimental evidence was provided, the hypothesis of three reactions was supported through spectroscopy analysis of products to determine the presence of CuO as a shifted phase in the spectrum. The reactions occurred

in the presence of  $\text{CuCl}_2/\text{Al}_2\text{O}_3$  catalyst along with the interaction with reagents. Although no conclusive evidence can be taken from the analysis, it suggested that the reverse reaction may occur in the presence of a catalyst. This situation however is not present in the decomposition reaction in the thermochemical Cu-Cl cycle..

A detailed analysis of one possibility of the reverse reaction was discussed by Marin et al. [62] and results were confirmed with XRD analysis of experimental samples of bubbling oxygen in molten  $\text{CuCl}$ . Furthermore, other potential reactions are the result of the presence of water from hydrolysis. A kinetics study of halides decomposition by Ramumarthy and Secco [63] indicated that a compound in the form of  $\text{Cu}(\text{OH})\text{Cl}$  will decompose at temperatures between 230 and 280 °C to produce  $\text{CuO}$ ,  $\text{CuCl}_2$  and  $\text{H}_2\text{O}$ . Marin et al. [44] discussed results of experiments and analysis to understand the possible paths for the thermal decomposition of  $\text{CuO}\cdot\text{CuCl}_2$  by following two proposed paths discussed in the literature. First, a mechanistic approach to the decomposition of  $\text{Cu}_2\text{OCl}_2$  was reported by Levy and Goreaud [55] with two competing reactions. Measurements were conducted at temperatures between 375 and 550 °C. The XRD measurements indicated the presence of a larger amount of  $\text{CuCl}_2$  compared to  $\text{CuO}$ .

A second possible path for the decomposition of a mixture of  $\text{CuO}$  and  $\text{CuCl}_2$  was reported by Serban et al. [59]. The experiments used an equi-molar mixture of  $\text{CuO}$  and  $\text{CuCl}_2$  in a vertical reactor at 500 °C. The XRD analysis of the solid products indicated that the solid phase is pure  $\text{CuCl}$ . The analysis concluded that oxygen evolution is limited by the decomposition of  $\text{CuCl}_2$ . The reaction was assumed to occur in two stages, with

intermediate release of chlorine in the first step and displacement of oxygen in the second step producing a mixture of chlorine, oxygen and copper (I) chloride.

Serban et al. [59] reported oxygen production above the amount indicated by equilibrium at the temperature of the experiment. The reactant for the oxygen production included  $\text{CuCl}_2$ . Thus chlorine gas is expected to be present in the products. Parallel experiments were conducted in a thermogravimetric analyzer to understand the thermal decomposition of  $\text{CuCl}_2$ . The decomposition temperature falls into the range of 390-450 °C. Similarly, experimental results indicated that the mix of  $\text{CuO} \cdot \text{CuCl}_2$  starts to decompose at temperatures above 430 °C. Results by Walter-Levy and Goreaud [55] indicated that  $\text{Cu}_2\text{OCl}_2$  is stable up to the temperature of 370 °C, with formation of  $\text{Cl}_2$  between 375 and 470 °C and products of decomposition including  $\text{Cl}_2$ ,  $\text{O}_2$  and  $\text{CuCl}_2$  beyond 475 °C. From the aspect of integration with its upstream hydrolysis reaction, this means if the extent of reaction in hydrolysis is below completion and the hydrolysis products contain un-reacted  $\text{CuCl}_2$ , when these hydrolysis products are decomposed in the downstream oxygen reactor, it will also result in the release of undesirable chlorine gas together with oxygen. This becomes a safety and efficiency concern since additional steps and energy are required to separate chlorine from the oxygen and recycle the gases back into the cycle.

## **2.4 Experimental and Theoretical Models**

Prior discussion explained the background for models to predict the conversion of solid  $\text{CuO} \cdot \text{CuCl}_2$  into copper (I) chloride and oxygen. To further understand the phenomena and resistances that result in equilibrium conditions in the decomposition of

CuO\*CuCl<sub>2</sub> particles, it was also necessary to develop theoretical models that complement the experimental work.

#### **2.4.1 Moving Interface Models**

Modeling of particles that change phase is often conducted by tracking a moving interface. Thermodynamics of a reaction that involves a diffusing species by implementing a moving boundary model was analysed by Chatterjee and Chaturvedi [64]. The model used a general formulation for a moving boundary problem in which heat is generated at the boundary due to an exothermic reaction involving a species which diffuses into a dispersed medium. They considered a reaction-diffusion moving boundary problem involving both heat and mass transfer due to a species that diffuses into a spherical porous solid reacting medium. Although this approach provided valuable information to minimize hot spots in the reactor, it did not account for resistances that impact the intrinsic reaction such as convective heat transfer away from the reacting surface.

A different approach to a phase change boundary problem where one of the boundary conditions induces solid-liquid phase change is known as a “Stefan problem”. The Stefan problem was first described and analytical solutions were first presented by Josef Stefan in 1889 with original work on the formation of ice in the polar seas. Several studies following thereafter to include more details are given by Vuik [65]. Ozisik [66] developed a coupled integral formulation to obtain an analytical expression for the location of the moving interface. Exact solutions of moving boundary problems that include melting or solidification are difficult because the location of the moving interface itself is not known. It is determined as a result of the solution itself. In most cases, exact

solutions can only be obtained for large times and infinite or semi-infinite regions. Exact solutions that represent melting of spherical particles do not exist and past studies have generally used approximate and numerical solutions.

Several numerical methods have been developed for the solution of the Stefan problem. Caldwell and Kwan [67] described and compared several methods for the numerical solution of one-dimensional Stefan problems. Typical solutions apply to melting in a half-plane, outward cylindrical solidification and outward spherical solidification.

The enthalpy method uses an enthalpy form of the energy equation and it is one of the most common methods. In the formulation, the enthalpy function is introduced such that it is satisfied at the interface as a discontinuity of the enthalpy. The terms represent the sum of sensible heat and latent heat, and the enthalpy follows the temperature function except where phase change occurs in which case there is a jump that is proportional to the Stefan number. Discretization of the heat equation then results in a set of non-linear equations. The enthalpy method provides a relatively easier path for implementation. The boundary immobilization method (BIM) uses a transformation of coordinates to transform the problem into a fixed boundary problem.

Similarly, the perturbation method uses a transformation by considering that the moving boundary is a monotonic function of time and it replaces the time variable with a moving boundary variable. This method is more elaborate and only works for small Stefan numbers. Other less common methods include the Heat Balance Integral Method (HBIM) and the Nodal Integral Method (NIM) where the space domain is discretized into

space-time nodes. These methods have been shown to be efficient, but require complicated formulations and often have convergence difficulties. A space-averaged time-dependent temperature and a time-averaged space-dependent temperature are then tracked at each node. Voller and Cross [68], developed a very accurate solution that starts with the enthalpy method. It demonstrated the application to two dimensional problems.

Dewynne and Hill [69] developed integral formulations for Stefan problems involving an infinite slab and inward solidification of cylinders and spheres. The proposed solutions were applied to Stefan problems where the initial temperature is different from the fusion temperature. The majority of applications assume that the solid phase is initially at the fusion temperature and that the moving boundary must be tracked as a function of latent heat. Dewynne and Hill [69] approximations included a pseudo steady-state estimate, large Stefan number expansion, and approximations based on integral iterations with a series solutions. The limitations of the solutions were discussed in view of problems of diffusion with simultaneous chemical reactions, although no solutions were provided. The authors used the Green function with mapping kernels to develop complex integral solutions for two-phase moving boundary problems involving slabs, cylinders and spheres.

Hsieh [70] presented numerical solution methods for Stefan problems with a moving heat front traveling at a constant velocity in a fixed direction. The method transformed the problem to moving coordinates and used a Laplace transform to develop exact solutions in quasi-steady state over short periods of time. This method applies to

extrapolation of well-known phenomena, thus not recommended given the limited current understanding of the decomposition reaction that may not result in adequate predictions.

Lenvenspiel [71] presented two methods to analyze a particle undergoing a non-catalytic chemical reaction: the progressive conversion model and the shrinking unreacted core model. A detailed discussion of the shrinking core model indicated that the model is not applicable to situations where a solid reacts as a result of heating only without interacting with other species. The shrinking core model was used by Daggupati et al. [48] in the hydrolysis reaction of  $\text{CuCl}_2$  and steam to predict the rate of formation of HCl and  $\text{CuO} \cdot \text{CuCl}_2$  in the Cu-Cl cycle. In the progressive conversion model, a reactant gas diffuses into the particle and solid reactant is converted continuously and progressively throughout the particle. A solid crust forms on the surface as the gas diffuses through to reach the solid core. In the shrinking core model, the reaction occurs first at the outer surface and the zone of reaction then moves into the solid, leaving behind completely converted material. However, when a solid is converted under the influence of heat transfer, there is an important exception to the shrinking core model.

Ishida and Wen [72-74] conducted comparisons of kinetic and diffusion models for solid-gas reactions and reported that the shrinking core model is the best representation for a majority of reacting gas-solid systems with two exceptions: (i) The situation of a slow reaction of a gas with a very porous solid; and (ii) the situation of solid conversion under the action of heat transfer only. The shrinking core model considers the resistances of reactant gas entering the particle by diffusing through the reacted film. This resistance exists in the opposite direction to the heat flow in the case of a particle of

copper oxychloride undergoing endothermic decomposition. Thus, the transport phenomena of thermal decomposition will be analyzed through a combination of experimental and theoretical models.

#### **2.4.2 Chemical Reaction Models**

A parallel approach to the solution of a moving interface by Brown and Churchill [75] and Guffy [76] suggested methods for approximation of planar solutions applicable to spherical coordinates in order to obtain the temperature profile within the melting spherical particle through a Fourier series. The method applies to particles with low thermal conductivity and a Biot number larger than 1. Mosally et al. [77] applied a heat balance integral method to a single-phase Stefan problem. The rationale was based on the use of appropriate exponential functions in place of polynomials in order to enhance the solution accuracy of heat balance integrals. The method requires a sound understanding of the governing functions that define the temperature profile and relies on the proper identification of a realistic exponential function. Dewynne and Hill [69] considered the melting of initially sub-cooled solids in planar, cylindrical and spherical geometries. The integral-differential equations enabled the integration of the interface movement within upper and lower bounds. The enthalpy method was also applied by using the numerical temperature profiles to evaluate the integrals of the heat equation. The method did not converge to solutions for small times of interface movement.

Scale-up of chemical reactors is usually implemented after detailed understanding of the kinetics, thermodynamics and mass and heat transport resistances of the reactions have been properly understood. It is unpractical to build reactors to try all possible

combinations of conditions for a reaction to occur. Engineers rely on proof of concept results and small sample lab experiments to obtain preliminary conclusions on the configuration of reactors. Furthermore, theoretical models supported by experimental data with small samples are normally used. Average mass and heat transfer coefficients are determined with theoretical-experimental models and applied to the design and scaling-up of reactors.

Hoon and Tin [78] used an external mass transfer model for quiescent enzyme systems. The model used theoretical mass transfer correlations of the Reynolds and Schmidt numbers to predict the hydrolysis of palm olein immersed in immobilized lipase. The proportionality and power constants of the mass transfer equation were determined by experimental work. The model used the apparent reaction rate by tracking the inlet and outlet concentrations of palm olein in the column and assuming that the column is perfectly mixed. A mass balance was applied to the reservoir for determination of the residence time. The rate model assumed a first-order reaction on the surface of a particle to determine the rate constant by using the slope of the experimental curve of concentration vs. time. The mass balance equation was then integrated to obtain an apparent rate of reaction expression. The surface first-order reaction rate constant was then combined with the rate of external mass transfer in order to identify the contributions of mass transfer resistances at constant temperature. Thus, a microscopic-level decomposition model of a solid particle describing the rate of movement of the interface resembles the rate of reaction when modified by the overall resistances (Cussler [79]). The mass transfer correlation model was presented in terms of dimensionless numbers making it useful for design and simulation of the reactor performance.

In a similar approach, Leyva-Ramos et al. [80] modeled the adsorption of fluoride on bone char by using diffusion and kinetic models of particles in conjunction with experimental work of small samples. Bone char, also known as ivory black, is a granular material produced by charring animal bones and used to remove fluoride from water. The study used a diffusion model in three steps: external mass transport, intra-particle diffusion and the adsorption rate. The experimental adsorption equilibrium data at different temperatures and particle diameters were interpreted by using isotherms to determine rate constants with a least-square method. The kinetic models fitted satisfactorily the experimental concentration decay curves. However, the kinetics order varied considerably with operating conditions and the model did not explain the reason of the trend. This conclusion is typical in the process of finding the right model that predicts behavior of chemical reactions, diffusion, and heat and mass transport phenomena.

Cheung et al. [81] developed four different kinetic models to predict the sorption capacity of chitosan, a natural polymer used in water treatment, for copper ions. They recognized that the effect of transport phenomena and chemical reactions are often experimentally inseparable and that usually obey multiple order kinetics. Whether it is a reaction controlled process, diffusion controlled process or a combination of the two; this implied that the four models were used to find the best fitting equation which correlated the theoretical predicted data with the experimental data.

The methodology used by Hoon and Tin [78], Leyva-Ramos et al. [80] and Cheung et al. [81] discussed above used an experimental rate of reaction to complement the theoretical analysis and produce a reliable model. Analysis of small samples in

specialized reactors and associated techniques of thermogravimetric analysis (TGA) are often used to determine the kinetic parameters of a given chemical reaction. The experimental data are then fitted to linear regressions to obtain rate constants for concentration versus time, or temperature, or both depending on the nature of the reaction.

Wilburn and Sharp [82] conducted experiments under isothermal conditions and monitored the time required to reach 50% of reacted species. They then calculated the reduced time as  $t/t_{(50\%)}$  and generated graphs of conversion vs. reduced time. The procedure allows for comparison with existing and well known reduced time plots for different reaction mechanisms in order to determine the most probable type of mechanism followed by the reaction. Wilburn and Sharp [82] published a study of numerical data for nine commonly used solid state reaction equations and indicated that these reactions can be expressed as a function of the reduced time and a constant term that depends on the order of kinetics. They indicated that the procedure can be applied to reactions that are diffusion controlled or obey first order kinetics.

### **2.4.3 Experimental Data Fitting**

Singh et al. [83, 84] conducted experimental work on the decomposition of hydrogen sulfate salts of diphenylamine through isothermal and non-isothermal TGA. The reaction kinetics fitted an Arrhenius type equation, and spectrometric analysis observations allowed them to conclude that the decomposition is controlled by proton transfer with the formation of liquid and gaseous residuals. Further experimental work with thermal decomposition of arylammonium sulfates were fitted to the Avrami-Erofeev equation for kinetic orders 2 and 3 to obtain linear regressions of concentration vs. time.

The Avrami-Erofeev equation relates how solids transform from one phase to another during a chemical reaction. Avrami [85, 86] developed theories of kinetics of phase change supported by extensive experimental work. The analysis concluded that for a given substance, there is a range of temperatures and concentrations throughout which the kinetics of phase change in the characteristic time scale remains unchanged. This observation indicated that results of isothermal reaction curves can be used to describe phenomena under varying conditions of temperature and concentration. Similarly, Levenspiel [71] presented a detailed discussion of chemical reaction mechanisms, kinetics and reaction orders. A common procedure in the determination of kinetic order and energy of reactions indicated that chemical reactions are represented by a concentration dependent function and a temperature dependent function. The Arrhenius equation represents accurately the majority of chemical reactions where equilibrium conditions are dependent on temperature of reaction. The concentration function follows from the linear regression of concentration vs. time where several curve fitting mechanisms are suggested. The occurrence of several reactions competing in parallel suggests that the order of reaction is above 1. The Avrami-Erofeev correlation to the concentration curve applies to reactions that result in phase change and behave at orders between 2 and 3.

Researchers have used numerical methods in order to model the complexity of phenomena associated with particles immersed in a continuum, with several numerical strategies found in the past literature that are used to describe interfaces and their motion. Pfeffer and Happel [87] presented a solution to the problem of predicting particle heat and mass transfer rates in multi-particle, gas-solid phase systems. They used a free surface model and assumed that the fluid properties remain constant with temperature. They

applied a boundary condition function of a product of the dimensionless radius and the Damkohler number to model a diffusion phenomenon with a surface chemical reaction. The free surface model requires the introduction of special methods to define the location of the interface, its movement and its influence on a flow. The complexity of the method makes it necessary to use numeric solutions.

The free-surface method is often applied in computational fluid dynamics (CFD) It is used in cases where the density difference between the solid and gas is large. Sussman et al. [88] applied a sharp interface method for the computation of incompressible, immiscible two-phase flows. The method is suitable and robust even for large density and viscosity ratios to the order of 1,000 to 1. CFD methods are used to simulate the interaction of liquids and gases with surfaces defined by specific boundary conditions. They provide valuable information in situations of transonic or turbulent flow. The initial modelling of particles in a quiescent molten continuum can be modeled with computer tools that do not require the computer time required by CFD applications.

Robustness of a CFD method is defined in terms of its capacity to handle wide ranges of physical and geometrical parameters. The free surface method was successfully applied to several phenomena and configurations including a droplet under the influence of currents, bubble oscillation driven by surface tension, capillarity instability problems and in general, the determination of 3-D bubble dynamics. The method uses an Eulerian-Lagrangian framework in order to handle the immersed moving boundary. The Lagrangian method uses a grid that is embedded and moves with the fluid, thus immobilizing the interface, while the Eulerian frame allows for the continuous update

during calculations of the frame of reference. However, the past literature indicated the existence of other methods that may apply closer to the phenomenon of a particle undergoing decomposition.

Wang et al. [89] investigated the behaviour of a buoyancy-driven bubble rising in an infinite and stationary liquid. The solution used the Volume of Fluid (VOF) method and gave consideration to the deformation of the bubble with density ratios assumed as 0.001 and a viscosity ratio of gas to liquid at 0.01. The VOF method assumes a control volume of the size of the grid cell values of temperature, pressure, velocity, etc. The method is applicable to modeling of slurry reactors using computational fluid dynamics (CFD) but it requires large computational power.

Every method offers particular advantages and disadvantages. The past literature indicated that the methods discussed above were applied to phenomena occurring in two-phase environments. Different assumptions and simplifications were used to approach the solution of equations and results adjusted as required to simulate the phenomena. The complexity of thermal decomposition reactions occurs because heat and mass is transported simultaneously away from the solid particle with the gas phase, while heat transport occurs towards the solid particle through the liquid phase. The phenomena results from a thermochemical reaction, with the dynamics of each phase impacting the rate of decomposition. Thus further considerations are necessary before a model can be selected and developed.

#### 2.4.4 The Damkohler Number

The Damkohler number is a dimensionless number that relates the chemical reaction timescale to a parallel phenomenon occurring in the system such as the convective mass transport rate. It also relates the characteristic fluid time to the characteristic chemical reaction time. It provides a first approach to estimate the overall resistances that result in a lower heat and mass transfer rate and impact the residence time in the reactor.

Bazbauers [90] conducted experimental work to investigate reacting flows in which mixing rates have the same order of magnitude as reaction rates under conditions of interest. The experiments were conducted in a turbulent grid diffusion burner designed to operate under a wide range of temperatures and high dilution in order to create flat turbulent flames. The results of experiments were presented in terms of the Damkohler number. The complexity of the reaction and the dynamics was described in terms of the Damkohler ratio that indicated faster reaction rates than those obtained with mean values in the chemical kinetic analysis. Typical Da numbers have been determined for different types of reactions where the Da number can be used as a reference for preliminary design of reactors.

Fogler [91] discussed the applicability of Da numbers to several situations of chemical engineering. Da numbers below 0.1 indicate a slow dynamic and high reversibility, while a trend to Da numbers higher than 1 indicates fast dynamics with low reversibility. An equilibrium approach was used by Daggupati et al. [48] while analyzing a reaction where decomposition of  $\text{CuCl}_2$  results in liquid  $\text{CuCl}$  and chlorine gas. They assumed a steady-state process with equimolar counter-diffusion of species and also that

the concentration of gas in the bulk was lower than the interface based on equilibrium conditions. Equilibrium considerations are useful in estimating the variable concentration of species in the process of modeling the moving interface of a particle undergoing a chemical reaction.

#### **2.4.5 Momentum Analysis**

A significant number of publications reported on analysis and modeling efforts to determine the momentum of solid particles immersed in a continuum. Momentum analysis provides important information on velocities for the analysis of mass and heat transfer. Doichinova et al. [92] analyzed the dissolution of solid particles by considering a primary and secondary flow velocity within a control volume in a quiescent fluid. The former velocity is a result of the rate of change of radius of the particle, The second velocity results from a concentration gradient.

Krishna [93] used the Maxwell-Stefan diffusion equations that describe diffusion in multicomponent systems at steady-state under no velocity gradients. The model was applied to non-ideal liquid mixtures and it used a matrix method of representation for the numerical solution for a spherical particle immersed in a gaseous flowing stream. The analysis is based on a film model for a single particle and it assumed a constant gas composition at the surface of the sphere. Experimental evidence supports the applicability of the Maxwell-Stefan equation for the description of multicomponent mass transfer with binary diffusivities, where diffusivity is dominant over convective mass transport.

A rigorous calculation of the rates of mass transfer in mixtures with three or more components is complicated by the coupling between individual concentration gradients as

discussed by Smith and Taylor [94]. Furthermore, this coupling may result in species transfer in opposite directions to those expected due to reverse diffusion. They may not diffuse at all or may diffuse in the absence of any driving force. Such limitations imply in that exact analytical solutions for the general n-component case are only known for a film model of steady state, one-dimensional mass transfer. The analysis suggested that unless this is carefully addressed, diffusivity considerations can introduce significant errors in the modeling.

Yang [95] used a boundary layer divided into two parts, one towards the outer edge and the other adjacent to the surface, and a successive approximation method to obtain the solution in both regions. The analysis specifies the temperature at the outer edge and the interface with a profile in between. It recognizes an unsteady transport phenomenon due to the fast occurrence of mass and heat transfer. In such situations, assumptions of steady state are not representative of the phenomenon with a low Fourier number where the transport of heat through the thin interface occurs faster than the rate of thermal energy storage. Furthermore, the model assumed that the fluid motion relative to a spherical particle can be dominated exclusively by shear forces when the density difference between the particle and fluid is small. The shear forces provide a potential approach in situations of one dimensional mass transfer, whereas the combination of fluid stress from binary fluids at the solid surface is complex due to the independent contribution of different phases as in the case of decomposition of  $\text{CuO} \cdot \text{CuCl}_2$ .

Numerical modeling of moving interface phenomena in isothermal and non-isothermal processes applies to manufacturing processes that include mould filling, hot

rolling, hot metal forming, conversion and refinement of metals, among others. A numerical solution in the context of finite elements was discussed by Cruchaga and Celentano [96] and applied to thermally coupled flow problems with phase change effects. The numerical analysis was subdivided into two time-varying subdomains occupied by two different phases. They identified the main difficulties as a result of the convective effects, updating of the moving interface and the description of the phenomena in the presence of materials with large differences in physical properties, added to the release or absorption of latent heat. The study presented a numerical solution to the problem of incompressible thermally coupled flow, including interfaces and phase change effects. Chemical reactions were not considered in the additional complexity that arises from concentration driven diffusion and multiple phases as in the case of chemical decomposition of  $\text{CuO} \cdot \text{CuCl}_2$  in a molten salt with release of gas, liquid and simultaneous phase change.

Hughmark [97] reported correlations for continuous phase transfer coefficients for spherical solid particles and bubbles in turbulent fluid fields. The correlations were presented as dimensionless transport coefficients based upon the shear velocity, Schmidt and Prandtl numbers. The analysis assumed that the slip velocity was represented by the vector-addition of the particle-fluid velocity and the terminal settling velocity of the particle for a Reynolds number ranging from 0.1 to 1.

Gan et al. [98, 99] analysed the sedimentation of a dispersed phase in a continuum accompanied by the interfacial activity such as chemical reactions and phase change. The analysis considered a single particle with zero initial velocity and a solid to fluid density

ratio of 1.00232. It indicated that melting adds three elements of new physics to the dynamics of a particle: changing inertia and weight of the particle, the flow of the newly melted layer down the particle surface, and downward thermal convection induced in the neighbourhood of the particle. It was observed that at small Stefan numbers ( $Ste \ll 1$ ), there is little melting and the particle settles steadily along the centerline of the control volume. At the other extreme, with large Stefan numbers ( $Ste \gg 1$ ), melting is so rapid that the process do not have time to develop before the particle disappears. The velocity of the particle is characterized by the Grashof number based on the ratio of buoyancy to viscous forces. Modeling in the flow regime of  $0 < Gr < 500$  indicated that the particle accelerates monotonically, reaching a maximum and then declining with a loss of mass and eventually settling steadily. This effect that is more pronounced at higher Stefan numbers.

Grevrin and Masbernat [100] analysed bioreactors and particle–fluid interactions using continuity and momentum equations in both phases with an interfacial momentum term accounting for the drag force only. They considered that inertia forces have little effect and they obtained a form of terminal local velocity modified by the mole-fraction of the solid. Thelen and Ramirez [101] used a similar approach for solid fluidization in the Stokes flow regime by simplifying the momentum balance to an algebraic relation between drag, buoyant and diffusive forces. Zastawny et al. [102] derived drag and lift force expressions for non-spherical particles. They proposed correlations for the lift force, drag force, and torque caused by the rotation of a particle. They concluded that the behavior of non-spherical particles with a fluid flow is a complex subject even for axisymmetric particles and uniform flow.

Pfeffer and Happel [103] analyzed the dissolution of solid particles embedded in a concentric spherical volume of a size slightly larger than the volume of the particle. The spherical control volume was used for the initial calculation of concentrations by applying a spherical geometry relationship to determine the concentration of solid as a function of changing radius. The analysis used a velocity profile determined by tangential components of stress at the surface of the particle, as a result of drag forces on a sphere falling in a fluid field. The study assumed each particle in a cloud was limited to motion within a concentric mass of fluid and the authors applied a numerical solution to the case of a chemical reaction at the surface. They assumed a first order surface chemical reaction and solved the problem for a dimensionless concentration ratio. The ratio was calculated by integrating the local concentration over the surface of the particle. They found that the Damkohler number is a monotonic function of the dimensionless concentration of products, and concluded that the model can be applied to more complex surface chemical reactions.

Happel [103] developed a mathematical treatment on the basis that two concentric spheres can serve as a model for a random assemblage of particles moving relative to a fluid. The inner sphere comprises the particle and the outer sphere has the fluid envelope. The appropriate boundary conditions that result from these assumptions enabled a closed solution that satisfied the Navier-Stokes equations while omitting inertia terms from the assumed low density differences. A free surface model was adopted and a mathematical model developed in relation to experimental results with accuracy of +/- 15%.

Due to the unique properties of a spherical geometry, development of the appropriate continuity time-dependent differential equations provides a non-zero transfer rate when solved for steady state conditions as discussed by Nelson and Galloway [104]. This leads to the well-known value of 2 for the Nusselt and Sherwood numbers at zero Reynolds number. However, attempts to derive expressions for heat and mass transfer based on theories for a single particle will fail if applied to a highly concentrated dispersed phase. The consequence of the proximity of particles results in a boundary condition where the radial gradient of concentration / temperature is zero since flow is reduced and the Reynolds number approaches zero. The hindrance effect can also be seen from the convective effect of other species in the gaseous or liquid phase surrounding the particle. In the case of thermal decomposition of  $\text{CuO} \cdot \text{CuCl}_2$ , the net effect may result in hindrance of heat transfer and thus a reduced rate of reaction.

Froment and Bischoff [105] presented a detailed analysis of the phenomena occurring in a chemical reaction and developed a general set of equations that describe mass, energy and momentum transport in all types of reactors. The entire set of equations used to represent the general problem can be simplified depending upon the specific type of reactor. The expressions provide a general frame of continuity for a species reacting in a flowing fluid where the density, temperature and composition are varying as a function of time and position. One form of the continuity equation is then required to represent the phase in which one particular species is reacting. A boundary condition and generally a term linking heat transfer between phases are used to link the equations. An extension of Fick's law is used to express the molar flux in cases where the flow can be assumed linear or perfectly ordered. Also, appropriate multicomponent diffusion like the Stefan-Maxwell

equation can be used. Furthermore, when integral averages are considered over the spatial directions, the equations of continuity reduce to those of ideal reactors and they can be applied to a control volume element of the reactor. For many cases, the cross-sectional average values of concentration and temperature can be used in the equations instead of spatially distributed values.

Above treatments of the continuity equations provide a wide range of possibilities to approach the problem of chemical decomposition. Experimental data, regressions and theoretical models are necessary to develop a comprehensive understanding. No one single approach provides the solution without neglecting some aspects of the phenomena. Once the measurable physical quantities have been identified and the governing equations are established, it is important to understand the proportion of magnitude between the independent terms such that no effort is spent in solving terms that do not significantly impact the phenomena.

#### **2.4.6 Dimensional Analysis**

Ruzicka [106] presented an extensive discussion of dimensional analysis and scaling and the implications of using dimensionless equations in the analysis of the phenomena. The dimensionless equations are independent of the system of units while the dimensionless numbers are relevant to the problem in question. Furthermore, the dimensionless equations provide a measure of proportion between terms and they apply to similar systems in terms of geometry, kinematics, dynamics, etc., thus providing an important tool for scale-up of systems.

Dimensional analysis does not necessarily follow a rigorous procedure; the choice of physical quantities is highly subjective and it requires a solid understanding of the problem. The analysis should take into account the system geometry, material properties, kinematic and dynamic aspects and external conditions, among others. Even if the equations cannot be solved, a dimensional analysis provides an indication of the relevant quantities. For instance, the Peclet number indicates the coupling between the transport by hydrodynamic convection and mass transfer due to molecular diffusion. It can also be interpreted as the ratio of heat transport by convection vs. heat transport by conduction. The Reynolds number indicates the relative importance of inertial to viscous forces. The presence of these terms in a dimensionless governing equation indicates a measure of the relative magnitude of driving forces and provides new information for understanding of the phenomenon.

Astarita [107] discussed several examples of dimensional analysis and scaling and demonstrated how it can provide significant insight into the solution of the problem. In order to have the appropriate scaling, it is necessary to have prior knowledge of the processes as a result of experiments, physical intuition or numerical analysis of similar cases. The limited understanding of the experimental decomposition of  $\text{CuO} \cdot \text{CuCl}_2$  indicated that it is a result of complex competing convective and diffusive heat and mass transfer phenomena where dimensional analysis provides a tool for simplification of the governing equations.

## **2.5 Experimental Methods**

A combination of experimental work and modeling is necessary to verify the hypothesis of this thesis. Several types of thermal experimental techniques exist as

discussed by Scott [108]. The basic techniques include thermogravimetric Analysis (TGA), Differential Thermal Analysis (DTA), Differential Scanning Calorimetry (DSC), Thermo Magnetometry (TM), and Dielectric Thermal Analysis (DTA). TGA, DTA and DSC are complementary techniques which can be performed simultaneously. A review of techniques suggested that TGA is an appropriate technique to monitor thermal decomposition of materials, among others. The results of TGA are usually reported in the form of curves relating mass lost from the sample against temperature or time. Furthermore, past literature reported some data of decomposition of  $\text{CuCl}_2$  using TGA. This data were found useful when comparing possible paths of decomposition.

Past literature indicated that TGA is the best technology that allows comparison with other experimental setups where the majority of experiments were conducted, namely a vertical split reactor and heating mantles. Each technology enabled the observation of the phenomena from different perspectives. TGA also has the capability to decompose small samples while supplying a predetermined constant heat rate and monitoring weight losses. The sample is contained in a closed chamber and the environment is continuously purged with a predetermined flow of inert gas. The temperature of the sample is closely monitored through a thermocouple. Unless integrated with a mass spectrometer, it does not provide for monitoring of the composition of gas or vapor species. It provides valuable data for the analysis of ratios of decomposition.

A heating mantle is a less stringent environment where temperature control provides feedback for the on-off operation of a resistive heater that transfers heat to the vessel containing a sample mainly through convection and conduction. It provides for an

open environment where the sample can be observed directly as the phenomena occurs. It was set following recommendations outlined by Moffat [109]. A heating mantle does not have provision for weight or gas monitoring. Split reactors are commonly used for research purposes and they provide a starting point for customization to fit the requirements of the reaction under investigation. Reactors allow for the decomposition of larger samples and can be arranged for continuous monitoring of gaseous species flowing in and out of the reactor. Reactors are limited by the access to information on weight of the sample only before and after the experiments.

## **2.6 Uncertainty and Error**

With experimental data from different equipment and the possibility to compare the information, it is critical to understand the magnitude of error in each set of measurements. The inherent error of experiments and subsequent interpretations and calculations can be determined by the Kline and McClintock method for experimental uncertainty [110] and the discussion by Moffat [109]. The method describes a systematic approach to determination of uncertainty with consideration for the true value and the measured value. It is however rare that the true value is known unless it can be determined from baseline experiments, conservation laws or the exact solution. The uncertainty attributed to a measurement is an estimate of the possible residual error after all corrections have been made.

Thus, the uncertainty is determined by the residual error after corrections, not the original error. Therefore, as explained by Moffat [109], the list of effects that must be counted as possible error sources depends on which criteria are applied to select as the definition of a true value. For instance, in the case of a temperature measurement, the true

value may differ between the value achieved at the thermocouple junction or the mass-averaged value that the sample may have achieved if the instrumentation had not disturbed the flow distribution. Moffat [109] considered several possible effects in between, pointing clearly to the relative nature of error observation and measurement.

The Kline-McClintock method for uncertainty calculation focuses on the coarseness of measuring tools. Thus it provides results of a 95% confidence of the experimenter of the band within which the mean of the many measurements would fall; and the magnitude of the fixed, constant error where the experimenter is 95% confident that the true value bias error would be less than a bias limit. The Moffat method relies on the relative definition of a true value. On the other end, the Kline-McClintock method relies on the precision that occurs from observation of the mean. In both situations, observance of the fixed error or bias of instruments does not produce subjective observation of error.

## Chapter 3 – Experiments on the Decomposition Reactor

---

### 3.1 Approaches to Experimental Work

The experiments in this thesis were designed to satisfy the following criteria.

1. Obtain a direct measure of mass loss / gain whether gas or solid to simplify the interpretation of data and facilitate a comparison of results from different techniques.
2. Collect data of measurable variables and obtain the time averaged value in order to characterize the analysis.
3. Use raw species that represent products from hydrolysis at equilibrium conditions.

A common direct method of mass loss tracking includes thermogravimetric analysis that is performed at isothermal or variable temperature conditions. The analysis can also be conducted under constant heat flux conditions. Thermogravimetric analysers are designed specifically for these situations and the data is automatically collected. Other techniques for thermal decomposition used a simple Erlenmeyer flask heated from the bottom in a heating mantle. The initial mass is then compared to the final mass and the difference corresponds with the mass of volatiles. A third technique used a split reactor connected to a series of sensors in order to monitor the evolution of volatiles in a continuous manner. Weight differences are then compared with the mass of volatiles measured and decomposition rates calculated. The three techniques were used in the experimental analysis of decomposition of a mixture of  $\text{CuO} \cdot \text{CuCl}_2$ . Each technique provided a different set of information that was correlated with consideration to its limitations.

### 3.2 Experimental Apparatus and Set Up

A review of thermal experimental techniques indicated that TGA is an appropriate technique to monitor the thermal decomposition of materials. The results of TGA are usually reported in the form of curves relating the mass lost from the sample against temperature or time. TGA also has the capability to decompose small samples while supplying a predetermined constant heat rate and monitoring weight losses. The sample is contained in a closed chamber and the environment is continuously purged with a predetermined flow of inert gas. The temperature of the sample is closely monitored through a thermocouple in direct contact. Unless integrated with a mass spectrometer, TGA does not provide for monitoring of the composition of gas or vapor species. It provides valuable data for the analysis of rates of weight loss that can then be correlated to decomposition rates. Experiments were repeated under similar conditions of initial mass and molar ratios, initial weight, and purge gas flow at atmospheric pressure.

Isothermal experiments were conducted in a thermogravimetric analyser. The TGA experiments used the SDT Q600 equipment with a sample capacity up to 200 mg on a microbalance, sensitivity of 0.1  $\mu\text{g}$  and precision of  $\pm 2\%$ . The instrument provides measurements of heat flow and weight change. The temperature of the sample is monitored and controlled via type R, platinum-rhodium thermocouples. Special care was taken in the preparation of samples for the TGA experiments due to the small size of the samples. A 10 g sample was placed and thin-spread in the oven at 150  $^{\circ}\text{C}$  for 24 hours and then carefully packed in a sealed glass container. The samples were then placed in the chamber and the following standard procedure was used: Continuous purge with 50 ml/min gas argon; Initial equilibrium and isothermal for 5 minutes at 30  $^{\circ}\text{C}$ ; Temperature

ramp up at 20 °C/min to 110 °C; Isothermal to equilibrium for 10 minutes; Temperature ramp up at 20 deg C/min to the desired temperature of decomposition (i.e., 450, 470, 490, 510 or 530 °C); Isothermal for up to 120 minutes incremental; Stop measurements and set air cooling on. The samples consisted of 30 to 55 mg of CuO\*CuCl<sub>2</sub>. The results were analyzed using the accompanying Universal Analysis 2000 data analysis software.

A heating mantle is a less stringent environment where a gross temperature control provides feedback for the on-off operation of a resistive heater that transfers heat to the vessel containing the sample through convection and conduction. It does not have provisions for weight monitoring. It provides for an open environment where the sample can be observed directly as the phenomenon occurs. The thermocouples were protected from the oxidizing environment by means of a thermo-well and set following recommendations outlined by Moffat [109].

Split reactors are commonly used for research purposes and they provide a starting place for customization to fit the requirements of the reaction under investigation. Reactors allow for the decomposition of larger samples and they can be customized for continuous monitoring of gaseous species flowing in and out of the reactor. Reactors are limited by the access to information on weight of the sample only before and after the experiments and data are obtained to be representative of average quantities. The vertical split reactor was set as indicated in Fig. 3.1 and 3.2 for the forward and reverse reaction respectively.

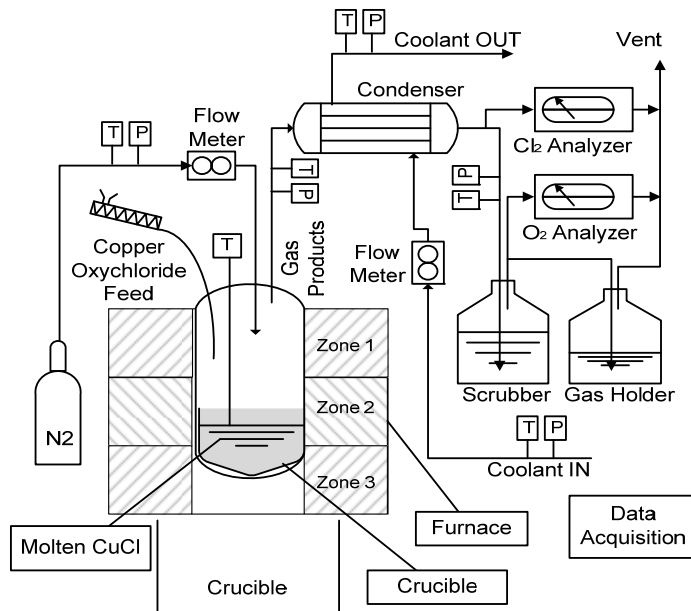


Fig. 3.1: Experimental apparatus with vertical split reactor for chemical decomposition

### 3.3 Chemicals and Materials

Prior to the start of experiments, the samples were prepared from chemicals of commercial grade. This selection of material represents levels of impurity typical of products from hydrolysis. Also, in order to minimize contamination of the oxygen gas generated, the carrying gas nitrogen was selected at ultra-high purity of 99.999 %. This level of purity implied a maximum background noise in the oxygen analyzer of 0.001%. Table 3.1 indicates the chemicals and corresponding impurities in the experiments.

Table 3.1: Chemicals used in experiments

Species	ACS Grade	Impurities
CuO	> 99%	< 0.02% insoluble
CuCl <sub>2</sub>	> 99%	< 0.01 % insoluble
CuCl	> 90%	< 0.02 % insoluble
N <sub>2</sub>	99.999%	O <sub>2</sub> , Ar.

The forward reaction experiments conducted with TGA and the vertical reactor used a stoichiometric mix of CuO and CuCl<sub>2</sub> with continuous purging of nitrogen gas. Experiments to study the evolution of chlorine from incomplete hydrolysis were performed in the heating mantle and the vertical reactor. These experiments used samples of CuO\*CuCl<sub>2</sub> with 20% excess CuCl<sub>2</sub>. Similarly, the reverse reaction experiments used a bed of CuCl with total air injection of 2 molar above stoichiometric requirements.

The aggressive nature of chemicals and the high temperature experiments required special considerations and careful selection of reactor materials. Also, the materials in contact with reactants and products were selected to not decompose during the reaction and result in contaminated species. Preliminary experiments were performed in order to select the most feasible materials. Pure copper was proposed as containment and for thermo-wells. The thermo-wells rapidly diluted, disappeared and exposed the thermocouple to the corrosive environment of molten CuCl. Pyrex containment was proposed and quartz was finally selected and used in several preliminary experiments. Although quartz handled the corrosive and high temperature exposure without visible degradation, it did not withstand the process of removal of the solid sample after experiments were completed. The high cost of quartz containment and regular breaking prompted the search for alternative containment materials.

Table 3.2: Materials used in the vertical reactor

Material	Location	Maximum Temperature, °C	Fluid / Species
Stainless Steel 316	Secondary containment reactor	630	CuCl vapours, Cl <sub>2</sub> gas, O <sub>2</sub> gas
Alumina	Primary containment	550	Molten CuCl, Cl <sub>2</sub> gas, O <sub>2</sub> gas
Hastelloy C	Thermo-well	550	Molten CuCl, O <sub>2</sub> gas, Cl <sub>2</sub> gas.
Stainless Steel 316	Discharge ports	350	O <sub>2</sub> gas, N <sub>2</sub> , CuCl vapours
PTFE tubing	Feed/discharge ports	100	O <sub>2</sub> gas, Cl <sub>2</sub> gas, CuCl vapours
Stainless Steel 416	Feeding ports	Ambient	CuO*CuCl <sub>2</sub> , Air, N <sub>2</sub> , CuCl <sub>2</sub>

Test experiments were conducted and coupons of several materials were placed in a crucible with a CuCl sample and brought to temperatures above 500 °C. The sample was contained in crucibles of alumina, and the thermocouples used thermo-wells of Hastelloy C. Materials tested and locations within the reactor are indicated in Table 3.2. Although hastelloy C and SS 316 were selected for the most stringent applications, chemical attack and corrosion were evident. The corrosion rate however was slow enough for practical application during experimental testing.

### 3.4 Forward Reaction

For the forward reaction, heat is supplied to the reactor by a 100 cm vertical split-type furnace with three heating zones, independently controlled via SCR power control modules, and with a PID control interface. The furnace can operate within 1 deg C of the targeted temperature and within the range of 50 to 1000 °C. The heating zones are independently powered for further heat flux control, and independently controlled via one

type K thermocouple for each heating zone. This arrangement provides a uniform temperature field to the reactor. The body of the reactor and pipes are made of stainless steel 316 and hastelloy-C, and the crucible containing the sample is made of ceramic.

The reactor chamber provides secondary containment to the sample, channelling the gases outside via a liquid seal that maintains back-pressure within the chamber slightly above atmospheric pressure. A pressurized reactor prevents atmospheric gases from entering and contaminating the products of the reaction. One stream of gas products is directed to an ABB-AO202 chlorine gas analyzer that provides readings in a continuous manner, with linearity of 1% of span and repeatability of 0.5% of span. Continuous time correction is applied to readings to compensate for instrument response time and space velocity of the sample. A second stream is directed to an on-line oxygen gas analyzer that uses a zirconium oxide sensor with five sensing ranges and a sampling pump connected in parallel. The oxygen analyzer is calibrated with analytical grade (99.999%) nitrogen for zero reading and atmospheric air for span reading. The AMI-201RSP continuous oxygen analyzer has five selectable ranges of operation, minimum detection of 0.01% and repeatability of +/- 0.2% of range. The error of readings of gas composition, including the calibration gas and response time of analyzer, was estimated at 1%.

The CuCl vapour tends to travel with the gases product of decomposition. In order to overcome this problem, a condenser is installed on the discharge of the reactor. Carrier gas nitrogen is injected in the reactor at constant pressure and continuous flow is measured via an O-FMA1600MA differential pressure mass-flow-meter with +/- 0.8% reading accuracy, +/- 0.2% repeatability, and pressure / temperature compensation.

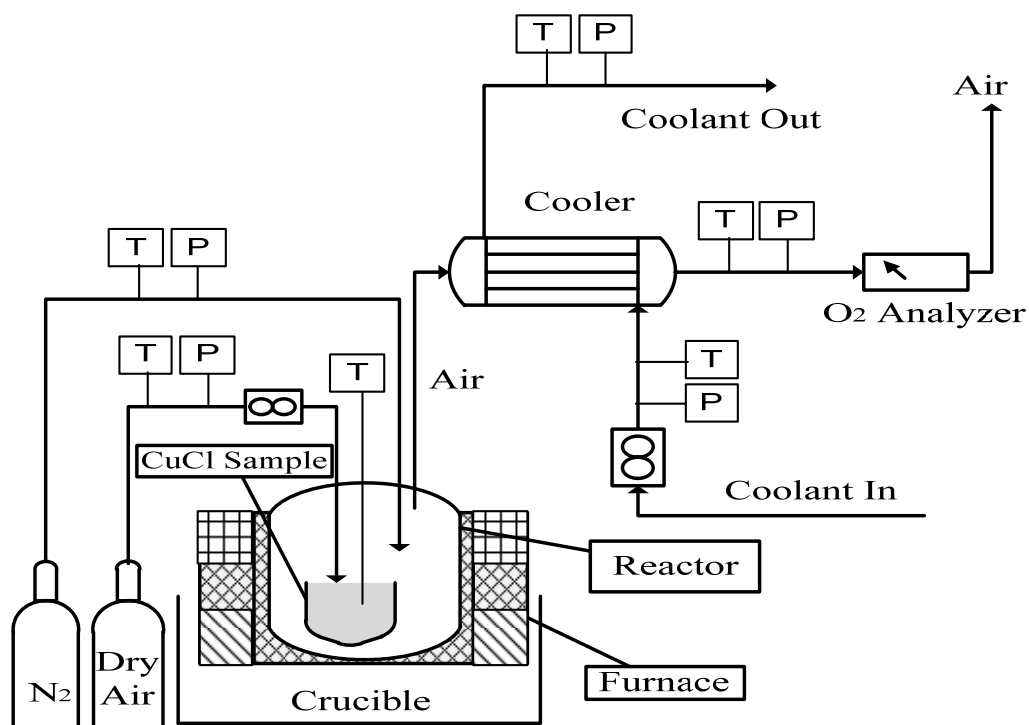


Fig. 3.2: Experimental configuration for the reaction of molten CuCl and O<sub>2</sub>

Temperatures of streams in and out of the reactor are monitored via type K thermocouples with integrated 4-20 mA INOR transducers with an accuracy of +/- 0.2%. The initial load of solid reactants and the remaining solid products are measured via a Mettler Toledo ML3002E weight scale with repeatability of 0.01 g and linearity of 0.02 g. Previous to the initiation of experiments, the solid reactants are placed in the oven for a minimum of 24 hours at 150 °C. Once inside the reactor, a chemically compatible crucible capable of withstanding high temperature holds the sample of solids with the immersed temperature measurement probe. The temperature probe is protected and isolated from the oxy-reducing environment via a thermo-well. The sample is placed inside the reactor, and the reactor is closed and purged with nitrogen to eliminate any traces of oxygen. When oxygen content is at undetectable levels, the furnace is turned on

and allowed to heat the sample. When applicable, at the sample temperature of 450 °C, further addition of reactants is initiated. . Experimental data was recorded with a frequency of 1 second using the NI-DAQmx 7.0 from National Instruments.

### **3.5 Reverse Reaction**

For the reverse reaction, the reactor setup shown in Fig. 3.2 contains a crucible that can withstand a very high temperature and it is chemically inert to both solid and molten CuCl. The crucible contains the sample and holds the probes for air injection and temperature measurement. It is located inside of a heating chamber surrounded by the top heating zone of the furnace. The inside diameter of the crucible varies from 5 - 8 cm so as to study the influence of the relative volume of CuCl. The heating chamber also provides secondary containment and it is used to purge the reaction environment from humidity and oxygen by using nitrogen. In the experiments, solid CuCl is fed into the reactor and heated to a molten state, and then air is bubbled through the molten CuCl at various temperatures. A perforated air distributor was used to increase the contact of bubbling air with the molten salt. No attempt was made to measure the effects of interfacial contact area between bubbles and molten CuCl since the objective of the experiments was to verify the possibility of the reverse reaction, independent of the efficiency. The gases exiting the heating chamber are cooled down to ambient temperature via a heat exchanger. The gases are then sampled continuously with an oxygen analyzer for observation of the content of oxygen.

The total quantity of reacted oxygen can be determined from integration of the concentration curve and the flow rates of air which are monitored in a real-time mode.

The oxygen quantity was calculated by assuming ideal behaviour as follows:

$$\dot{m}_{O_2} = \frac{1}{22.4} (p_{O_2}) (F_{N_2}) \left( \frac{P_1 T_2}{P_2 T_1} \right) \quad (3.1)$$

In this equation,  $P_1$ ,  $T_1$  and  $P_2$ ,  $T_2$  represent the pressure and temperature at the inlet and outlet conditions, respectively. Also,  $p_{O_2}$ ,  $F_{N_2}$  and  $\dot{m}_{O_2}$  represent the partial pressure of oxygen, flow of nitrogen and mass flow of oxygen, respectively.

The solid products of reaction were analyzed by x-ray diffraction (XRD) with a PANalytical X'pert diffractometer where the diffraction angle 2-Tetha was allowed to change between 5 and 60 degrees. Subsequent quantification used the X-pert PANalytical quantification software.

### 3.6 Uncertainty and Error

The collected data was used for the generation of the rate of reaction. Each data set collected through different techniques brings intrinsic errors that must be carefully understood and analyzed. The inherent error of experiments and subsequent interpretations and calculations were determined by following the method for experimental uncertainty as outlined by Kline and McClintock [110] and the discussion by Moffat [109]. The cumulative volume of gasses generated at standard conditions is obtained by integrating the curve of the mass balance over the time period. The mass balance of gases is calculated by using Raoult's law for the mole fractions and partial pressures in parallel with a mass balance as follows:

$$F_{out} = F_{N_2} + F_{O_2} + F_{Cl_2} \quad (3.2)$$

The volume of gas yielded results from the integration of the instantaneous curve of gas produced vs. time:

$$V_{O_2} = \int_{\tau_1}^{\tau_2} X_{O_2} F dt \quad (3.3)$$

The mass loss from the mixture of  $CuO \cdot CuCl_2$  reactant is measured as the difference between the weights of the full and empty crucible, and before and after the reaction:

$$M_{solids} = \Delta m_0 - \Delta m_1 \quad (3.4)$$

Table 3.3: Summary of measurement assumptions and uncertainties

Parameter / Procedure	Range	Bias	Precision	Error %	R <sup>2</sup>
Nitrogen flow meter	0-2 SLPM	0.8	0.2		
Percent oxygen	0-25%	0.01	0.2		
Percent chlorine analyzer	0-10%	1.0	0.5		
Reactor temperature	370-1000 °C	0.2	0.1		
Reactor pressure	0-5 bar	0.6	0.06		
Weight Scale	0-400 g	0.0002	0.0001		
Reactor data acquisition	0-24 mA	0.12	0.1		
Reactor conversion curve fitting				3.6	0.9835
Zero intercept reactor conversion curve fitting				20.0	0.9898
Reactor temperature fitting					0.9534
TGA weight measurement			0.2		
TGA conversion curve fitting				1.5	0.9908
TGA temperature curve fitting					0.9030
NIST Cu, Cl <sub>2</sub> , O <sub>2</sub> data			0.08		
Uniform density solid and liquid	4.83 - 4.18			13.5	
Average density at equilibrium				8.97	
Average numerical error (local)	%			0.01	
Bias and Precision values are +/-					

Uncertainty calculations were taken over a representative time period of the experiments. Experiments were repeated under similar conditions of initial mass and molar ratios, initial weight, reactor pressure and purge gas flow. A steady set of readings from the data acquisition system was selected over a time period for uncertainty calculations. The uncertainty of the total mol evolution was calculated as 1.28%, and determined by following a combination of precision (random) contributions to the uncertainty of  $\dot{n}, P_i$ , and a bias contribution to the uncertainty of  $\dot{n}, B_i$ . The two contributions were evaluated separately in terms of the sensitivity of coefficients following the Kline and McClintock [110] equation for error propagation. Table 3.3 contains a tabulation of precision and bias limits for variables and parameters used in uncertainty calculations.

The enthalpy and entropy changes for each component are calculated from the integration of the heat capacity curve. The parameters of the  $C_p$  curve are obtained from NIST [60] for the most common species. The equations apply to species where no phase transition occurs:

$$\Delta_{25}^T H^\theta = \int_{25}^T C_p dT \quad (3.5)$$

$$\Delta_{25}^T S^\theta = \int_{25}^T \frac{C_p dT}{T} \quad (3.6)$$

The Gibbs free energy of formation of products and reactants was calculated from their enthalpy and entropy of formation:

$$\Delta_f^T G^\theta = \Delta_f^T H^\theta - T \cdot \Delta_f^T S^\theta \quad (3.7)$$

where  $\Delta_f^T H^\theta$  and  $\Delta_f^T S^\theta$  are the standard enthalpy and entropy of formation, respectively.

The accuracy of thermodynamic data in the theoretical modeling as well as the interpretation of experimental results may impact the conclusions of the study. Parry [111] presented calorimetric measurements of heat capacity for copper oxychloride in the range of 20 to 410 °C, assumed a monotonically increasing function beyond that temperature and used a Debye and Einstein extrapolation method to obtain thermodynamic data to 550 °C. Although the heat capacity changes rapidly in the low-temperature range and uncertainty arose in this region, the slope of the curve decreases in the high temperature range beyond 400 °C to less than 5 J/mol.K per 100 °C.

Table 3.4: Enthalpy of formation of compounds in the Cu-Cl Cycle at 298.15 K

Compound	Enthalpy of Formation (kJ/mol)*					Standard Deviation
CuCl <sub>2</sub>	-217.4	-217.4	-218.0	-205.9	-205.9	5.83%
CuO	-162.0	-155.8	-156.1	-156.1	-156.1	0.13%
CuCl	-137.0	-137.0	-136.8	-137.0	-138.1	0.57%
CuOCuCl <sub>2</sub>	-381.3	-381.0	-385.1		-381.3**	1.54%
HCl		-92.31		-93.4	-93.3	0.48%
H <sub>2</sub> O		-241.82		-285.8	-285.8	1.88%
<b>Reference</b>	[108]	[49]	[50]	[52]	Present study***	
* Standard temperature of 298.15 K ** T. Parry [111] *** NIST [60]						

Deviations from previously observed data were attributed to undetected heat leaks. The error of values obtained through this method was +/- 1.1%. Other sources of enthalpy data of common compounds in this and past research are tabulated in Table 3.4 and the standard deviations are shown.

The specific heat for other species was obtained from regressions at the phase change temperature based on data from NIST [60]. Table 3.5 provides further details of data used in the calculations, including thermal conductivity of CuCl from measurements performed by Slack and Anderson [112].

Table 3.5: Thermo-physical properties of species

Characteristic	Value			Units
	<b>CuCl</b>	<b>CuO*</b> <b>CuCl<sub>2</sub></b>	<b>Oxygen</b>	
Specific heat capacity	66.944	74.9 to 115	33.6	<i>J/mol.K</i>
Dynamic viscosity	17 to 26		0.397*	<i>kg/m.s</i>
Molecular weight	0.09899	0.214	0.032	<i>kg/mol</i>
Molar density	42287	22678	16.19, 15.18**	<i>mol/m<sup>3</sup></i>
Thermal conductivity	0.421	0.451***	0.03	<i>J/m.s.K</i>
Heat of fusion	1.02E-4			<i>J/mol.s.K</i>
Thermal diffusivity	3.34E-7		5.515	<i>m<sup>2</sup>/s</i>
*Average; **At 750 K and 803 K ***Averaged from CuO and CuCl <sub>2</sub>				

The uncertainty of the measurement of weight loss was determined by following a combination of a precision (random) contribution to the uncertainty of  $\dot{m}$ ,  $P_{\dot{m}}$ , and a bias contribution to the uncertainty of  $\dot{m}$ ,  $B_{\dot{m}}$ . The two contributions can be evaluated separately in terms of the sensitivity of coefficients based on the Kline and McClintock equation for error propagation [110]:

$$P_{\dot{m}}^2 = \left( \frac{\partial \dot{m}}{\partial p} \right) P_p^2 + \left( \frac{\partial \dot{m}}{\partial T} \right) P_T^2 + \left( \frac{\partial \dot{m}}{\partial A_{O_2}} \right) P_{A_{O_2}}^2 + \left( \frac{\partial \dot{m}}{\partial F_{N_2}} \right) P_{F_{N_2}}^2 \quad (3.8)$$

and

$$B_{\dot{m}}^2 = \left( \frac{\partial \dot{m}}{\partial p} \right)^2 B_p^2 + \left( \frac{\partial \dot{m}}{\partial T} \right)^2 B_T^2 + \left( \frac{\partial \dot{m}}{\partial A_{O_2}} \right)^2 B_{A_{O_2}}^2 + \left( \frac{\partial \dot{m}}{\partial F_{N_2}} \right)^2 B_{F_{N_2}}^2 \quad (3.9)$$

The overall uncertainty in the determination of the total oxygen evolution is expressed by:

$$U = \left( P_{\dot{m}}^2 + B_{\dot{m}}^2 \right)^{1/2} \quad (\text{at } 95\%) \quad (3.10)$$

As discussed by Moffat [109], about 99% coverage can be formed by addition:

$$U_{add} = B_x + P_x \quad (\text{at } 99\%) \quad (3.11)$$

where the subscripts  $p$ ,  $T$ ,  $A_{O_2}$ ,  $F_{N_2}$  of precision ( $P$ ) and bias ( $B$ ) represent pressure, temperature, percent analyzer reading and flow meter, respectively; and  $U$  represents the overall uncertainty. Uncertainty estimates were taken over a representative period of the experiments. Experiments were repeated under similar conditions of initial mass and molar ratios, initial weight, reactor pressure and purge gas flow. A steady set of data was selected over a period for the uncertainty calculations. The measured uncertainty of moles of percent volume oxygen reading was determined as 1.87%, based on precision (random) contributions to the uncertainty of  $\dot{m}$ ,  $P_m$  and a bias contribution to the uncertainty of  $\dot{m}$ ,  $B_m$ . The fit of XRD data compared to data from the International Centre for Diffraction Data and inaccuracies introduced by the Rietveld method yield a weighted R-factor of approximately 3% in the phase determination.

The composition of the reaction product is analyzed by an X-ray diffraction (XRD) technique after solidification of CuCl. Bragg's Law of XRD diffraction is represented as follows:

$$n\lambda = 2d \sin(\theta) \quad (3.12)$$

The equation describes how the cleavage face of crystals scatters X-ray beams at certain angles of incidence. When the angle of incidence  $\theta$  equals the angle of scattering, and the path-length difference equals an integer number of wavelengths  $n$ , then peaks of scattered intensity can be observed as described in “Introduction to X-ray Diffraction” [113] and discussed by XRD quantification by Leroux et al. [114]. In the equation,  $d$  represents the distance between atomic layers in the crystal. Lambda,  $\lambda$ , is the known wavelength of incidence of the X-ray beams and  $n$  is an integer.

Bragg's Law conditions occur at a different  $d$ -spacing in materials with a polycrystalline structure. A pattern can then be obtained by plotting the angular positions and intensities of the resultant diffracted peaks of radiation. The diffracted peaks are a characteristic that depend exclusively on the crystalline structure of the sample. If the sample contains a mixture of different phases, the pattern shows the reflections of individual phase characteristics at different angular positions. Powder diffraction XRD was applied to a 1 mm thick sample in a 2 cm<sup>2</sup> bed in order to characterize the crystallographic structure. The measurements used a Philips PW 1830HT generator with a PW1050 goniometer, PW3710 control, X-pert software (2007 version; International Centre for Diffraction Data) and Rietveld refinement software. The Rietveld refinement method optimizes the model function to minimize the weighted sum of squared

differences between the observed and computed intensity values. In the XRD analysis of the CuCl samples, the angle  $2\theta$  was allowed to vary within a range of 5 to 60 degrees.

The uncertainty from data collection and instrumentation is a function of the measurement of temperature and conversion dependent variables as follows:

$$w_r = f\{T\}f\{x\} = f(T_s, T_g)f(N_2, O_2, Cl_2, m_s) \quad (3.13)$$

In deriving the rate of reaction equation, the Avrami-Erofeev linear fitting was used for the concentration vs. time curve, and a zero crossing approximation was then adopted. The curve of concentration vs. temperature was fitted to the Arrhenius equation. The overall measurement uncertainty of the rate expression obtained from this analysis is a function of the uncertainty of all independent variables. The estimated uncertainty of the experimental vs. calculated data yields an uncertainty of +/- 0.04 mol/m<sup>2</sup>.s. There is an additional error that results from the numerical analysis in simulating the chemical decomposition of a particle. The dynamics of the system are fast and the size of particles small. Therefore, error propagation from numerical iterations has a significant impact on results. The Runge–Kutta–Fehlberg method uses a Runge-Kutta-4 method together with a higher order method that predicts the adaptive step-size. In order to monitor and control local error the procedure of Vettering and Teukolsky [115] was used and it selected a desired accuracy  $\Delta_0$  of  $O-6$  (overall tolerance level). The error is estimated as:

$$\Delta_1 = z_{n+1} - z'_{n+1} = \sum_{i=1}^6 (c_i - c_i^*)k_i \quad (3.14)$$

where  $z$  represents the variable calculated with RK-4 and  $z'$  the same variable calculated with the RKF method. The values of  $k$  and  $c$  are the RK-4 delta midpoint and the improved Cash and Karp [116] constants, respectively. The average error of local calculations in the desired accuracy is indicated in Table 3.1. The step size is adjusted accordingly based on the desired accuracy and the new scale  $\Delta_1$  by following the correlation of Cash and Karp [116]:

$$h_o = h_1 \left| \frac{\Delta_o}{\Delta_1} \right|^{0.2} \quad (3.15)$$

In the next chapter, a predictive model of transport phenomena will be presented.

## Chapter 4 - Model of the Decomposition Kinetics

---

The thermal decomposition of copper oxychloride is a complex phenomenon that results in a three-phase system of heat and mass transfer, its understanding requires an analysis from several fronts. First, a detailed analysis of the hydrolysis reaction in view of the past literature provides the basic understanding of the nature of products that feed the decomposition reactor. Because of the closed nature of the cycle, the decomposition reactor is fed with products of reactions from the hydrolysis reactor that may carry unreacted  $\text{CuCl}_2$  and other species. Thus, a mixture of  $\text{CuO} \cdot \text{CuCl}_2$  was adopted for the decomposition reaction experiments since the potential presence of free  $\text{CuCl}_2$  with the products of hydrolysis is represented in the mixture. The preparation of the mixture also adds some variability to the sample to an extent comparable to the variability of products from hydrolysis. This process suggested a reproduction of the nature of the feedstock to the reactor with the potential presence of free  $\text{CuCl}_2$ . This decomposition of the mixture reflects better the non-uniform nature of the feedstock. Second, the decomposition reaction may follow either path as discussed by Levy and Goreaud [55] and Serban et al. [59].

These paths need to be considered and understood for this kinetic analysis to be complete. In their analysis, both researchers suggested the intermediate presence of a mixture of  $\text{CuO}$  and  $\text{CuCl}_2$  as a path to the release of oxygen. Furthermore, Serban et al. [59] proposed using a mix in experiments intended to understand the kinetics analysed the decomposition of  $\text{CuCl}_2$  with release of chlorine. Third, the product of decomposition at equilibrium is the result of the balance between the forward and reverse reaction, such

that aspects that promote the reverse reaction and the thermodynamic limits will also be analyzed here. Fourth, the analysis of the thermodynamic aspects of the decomposition reaction provided new light on the second law limits and implications on equilibrium conditions of varying pressure and temperature.

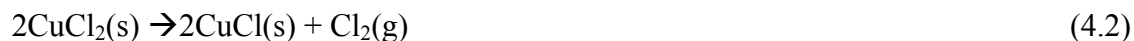
These four aspects will be analyzed such that experiments of the forward reaction can be understood with confidence before arriving at a rate of reaction expression and attempting a theoretical model of the phenomena.

#### **4.1 Hydrolysis Reaction for Production of Copper Oxychloride**

A complete hydrolysis reaction produces  $\text{Cu}_2\text{OCl}_2$  (copper oxychloride) and HCl (hydrogen chloride) as a result of the reaction of  $\text{CuCl}_2$  and steam at 380 °C. Past research indicated that the molar fraction of water must be in excess of the stoichiometric value in order to obtain reasonable conversion to copper oxychloride and hydrogen chloride. However, as the ratio of steam increases, more energy is required to heat steam and the HCl produced is more diluted.

Analysis of experimental results reported by Lewis et al. [32] and Ferrandon et al. [53] indicated that the maximum conversion to copper oxychloride is achieved at molar ratios of steam to copper in the vicinity of 20. Experiments where the steam ratio was higher than 20 increased the amount of un-reacted  $\text{CuCl}_2$  found in the solid products, in addition to CuCl. The ratio of un-reacted  $\text{CuCl}_2$  in the products decreased when the reactor operated under vacuum conditions. Dagupatti et al. [48, 52] presented a thermodynamic analysis of the reaction based on the equilibrium conversion and extent of

reaction. The study considered a mechanistic analysis of the hydrolysis of  $\text{CuCl}_2$  with three competing reactions as indicated in the following equations.



The study considered equilibrium conversion using the Gibbs free energy of reaction and the extent of reaction analysis. Increasing the initial mole fraction of steam and decreasing the total pressure of the system resulted in lower equilibrium constants and higher equilibrium conversion. Overall, the analysis indicated that the hydrolysis reaction favours high temperature, excess steam and lower than atmospheric pressures. The excess steam in the reaction also consumes the released chlorine. At a temperature of  $380^\circ\text{C}$  and atmospheric pressure, the change in Gibbs energy of the hydrolysis reaction is negative and the reaction is spontaneous. At  $380^\circ\text{C}$  and atmospheric pressure, the analysis predicted that the yield of  $\text{Cu}_2\text{OCl}_2$  is approximately 5% for stoichiometric steam ratios. The analysis also predicted a yield of 80% when pressure is decreased to 0.5 bar, and the steam ratio is increased to 5 mol/L. In a separate study, Ferrandon et al. [53] experimented with 40 mg of  $\text{CuCl}_2$  at  $350^\circ\text{C}$  and reported XRD intensity peaks of 0.6 for copper oxychloride in the products, in addition to  $\text{CuCl}$ , when using 2500 ppm of water vapour.

Ferrandon et al. [53] used a vertical spray reactor at  $400^\circ\text{C}$  with an ultrasonic nozzle to promote the contact between a solution of  $\text{CuCl}_2 \cdot \text{H}_2\text{O}$  and steam. Upon

atomization of the solution, water evaporates rapidly from the droplets. The particles of  $\text{CuCl}_2$  react with steam or thermally decompose before reaching the bottom of the spray reactor. The phase composition of products was determined by powder X-ray diffraction. A quantitative analysis was performed in the solids to determine the content of  $\text{CuCl}$ . The amount of  $\text{Cu}_2\text{OCl}_2$  was determined based on oxygen evolution from decomposition of the solid products in a catalytic reactor. At atmospheric pressure and a molar ratio of steam to  $\text{CuCl}_2$  of 10, the reaction yielded 60%  $\text{Cu}_2\text{OCl}_2$  and 7%  $\text{CuCl}$ . Reducing the reactor pressure to 0.4 bar resulted in a yield of 75%  $\text{Cu}_2\text{OCl}_2$  and 4%  $\text{CuCl}$ , with the balance of un-reacted  $\text{CuCl}_2$ .

Past literature indicated that the reaction in Eq. (3.2) does not proceed to completion, and that certain amounts of chlorine will result from the decomposition of  $\text{CuCl}_2$ . Some chlorine recombines with steam to produce hydrogen chloride as in Eq. (3.4). Since the two species are gaseous, the probability of collisions occurring and resulting in strong bonds that generate a new compound is low, resulting in free chlorine mixed with products. Free chlorine in the gas products does not represent a problem for the subsequent decomposition of copper oxychloride in the oxygen reactor, but it is a polluting agent that must be separated from the oxygen stream. Free chlorine mixed with hydrogen chloride may be a problem for the electrolytic reaction, shortening the life of the membrane and electrodes, or resulting in side reactions. This aspect requires further research. The presence of  $\text{CuCl}$  in the products of hydrolysis is acceptable since it is also a product of the decomposition of copper oxychloride in the oxygen reactor. Finally, depending on the molar fraction of steam and factors related to the geometry and efficiency of the reactor, the presence of un-reacted  $\text{CuCl}_2$  in the products of hydrolysis is

highly probable. Free  $\text{CuCl}_2$  in the oxygen reactor results in the release of chlorine, changes the balance of partial pressures in the reactor, and reduces the oxygen yield and purity.

#### 4.2 Thermodynamic Analysis of the Reverse Reaction

Copper oxychloride is not commercially available and it exists in nature in very few locations as a mineral called melanothallite. Lewis et al. [56] reported micro-scale attempts to reproduce the hydrolysis reaction with limited results. Dr. Greg Hope at Griffith University, Australia (as cited by Parry [111]) prepared copper oxychloride in a laboratory through a slow synthesis process that utilized an equi-molar mixture of copper oxide ( $\text{CuO}$ ) and cupric chloride ( $\text{CuCl}_2$  or copper II chloride) in a quartz tube vacuum heated for several days at  $400\text{ }^\circ\text{C}$ . Krivovichec and Filatov [117] synthesized melanothallite in a small reactor at temperatures between  $370$  and  $470\text{ }^\circ\text{C}$ . The temperature ranges and duration of these experiments suggests that the reaction of  $\text{CuCl}_2$  and  $\text{CuO}$  may not occur for practical reasons within the short time of duration and temperature ranges of the experiments of this research. Furthermore, the experimental work reported in past literature indicated that the most probable result of decomposition of  $\text{CuO}\cdot\text{CuCl}_2$  and of copper oxychloride are molten  $\text{CuCl}$ , oxygen gas and to a minor degree, chlorine gas. With the predominant presence of free oxygen and molten  $\text{CuCl}$ , the probability of a reverse reaction that involves these two species is higher than a reverse reaction involving  $\text{CuO}$  and  $\text{CuCl}_2$ . Based on the above discussion, this study proceeded to analyze the path for a probable reverse reaction in the decomposition of copper oxychloride as follows:



The spontaneity of the reaction in Eq. (4.4) can be predicted from the change of the Gibbs free energy of the reaction,  $\Delta_r^T G$ . Any deviation from standard conditions can influence the behaviour of the reaction. The reaction Gibbs free energy  $\Delta_r^T G$  can be calculated as follows:

$$\Delta_r^T G = \Delta_r^T G^\circ + RT \ln(Q_r) \quad (4.5)$$

where  $\Delta_r^T G^\circ$  is the change of Gibbs free energy of the reaction at standard pressure and temperature, and  $Q_r$  is the reaction quotient defined by the stoichiometric ratio of the product and reactant fugacity. Since CuCl and Cu<sub>2</sub>OCl<sub>2</sub> exist in the form of a condensed state, the reaction quotient can be simplified by:

$$Q_r = \frac{1}{(P_{O_2} / P^\circ)^{1/2}} \quad (4.6)$$

where  $Q_r$  represents the reaction quotient,  $P^\circ$  is the standard pressure (100 kPa) and  $P_{O_2}$  is the partial pressure of O<sub>2</sub> under actual reaction conditions. When the reaction reaches equilibrium, the quotient is equal to the reaction equilibrium constant  $K$  as defined by:

$$\Delta_r^T G^\circ = -RT \ln K \quad (4.7)$$

and  $K$  is then determined by:

$$K = Q = \frac{1}{(P_{O_2} / P^\circ)^{1/2}} \quad (4.8)$$

where  $\Delta_r^T G^\circ$  can be calculated from the molar Gibbs free energy of formation of the product and reactants:

$$\Delta_r^T G^\circ = \Delta_f^T G^\circ_{(\text{Cu}_2\text{OCl}_2)} - [2\Delta_f^T G^\circ_{(\text{CuCl})} + 1/2\Delta_f^T G^\circ_{(\text{O}_2)}] \quad (4.9)$$

where  $\Delta_f^T G^\circ_{(\text{Cu}_2\text{OCl}_2)}$  and  $\Delta_f^T G^\circ_{(\text{CuCl})}$  are the molar Gibbs free energy of formation for CuCl and Cu<sub>2</sub>OCl<sub>2</sub>, respectively. The Gibbs free energy of formation of each reactant and product can be calculated from their enthalpy and entropy of formation:

$$\Delta_f^T G^\circ = \Delta_f^T H^\circ - T \cdot \Delta_f^T S^\circ \quad (4.10)$$

where  $\Delta_f^T H^\circ$  and  $\Delta_f^T S^\circ$  are the standard enthalpy and entropy of formation of the species at temperature  $T$ .

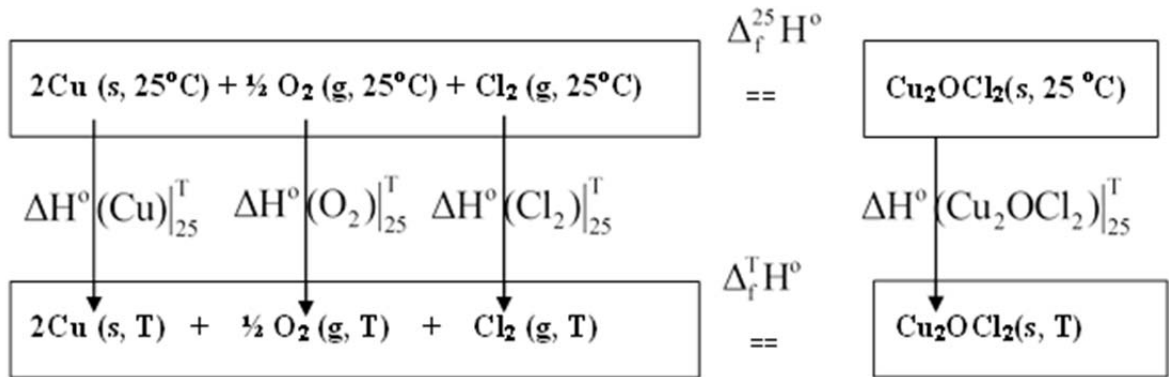


Fig. 4.1: Paths for thermodynamic calculations of copper oxychloride

Limited data of  $\Delta_f^T H^\circ$  and  $\Delta_f^T S^\circ$  have been reported for CuCl and Cu<sub>2</sub>OCl<sub>2</sub> in the temperature range of 400 to 550 °C. CuCl exists in the solid phase up to the temperature of 412 °C. At this temperature, it remains solid with a different microstructure and

thermo-physical properties. This phase is identifiable between the temperatures of 412 to 423 °C. Beyond this temperature, CuCl remains liquid in the range of temperatures of interest with significant vaporization beyond the temperature of 550 °C. The thermo-physical properties of Cu<sub>2</sub>OCl<sub>2</sub> are calculated from the properties of compounds and elements. The procedure utilizes known data of enthalpy and entropy at ambient temperature. For the product Cu<sub>2</sub>OCl<sub>2</sub> in Eq. (4.17), the schematic of a thermodynamic method in Fig. 4.1 is used for the calculation of  $\Delta_f^T H^o$  :

The method also applies to the calculation of  $\Delta_f^T S^o$  , then

$$\Delta_f^T H^o = [\Delta_f^{25} H^o + \Delta H^o(Cu_2OCl_2)_{25}^T] - [\Delta H^o(Cu)_{25}^T + \Delta H^o(O_2)_{25}^T + \Delta H^o(Cl_2)_{25}^T] \quad (4.11)$$

$$\Delta_f^T S^o = [\Delta_f^{25} S^o + \Delta S^o(Cu_2OCl_2)_{25}^T] - [\Delta S^o(Cu)_{25}^T + \Delta S^o(O_2)_{25}^T + \Delta S^o(Cl_2)_{25}^T] \quad (4.12)$$

where the enthalpy and entropy changes for each component are calculated based on the following equations:

$$\Delta_{25}^T H^o = \int_{25}^T C_p dT \quad (4.13)$$

$$\Delta_{25}^T S^o = \int_{25}^T \frac{C_p dT}{T} \quad (4.14)$$

A similar methodology is adopted for the reactants CuCl and O<sub>2</sub> in Eq. (4.4) for the calculation of  $\Delta_f^T H^o$  and  $\Delta_f^T S^o$  shown in Fig 4.2. The correlations of C<sub>p</sub> and the values of  $\Delta_f^{25} H^o$  for Cu, O<sub>2</sub>, Cl<sub>2</sub> and CuCl reported by NIST [60] are adopted in this thesis. The reactant CuCl experiences a phase change from solid to liquid at the temperature of 430

°C (803.15 K). The entropy change  $\Delta S$  at the melting point is calculated with the following equation:

$$\Delta_{melting} S^o = \frac{\Delta H_{melting}^o}{803.15} \quad (4.15)$$

where  $\Delta H$  represents the enthalpy of phase change. For  $\text{Cu}_2\text{OCl}_2$ , only the experimental data of specific heat capacity at constant pressure  $C_P$  in the temperature range of 25 - 410 °C was reported by Parry [111]. The following equation is proposed to correlate the data:

$$C_{P(\text{Cu}_2\text{OCl}_2)} = 99.23243 + 0.021622T \quad (4.16)$$

where  $C_P$  and  $T$  have units of J/mol·K and K, respectively. The relative standard deviation of Eq. (4.16) in the temperature range of 25 - 410 °C is within 3%, so it will be assumed to be extended to the temperature of 550 °C. This theoretical projection in the range of decomposition of copper oxychloride introduces additional uncertainty to the thermodynamic calculations. This is due to the unknown degree of stability of copper oxychloride beyond the temperature reported in past studies.

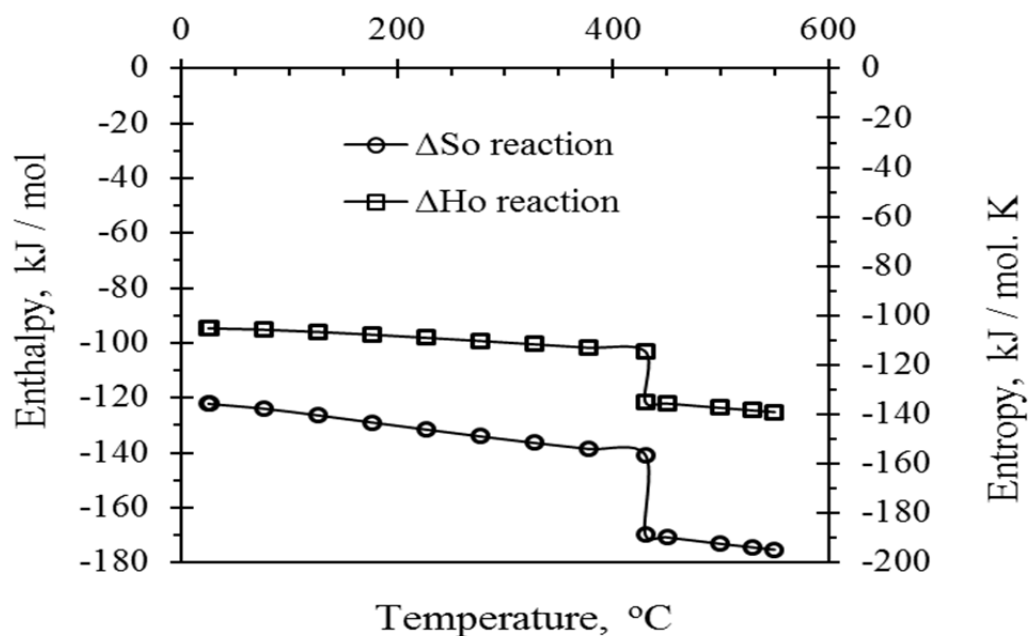


Fig. 4.2: Standard enthalpy ( $\Delta_r^T H^\theta$ ) and entropy ( $\Delta_r^T S^\theta$ ) of the reverse reaction at various temperatures

The thermodynamic properties for the formation of  $\text{Cu}_2\text{OCl}_2$  and  $\text{CuCl}$ , i.e., values of  $\Delta_f^T H^\theta$ ,  $\Delta_f^T S^\theta$  and  $\Delta_f^T G^\theta$ , are calculated from Eqs. (4.13), (4.14) and (4.10), and following the thermodynamic method described above (shown in Fig. 4.1).

Based on these thermodynamic properties, the changes of standard enthalpy  $\Delta_r^T H^\theta$ , entropy  $\Delta_r^T S^\theta$ , and Gibbs free energy  $\Delta_r^T G^\theta$  for the reaction in Eq. (4.4) can be calculated, as shown in Figs. 4.3 and 4.4.

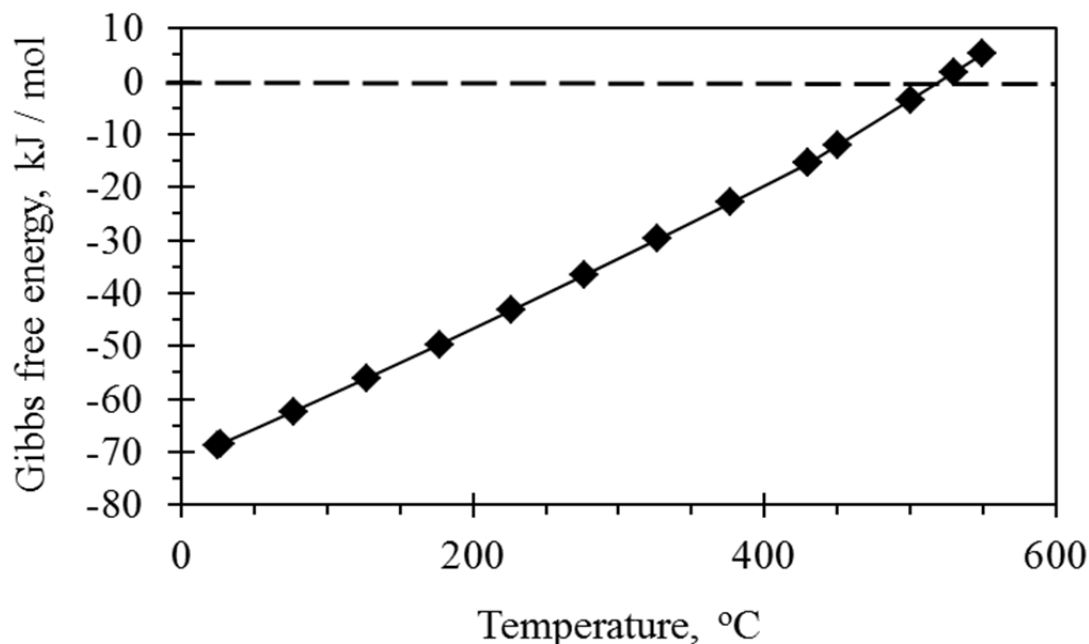


Fig. 4.3: Standard Gibbs free energy ( $\Delta_r^T G^\circ$ ) of the reverse reaction at various temperatures

The negative values of the reaction enthalpy in the temperature range of reactions as shown in Fig. 4.2 indicate that the reverse reaction is exothermic. The steep slope at 430 °C is explained by the phase change of CuCl at this temperature, which also explains the steep slope for the standard entropy of reaction. This sudden change does not exist in Fig. 4.3 for the standard Gibbs free energy  $\Delta_r^T G^\circ$  because the phase change of CuCl is close to a reversible thermodynamic process under isobaric conditions.

As indicated in Fig. 4.3, the transitional point from negative to positive Gibbs free energy  $\Delta_r^T G^\circ$  occurs at a temperature close to 510 °C, which indicates that the reverse reaction is spontaneous if the temperature is below it at standard pressure, or the reaction will not occur when the temperature is higher than 510 °C at standard pressure.

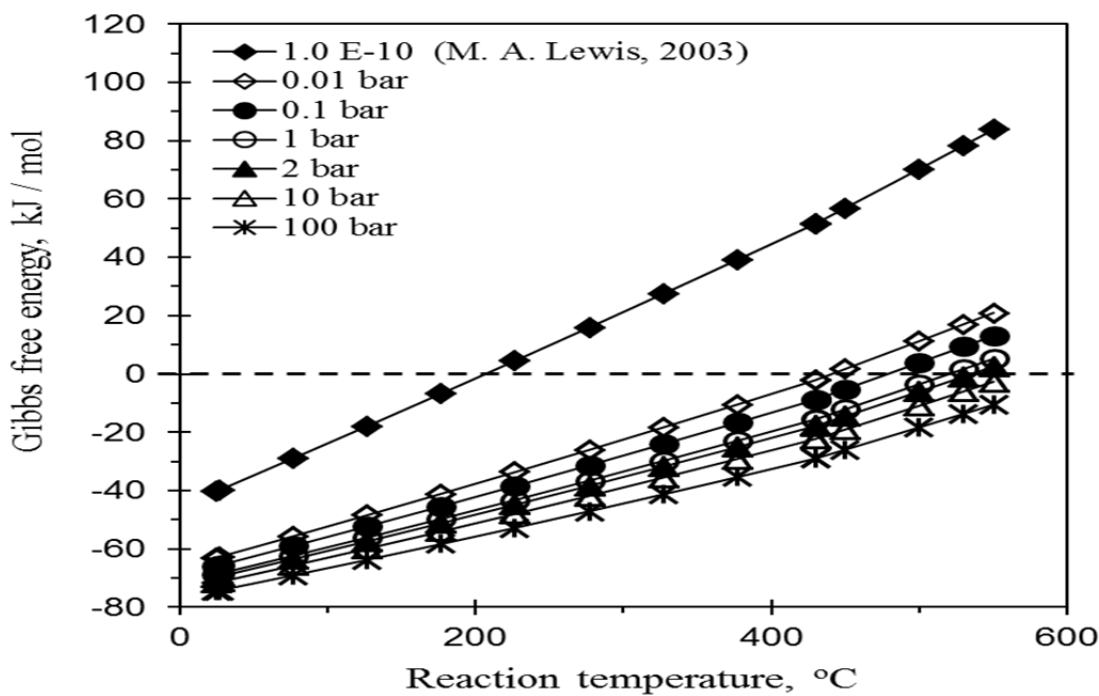


Fig. 4.4: Gibbs free energy of CuCl + O<sub>2</sub> reaction at various operating conditions

Figure 4.4 shows results for the operating pressure range of  $1.0 \times 10^{-10}$  to 100 bars to represent the range of vacuum to highly pressurized reactors. An analysis of Fig. 4.4 indicates that the reverse reaction may be minimized by either decreasing the oxygen pressure or increasing the reaction temperature. When the oxygen pressure is decreased to below one bar, a vacuum will be created. Since the produced oxygen in the forward reaction is often pressurized for further storage or utilization in other units that consume oxygen, a vacuum oxygen reactor may increase the power consumption of the vacuum and pressurization for industrial scale oxygen production. In addition, a vacuum is more likely than pressurization to introduce other gases into the oxygen production reactor. Furthermore, negative pressure may also increase the generation of CuCl vapour. Therefore, a vacuum oxygen production reactor is not suggested for the Cu-Cl cycle.

A method of minimizing the reverse reaction is to increase the operating temperature. However, if the temperature is higher than 530 °C, significant amounts of CuCl vapour may be generated, as observed in the reactor and oxygen outlet in the experiments.

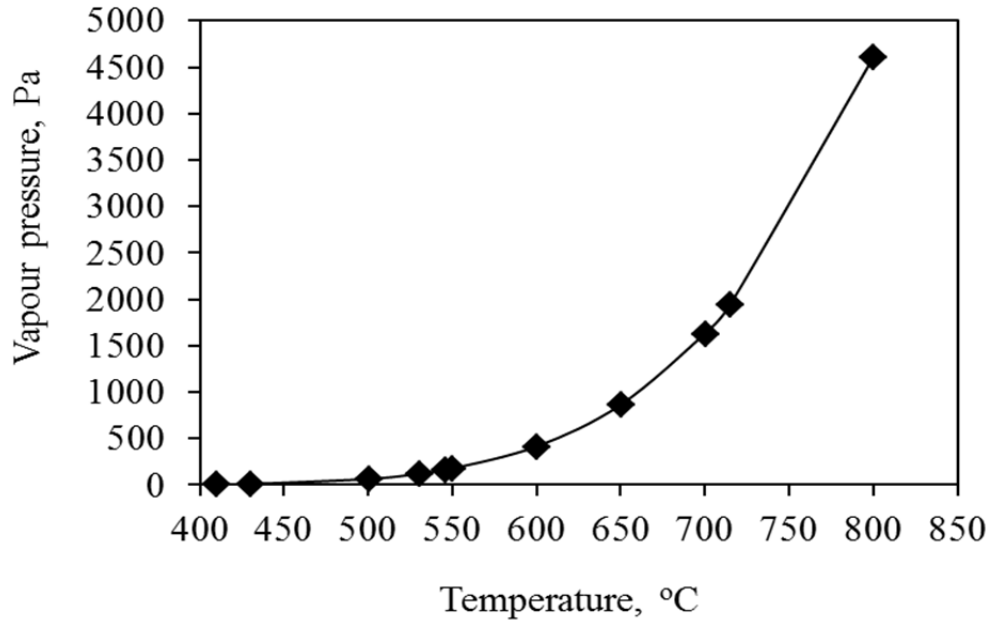


Fig. 4.5: Vapour pressure of CuCl at various temperatures

Figure 4.5 shows the vapour pressure of CuCl based on experimental data reported in previous studies by Brewer and Lofgren [118] and Mizuno et al. [119]. The temperature must be below 530 °C in order to maintain the vapour pressure of CuCl below 1,000 Pa (0.01 bar). For CuCl vapour minimization and the simultaneous impact of pressure and temperature on the Gibbs free energy, the optimum operating pressure is suggested in the range of 1 - 2 bars and a temperature in the range of 525 - 550 °C.

Although it is desirable to decompose  $\text{Cu}_2\text{OCl}_2$  at lower temperatures, experimental results of the decomposition of copper oxychloride indicate that the conversion rate is very low below  $500\text{ }^\circ\text{C}$ . This is due to the increased spontaneity of the reverse reaction at lower temperatures. As shown in Fig. 4.3, the Gibbs free energy of the reverse reaction is positive at temperatures above  $510\text{ }^\circ\text{C}$ .

Furthermore, Fig. 4.3 indicates that the reverse reaction is spontaneous ( $\Delta G < 0$ ) when the operating temperature is below  $450\text{ }^\circ\text{C}$ , and the oxygen pressure is higher than 0.01 bars. This implies the reverse reaction may occur in the process of reactant preheating from a temperature significantly lower than  $450\text{ }^\circ\text{C}$ . This situation may occur when species are transferred from the hydrolysis reaction to the downstream oxygen production reaction as shown in Fig. 4.3.

Lower pressure in the reaction system moves the curve to the left, thus lowering the temperature for equilibrium. Furthermore, the decomposition reaction occurs with removal of oxygen from the reacting zone. Thus even if the conditions for the reverse reaction are present, the produced  $\text{CuCl}$  is starved for oxygen to react. This effect is confirmed by Le'Chatelier's principle, thus promoting the forward reaction.

### **4.3 Copper Oxychloride Decomposition Reaction**

It can be prepared in small quantities in the laboratory through a lengthy process that used an equi-molar mixture of copper oxide ( $\text{CuO}$ ) and copper II chloride ( $\text{CuCl}_2$ ). The decomposition experiments with a mixture have been justified in the past literature on the basis that the intermediate reactions occur through the decomposition of  $\text{CuCl}_2$  and the reaction of  $\text{CuO}$  in competing dynamics. Also, the absence of easy access to the

compound has motivated the experiments of decomposition reported in the literature are a result of either copper-oxychloride ( $\text{Cu}_2\text{OCl}_2$ ) or from a mix of  $\text{CuO}$  and  $\text{CuCl}_2$  identified as  $\text{CuO}\cdot\text{CuCl}_2$ . Since the decomposition of the mix represents a more stringent situation, it was decided that the experimental work would be conducted on a stoichiometric mixture of  $\text{CuO}$  and  $\text{CuCl}_2$ .

Two potential paths for the decomposition of copper oxychloride have been discussed in the literature. The treatment of the decomposition reaction suggested an intermediate step where the compound is treated as a mixture of  $\text{CuO}$  and  $\text{CuCl}_2$  rather than copper oxychloride. A mechanistic approach to copper oxychloride decomposition was first proposed by Walter-Levy et al. [55]. The experiments indicated that copper oxychloride is stable until the temperature of  $370^\circ\text{C}$  is reached. Between  $375^\circ\text{C}$  and  $470^\circ\text{C}$ ,  $\text{Cl}_2$  is released with the formation of  $\text{CuCl}$  and  $\text{CuO}$  plus small amounts of  $\text{CuCl}_2$ . From  $475^\circ\text{C}$  to  $550^\circ\text{C}$ , XRD reveals larger amounts of  $\text{CuCl}_2$  in the products while the amount of  $\text{CuO}$  was reduced. The decomposition reaction is analyzed in view of two consecutive reactions as follows:



The competing reaction occurs in parallel, and the experimental results indicated that the secondary reaction was responsible for a partial decrease of  $\text{CuO}$  due to  $\text{Cl}_2$  from the former reaction. In the analysis this set of reactions is called path A.

Another approach to the analysis of the decomposition of copper oxychloride was recently proposed by Serban et al. [59]. The experiments used an equi-molar mixture of CuO and CuCl<sub>2</sub> in a vertical reactor at 500 °C. The XRD analysis of the solid products indicated that the solid phase is pure CuCl. The analysis used a mechanistic approach (path B) and concluded that the oxygen evolution is limited by the decomposition of CuCl<sub>2</sub>. The reaction occurred in two consecutive stages as follows:



The competing reaction in Eq. (4.19) is the heterogeneous, endothermic thermolysis of cupric (II) chloride. The observations indicated that even though only 60% decomposition of CuCl<sub>2</sub> is achieved at 530 °C, the presence of CuO in the mixture appeared to promote the release of Cl<sub>2</sub>. This effect was also observed by Serban et al. [59] and resulted in decomposition of CuCl<sub>2</sub> at lower temperatures. The study also concluded that the Cl<sub>2</sub> released is completely consumed in the reaction with CuO as in Eq. (4.20) since no free Cl<sub>2</sub> was detected in the gas products.

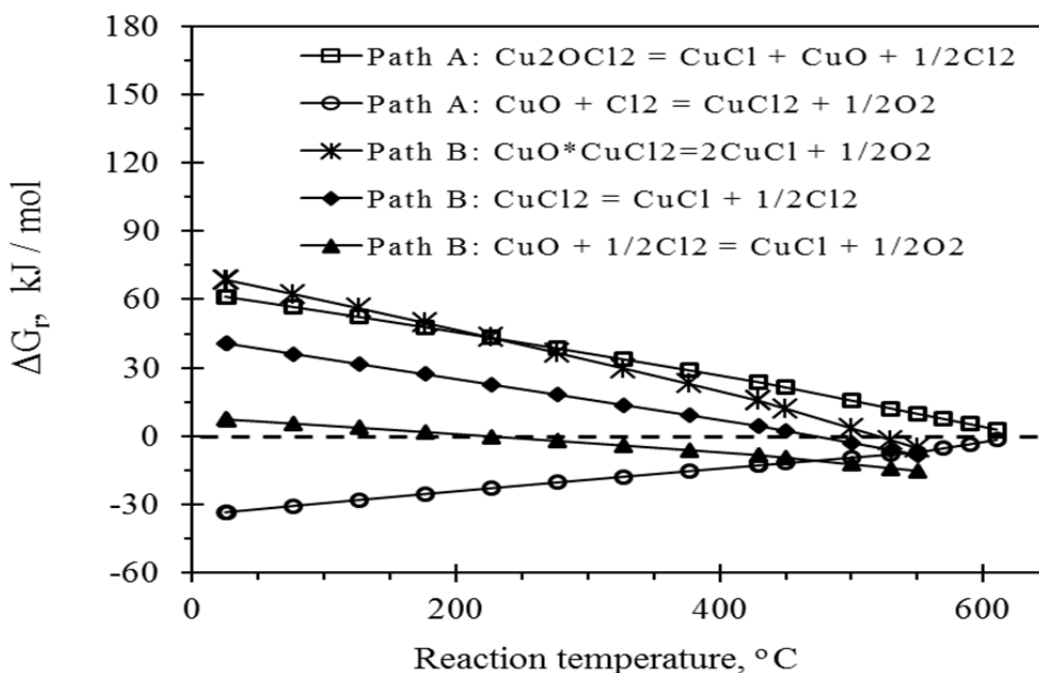


Fig. 4.6: Gibbs energy of reactions of two pathways (path A in open markers) for decomposition of copper oxychloride at atmospheric pressure

The Gibbs energy of reaction provides an indication of the probability of either mechanistic approach to occur. Figure 4.6 indicates the temperatures at which each of the possible reactions becomes spontaneous. The Gibbs free energy of the reaction in Eq. (4.19) indicates that the reaction reaches equilibrium at 500 °C, and it is spontaneous beyond this temperature, with more chlorine available to react with CuO as the temperature increases. Furthermore, experimental results also indicated that the decomposition of  $\text{CuCl}_2$  is not completed until it reaches 600 °C.

The two mechanistic approaches coincide in the intermediate release of chlorine and displacement of oxygen out of copper oxide to produce either copper (I) chloride or copper (II) chloride. Experiments conducted by Marin et al. [44, 62] indicated that the

decomposition of  $\text{CuO}\cdot\text{CuCl}_2$  results in a mixture of oxygen, chlorine and  $\text{CuCl}$  vapour. The occurrence of  $\text{CuCl}$  vapour is anticipated because the melting point of  $\text{CuCl}$  is  $430^\circ\text{C}$ , below the temperature of the experiments.

$\text{CuCl}$  vapours condense as soon as gases exit the reactor, given the high differential between the phase change temperatures and ambient such that the overall impact of  $\text{CuCl}$  vapours in the evolution rate of gases is not obvious. The partial pressure of chlorine is several orders of magnitude larger than  $\text{CuCl}$  vapour which rises rapidly beyond  $430^\circ\text{C}$ . It results in the potential presence of  $\text{CuCl}$  vapour in the oxygen stream. The thermodynamic analysis of the decomposition of  $\text{CuCl}_2$  indicated that at a temperature of  $470^\circ\text{C}$ , the Gibbs energy of the decomposition of  $\text{CuCl}_2$  becomes negative and therefore the reaction becomes spontaneous. The Gibbs energy of reaction of copper oxide and chlorine is also negative in this range of temperature, therefore, in the presence of copper oxide, free chlorine can react to produce  $\text{CuCl}$  or  $\text{CuCl}_2$  as indicated by the curves in Fig. 4.6, to release oxygen. Furthermore, when  $\text{CuCl}_2$  is entrained with copper oxychloride in the products of hydrolysis, it continues to decompose spontaneously beyond  $470^\circ\text{C}$  and beyond what can possibly react with  $\text{CuO}$ .

To study the effect of the operating pressure on the chemical streams among integrated reactions, the Gibbs energy of the competing reactions is used at low and standard pressures in Fig. 4.7. At 0.1 bar, the decomposition of  $\text{CuCl}_2$  reaches equilibrium at  $350^\circ\text{C}$  and becomes spontaneous above that temperature. By comparison, the decomposition of  $\text{Cu}_2\text{OCl}_2$  at the same temperature and pressure is not spontaneous. Copper oxychloride is stable up to the temperature of  $470^\circ\text{C}$ .

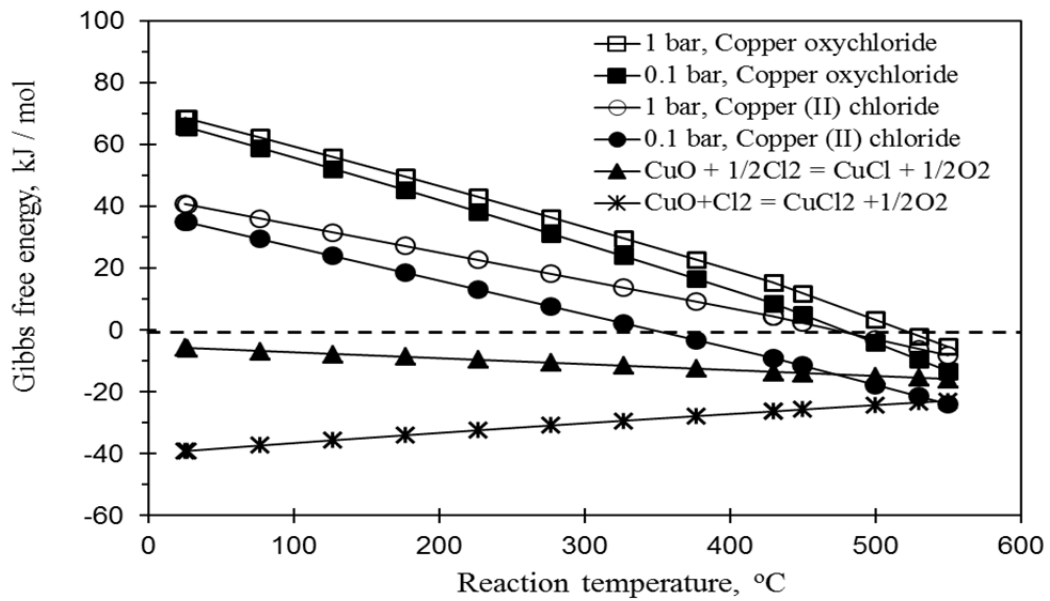


Fig. 4.7: Effects of reactor pressure in the Gibbs energy of the copper oxychloride decomposition reaction

Between 375 °C and 470 °C, it decomposes with the formation of CuCl, CuCl<sub>2</sub> and chlorine as discussed by Marin et al. [44]. The Gibbs free energy of reaction in Fig. 4.7 indicates that the second reaction occurs as soon as chlorine is available in the system. Also, the slope of the Gibbs curve indicates that more CuCl<sub>2</sub> decomposes at low pressure and within the same temperature range compared to atmospheric pressure. Operating at pressures under atmospheric pressure does not change the mechanics of reactions. The advantages of operating the reactor at lower pressures can also be seen from Fig 4.7 where the difference of slopes between the curves at 1 bar and 0.1 bar indicated that the advantages of lowering the temperature threshold of the oxygen production reactor may be compromised with the additional mechanical energy requirement. This alternative has considerable impact on the overall efficiency on the cycle and the final cost of hydrogen.

### 4.3.1 Thermodynamic Equilibrium of the Decomposition Reaction

The equilibrium of phases in any mixture of species is the result of thermal, mechanical and chemical potential equilibrium. As the species in the mixture are influenced by chemical reactions, the condition of chemical reaction equilibrium needs to be considered in addition to those mentioned above. At the point of chemical equilibrium, the forward and backward reaction rates balance so there is no change in the Gibbs energy of reaction as expressed by Eq. (4.4):

With the forward and backward reaction rates balanced, the expression to the left in Eq. (4.5) becomes zero, and the reaction quotient  $Q_r$  at equilibrium is called the equilibrium constant at the given temperature. Therefore, the change in Gibbs energy at a specific temperature is defined by Eq. (4.7), with  $Q_r = K_{eq}$ , where  $\Delta_r G^\circ$  is the standard Gibbs energy of reaction. It results from the sum of the standard Gibbs energy of the reaction products minus the sum of standard Gibbs energy of reactants; and standard denotes ideal behaviour. At equilibrium, the change in Gibbs free energy of the reaction equals zero, and the reaction quotient represents the equilibrium constant. A deviation from standard conditions influences the temperature at which the reaction becomes spontaneous. The deviation from the reference state (1 bar) can be described in terms of fugacity. A method similar to that applied to the reverse reaction in Eq. (4.4) is used and applied to the decomposition as described in Eqns. (4.17 – 4.18). In terms of the fugacity coefficient  $\phi$  and the mole fraction as discussed by Avrami [85] and represented in the following equation:

$$K(T) = \frac{y_C^{v_C} y_D^{v_D}}{y_A^{v_A} y_B^{v_B}} \left( \frac{P}{P^\circ} \right)^{-\Delta_r v} \frac{\phi_C^{v_C} \phi_D^{v_D}}{\phi_A^{v_A} \phi_B^{v_B}} \quad (4.21)$$

where A, B, C, D represent the species in the reaction. At low differential pressures, the fugacity of condensed phases becomes 1. Also, as gases approach ideal gas behaviour, the fugacity coefficient approaches a value of unity. The reactions occur at atmospheric pressure or very close to 1 bar. Therefore, assume ideal gas behaviour for this analysis. The mole fraction of gaseous species can be expressed as a function of the extent of reaction:

$$n_i = n_i^o + \sum_{j=1}^j \nu_{i,j} \xi_j \quad (4.22)$$

where  $j$  represents the number of reactions, and there is one extent of reaction for each reaction. For the copper oxychloride decomposition in Eq. (4.17), the equilibrium constant in terms of partial pressures is represented by:

$$K_1 = \left( \frac{\hat{f}_{Cl_2}}{1bar} \right)^{0.5} \left( \frac{\hat{a}_{CuCl}}{a_{CuCl}} \right)^1 \left( \frac{\hat{a}_{CuO}}{a_{CuO}} \right)^1 \left( \frac{\hat{a}_{Cu_2OCl_2}}{a_{Cu_2OCl_2}} \right)^{-1} \quad (4.23)$$

The initial number of moles of chlorine is zero, therefore the number of moles of chlorine as determined from Eq. (4.17) is  $n_{Cl_2} = \frac{1}{2} \xi$ , and the total number of moles in the gas phase at any time is calculated as  $n = n_{Cl_2} = \frac{1}{2} \xi$ . Also, the activity for condensed and solid species is typically 1. From Eq. (4.18) and with consideration for activity of condensed phases and ideal gas behaviour,

$$K_1 = \left( \frac{y_{Cl_2} P}{P^o} \right)^{0.5} \quad (4.24)$$

$$\text{Here } K_1 = P_{Cl_2}^{1/2}, \text{ (for the reaction in Eq. (4.17));} \quad (4.25)$$

Applying similar procedure to reactions in Eqns. (4.18, 4.19) and (4.20) respectively, we obtain:

$$K_2 = \frac{(0.5\xi_2 - 0.5\xi_2^2)^{1/2}}{1 - \xi_2} \frac{1}{P^{1/2}}, \text{ (for reaction in Eq. (4.18))} \quad (4.26)$$

$$K_3 = P_{Cl_2}, \text{ (for the reaction in Eq. (4.19))} \quad (4.27)$$

$$K_4 = \frac{\xi_2}{1 - \xi_2}, \text{ (for the reaction in Eq. (4.20))} \quad (4.28)$$

Numerical solutions are presented for a system with a mixture of copper oxide and copper (II) chloride. Low values of equilibrium constants indicate high rates of conversion at equilibrium. Serban et al. [59] reported equilibrium constant values between 6.013 and 7.767 at temperatures of 480 to 515°C, respectively, for the CuO and Cl<sub>2</sub> reaction in Eq. (4.20).

Table 4.1: Gibbs equilibrium constants for potential decomposition paths

Path	Reaction	Temperature °C				
		430	450	500	530	550
A	$Cu_2OCl_2 = CuCl + CuO + \frac{1}{2} Cl_2$	0.017	0.028	0.087	0.160	0.240
A	$CuO + Cl_2 = CuCl_2 + \frac{1}{2} O_2$	8.90	7.10	4.30	3.30	2.80
B	$CuCl_2 = CuCl + \frac{1}{2} Cl_2$	0.468	0.677	1.569	2.474	3.292
B	$CuO + \frac{1}{2} Cl_2 = CuCl + \frac{1}{2} O_2$	4.156	4.822	6.794	8.200	9.235

It can be inferred from Fig. 4.6 that products dominate the mixture at higher temperatures. Thus, a high value of the equilibrium constant based on the Gibbs energy of reaction

indicates that a larger proportion of the mixture at equilibrium is due to products rather than unreacted reactants (tabulated in Table 4.1).

Higher values of the equilibrium constant derived from path B suggest that this path results in higher conversion. This information is useful if the path could be selected and controlled. However, the decomposition will occur through either or both. The most efficient path will dominate. The path is then determined by several factors that need to be understood and their impact on the rate of reaction. Those factors, among others, include the concentration of solids, heat flux, hindering effects such as partial pressure of oxygen, and CuCl vapour formation which is function of the temperature of the molten salt.

#### 4.4 Experimental Rate of Reaction

In the kinetics model in the following section, the rate expression for a species “*i*” in general will be written as a product of a temperature dependent term and a composition dependent term as follows:

$$r_i = f_1(\text{composition}) * f_2(\text{temperature}) = k_1 * k_2 \quad (4.29)$$

where  $k_1$  is the concentration dependent term and  $k_2$  is the temperature dependent term. For the conversion dependent term, Wilburn and Sharp [82] used a reduced time method and applied it to three different conditions, each a function of the heat flux. In the decomposition of copper oxychloride, two different conditions were considered: one where heat transfer into the sample was high, representative of a TGA apparatus; and in the other condition, heat transfer into the sample was low, representative of an apparatus in which relatively large samples are used. Alternative, the latter case occurs if heat must

flow through a ceramic crucible (e.g. quartz) tube or where a gaseous space exists before reaching the sample, a situation typical of a batch reactor.

The Avrami-Erofeev equation (as cited by Singh et al. [83] and Avrami [85]) relates how solids transform from one phase to another during a chemical reaction. It is assumed that the decomposition occurs at the same rate in all directions of the particle, and that the decomposition rate does not depend on the extent of reaction:

$$r(X) = k_1 (-\ln(1-X))^{0.5} \quad (4.30)$$

In the reactor experiments, the partial pressure of oxygen started to increase at 430 °C, suggesting that pure CuCl<sub>2</sub> starts to decompose at or before this temperature thereby making Cl<sub>2</sub> available to displace O<sub>2</sub> out of CuO. Although CuCl<sub>2</sub> does not decompose completely before reaching 630 °C, the presence of CuO seems to favour its decomposition. The highest rates of decomposition of CuO\*CuCl<sub>2</sub> at 93% were observed at temperatures of 530 °C. Marin et al. [44] presented experimental results that supported two different pathways of decomposition of CuO\*CuCl<sub>2</sub>. A first-order reaction does not fit the decomposition. An empirical curve fitting procedure is used by following the Avrami-Erofeev equation. The regression has been approximated to a line crossing the origin, with a magnitude of error of the correlation as reported in Table 3.1.

Following the linear curve fitting of conversion vs. time using the Avrami-Erofeev equation, the rate equation in terms of the conversion of CuO\*CuCl<sub>2</sub> can be represented by the following expression:

$$n_0 \frac{\partial X}{\partial t} = k_1 (-\ln(1-X))^{0.5} \quad (4.31)$$

Using separation of variables and introducing the following transformation:

$$V = (-\ln(1-X))^{0.5} \quad (4.32)$$

$$e^{V^2} = e^{-\ln(1-X)} \quad (4.33)$$

Substituting in Eq. (4-31),

$$n_0 \frac{\partial X}{(-\ln(1-X))^{0.5}} = n_0 \frac{2Ve^{-V^2}}{V} dV = k_1 t \quad (4.34)$$

Then integration yields:

$$2n_0 \int e^{-V^2} dV = n_0 \sqrt{\pi} \operatorname{erf}(V) = k_1 t \quad (4.35)$$

Substituting from Eq. (4-32):

$$n_0 \sqrt{\pi} \operatorname{erf}\left(\sqrt{-\ln(1-X)}\right) = k_1 t \quad (4.36)$$

where  $k_1$  represents the conversion dependent term in the rate Eq. (4-29).

The temperature dependent term is obtained following the Arrhenius law. The conversion of  $\text{CuO} \cdot \text{CuCl}_2$  at several temperatures tabulated against  $1/T$  (temperature in K) resulted in a linear correlation. A pre-exponential factor is obtained from the linear regression of concentration vs. temperature. The slope of the curve provides the value of the energy of

reaction. It can be observed that the energy of reaction is positive as a result of the endothermic nature of the reaction.

The combined conversion and temperature rates result in the overall rate of reaction equation:

$$r = k_1 * k_2 = \frac{n_0 \sqrt{\pi} [k_0 e^{-E/RT}] \left[ \operatorname{erf} \left( \sqrt{-\ln(1-X)} \right) \right]}{t} \quad (4.37)$$

Serban et al. [59] analyzed the decomposition of  $\text{CuO} \cdot \text{CuCl}_2$  via TGA experiments. In the experiments, free chlorine is injected to a sample of CuO heated at 480 °C. The chlorination resulted in oxygen release and the apparent activation energy was estimated at 45 kJ/mol. Although not directly comparable, the analysis of experimental data in this research resulted in apparent activation energy of 22 kJ/mol at 530 °C. Based on the expressions for a conversion dependent term and a temperature dependent term, and introducing a thermal resistance factor by comparison with the pure phase change model, a final correlation for the rate of reaction expression is obtained as follows:

$$Rr = \frac{n_0 \sqrt{\pi} [k_0 e^{-E/RT}] \left[ \operatorname{erf} \left( \sqrt{-\ln(1-X)} \right) \right]}{t} * \frac{1}{L_c^2} \quad (4.38)$$

where the resulting rate of reaction units are given in  $\text{mol}/\text{m}^2 \cdot \text{s}$ . The initial number of moles of  $\text{CuO} \cdot \text{CuCl}_2$  is indicated by  $n_0$ . Also,  $L_c$  represents the characteristic length of the system, impacted by the shape of the crucible as discussed previously. The results suggest that the relation of instantaneous volume of sample versus some surface of the reactor

impact the rate of reaction in a manner that is inversely proportional to the magnitude of the characteristic length. As the size of the sample decays in a batch process, the net heat flow to the sample is reduced due to the reduced surface area. This effect results in decay of the rate of decomposition as indicated by the experimental data.

## Chapter 5 - Model of Moving Boundary Heat Transfer

---

In this chapter, a model is developed for heat transport across a stagnant liquid film that surrounds the particle. A moving interface is assumed at the solid-liquid interface and heat transport across the interface is the dominant rate limiting mechanism. Other transport resistances are neglected in the model. The rate is then modelled by an empirical factor that accounts for other thermal resistances. The phase change model assumes symmetry and uniform properties in a spherical region surrounding a particle. The model neglects convective effects or mass transfer resistances. The rate at which the interface moves inwards represents the rate at which the concentration of solid changes.

There exists a relation between the change phase model and the rate of chemical decomposition of a solid particle with the reaction occurring at the interface surface, where the proportionality constant is a function of the magnitude of mass transport, heat transport and chemical reaction resistances. The solution of the energy equation in a solid particle subject to a moving boundary that arises from the phase change provides an expression from which the position of the interface of solid and liquid can be tracked as the decomposition occurs. A model of coupled processes is developed to gain new understanding of the magnitude of resistances that affect the conversion rate of  $\text{CuO} \cdot \text{CuCl}_2$  in a reactor by a comparison with experimental data. The energy equation will be written separately for the solid and liquid phases, and the temperature is coupled to the dynamic interface movement through the interfacial energy balance.

The decomposition of spherical particles of  $\text{CuO} \cdot \text{CuCl}_2$  in sizes ranging from 100 microns to 200 microns will be analyzed with a particular focus on the heat transfer

processes. The resistances to heat transfer will be analyzed and a decomposition model will be developed and compared with experimental data. The resistances arise from gas diffusion from the transition surface and through the liquid phase, thereby increasing the resistance to heat conduction through molten CuCl and reducing the rate at which heat reaches the solid core. A separate analysis of the mass diffusion resistance is beyond the scope of this thesis and it is not included in the following analysis.

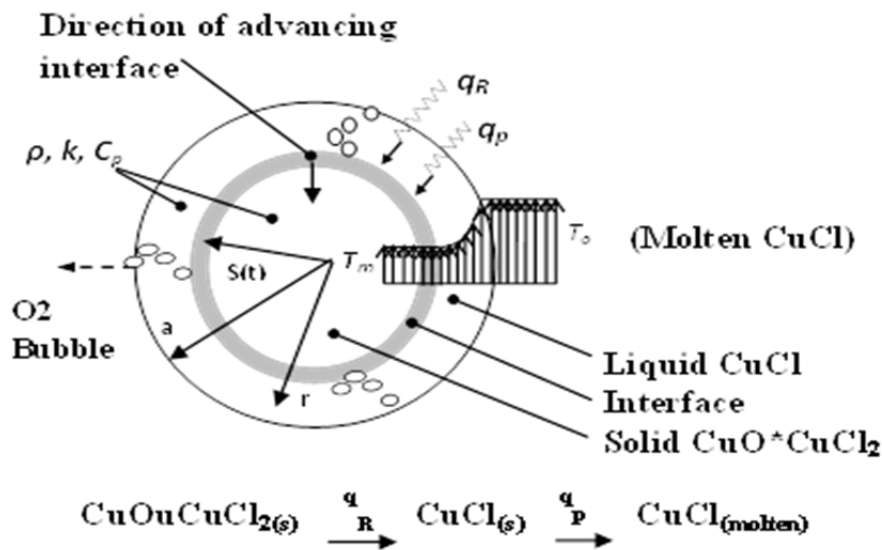


Fig. 5.1: Particle interface, species and temperature profiles during thermal decomposition

It is assumed that the latent heat for CuCl melting is absorbed at the transition of solid  $\text{CuO} \cdot \text{CuCl}_2$  and molten CuCl simultaneously with the energy required for decomposition. A sharp interface exists at this transition. Heat is initially transferred to the molten product, then to the surface of the particle and this causes the phase interface to appear. The interface moves inwards and a liquid phase occurs at the outer surface of the particle. The supplied heat must then be conducted through the liquid phase into the moving interface. The solid reactant will decompose and the molten product appears as

soon as the high temperature is experienced at the phase interface. This yields a sharp moving front at  $r = S(t)$  that separates the solid and liquid regions as indicated in Fig. 5.1.

### 5.1 Energy Equation

The energy equations are given by:

$$\rho C_{Pl} \frac{\partial T_l}{\partial t} = \lambda_l \left( \frac{1}{r^2} \frac{\partial}{\partial r} \left( r^2 \frac{\partial T_l}{\partial r} \right) \right) \quad (5.1)$$

$$\rho C_{Ps} \frac{\partial T_s}{\partial t} = \lambda_s \left( \frac{1}{r^2} \frac{\partial}{\partial r} \left( r^2 \frac{\partial T_s}{\partial r} \right) \right) \quad (5.2)$$

for the liquid and solid phases, respectively. The phase change model considers a particle wherein the solid portion does not have an internal spatial temperature gradient. The initial temperature of the solid equals the phase change temperature while the liquid phase presents a temperature profile. Following these assumptions, this analysis focuses on the solution of Eq. (5.1).

The total heat supplied to the particle must equal the heat required for chemical decomposition. In the decomposition of  $\text{CuO} \cdot \text{CuCl}_2$ , the total heat per mol supplied must provide the required heat to the endothermic reaction enthalpy,  $\Delta H_R$ , and the heat required for the  $\text{CuCl}$  phase change,  $L$ .

$$q = L + \Delta H_R \quad (5.3)$$

The reaction enthalpy is determined by the formation enthalpy of products (molten  $\text{CuCl}$  and oxygen) and reactant (mixture of  $\text{CuCl}_2$  and  $\text{CuO}$ ) in the temperature range of interest as discussed by Marin et al. [62] and indicated in the following expression:

$$\Delta H_R = \sum H_{prod} - \sum H_{reac} \quad (5.4)$$

The phase change heat consists of two sources: one is the melting of CuCl produced in the reaction, and the other is the partial evaporation of molten CuCl. Since the CuCl evaporation is partial, the CuCl phase change enthalpy caused by the partial evaporation of CuCl is determined by the evaporation latent heat and the production rate of CuCl vapour. The maximum partial pressure of the CuCl vapour corresponds to its thermodynamic equilibrium vapour pressure. Therefore, the upper thermodynamic limit of the evaporated amount is determined by both the equilibrium vapour pressure and the oxygen production rate if the oxygen bubbles are saturated with CuCl vapour immediately after oxygen is produced. The CuCl vapour production rate is determined by the O<sub>2</sub> production rate, i.e., decomposition rate of reactant, and the evaporation rate of molten CuCl. Since the coupled processes are complex in this three-phase reacting system, assumptions are adopted for purposes of modeling. The assumptions are reasonable for the actual processes in a larger scale system because the gas bubbles would experience a longer path while passing through a deeper molten CuCl bath. The oxygen production rate is determined by the reaction decomposition rate, and based on the saturation partial pressure as reported in past studies by Marin et al. [62].

In this first part of the model, the movement of the interface with time as a result of the phase change is predicted. The system is characterized by Stokes flow where heat conduction prevails over convection. Thermal radiation and other heat transfer mechanisms are lumped into a single effective heat transfer term. Therefore, at the interface, the heat balance is given by.

$$\left[ \lambda_s \frac{\partial T_s}{\partial r} - \lambda_l \frac{\partial T_l}{\partial r} \right]_{r=S(t)} = \bar{\rho} L \frac{dS(t)}{dt} \quad (5.5)$$

Since the solid portion of the particle remains at constant temperature and there is no temperature gradient, Eq. (5.5) reduces to:

$$\left[ \lambda_l \frac{\partial T_l}{\partial r} \right]_{r=S(t)} = \bar{\rho} L \frac{dS(t)}{dt} \quad (5.6)$$

where

$$\bar{\rho} = \frac{n_s \rho_s + n_l \rho_l}{n_t} \quad (5.7)$$

The average liquid-solid density is calculated with consideration of the number of moles present in each phase at equilibrium. The error inherent in this consideration is indicated in Table 3.1. Furthermore, it is assumed that there is a negligible temperature gradient in the solid. With  $T(r,t)$  assumed continuous within the range  $S(t) \leq r \leq a$ , the governing equations are then defined by Eq. (5.1) and the Dirichlet boundary and initial conditions of the problem, as well as the interfacial Stefan condition given by Eq. (5.6) and:

$$T(a,t) = T_o \quad \text{at } r = a \quad (5.8)$$

$$T(0,t) = T_m \quad \text{at } r = 0 \quad (5.9)$$

$$T(r,0) = T_m \quad (5.10)$$

## 5.2 Dimensional Analysis

Define the following non-dimensional relations, which will be used to formulate an integral solution of the Stefan problem for the spherical particles:

$$\xi = \frac{T - T_m}{T_o - T_m} \quad (5.11)$$

$$\psi = \frac{r}{a} \quad (5.12)$$

$$t^* = \frac{\lambda}{\rho C_p} \frac{t}{a^2} \quad (5.13)$$

$$R(t) = \frac{S(t)}{a} \quad (5.14)$$

Substituting these relations into the energy equation, Eq. (5.1) yields:

$$\frac{\partial \xi}{\partial t^*} = \frac{1}{\psi^2} \frac{\partial}{\partial \psi} \left( \psi^2 \frac{\partial \xi}{\partial \psi} \right) = \frac{1}{\psi} \left( \psi \frac{\partial^2 \xi}{\partial \psi^2} + 2 \frac{\partial \xi}{\partial \psi} \right) \quad (5.15)$$

with the conditions:

$$\xi(\psi, t^*) = 1 \quad \text{at } \psi = 1 \quad (5.16)$$

$$\xi(\psi, t^*) = 0 \quad \text{at } \psi = 0 \quad (5.17)$$

$$\xi(\psi, 0) = 0 \quad \text{at } t^* = 0 \quad (5.18)$$

$$-\frac{\partial \xi}{\partial \psi} = \alpha \frac{dR(t^*)}{dt^*} \quad (5.19)$$

where the ratio of the latent heat of fusion to sensible heat of the liquid is called the Stefan constant:

$$\alpha = \frac{L}{C_{pl}(T_o - T_m)} \quad (5.20)$$

The equations are solved by introducing the following transformation:

$$V(\psi, t^*) = \psi * \xi(\psi, t^*) \quad (5.21)$$

Applying the transformations to the system of equations results in the following heat equation and Dirichlet boundary conditions:

$$\frac{\partial V}{\partial t^*} = \frac{\partial^2 V}{\partial \psi^2} \quad (5.22)$$

$$\xi(1, t^*) = 1 \rightarrow V(1, t^*) = \xi_o = 1 \quad (5.23)$$

$$\xi(0, t^*) = 0 \rightarrow V(0, t^*) = 0 \quad (5.24)$$

$$\xi(\psi, 0) = 0 \rightarrow V(\psi, 0) = 0 \quad (5.25)$$

where  $\kappa$  represents the thermal diffusivity,  $\lambda/\rho C_p$ , of the liquid phase. The above relations represent a form of non-homogenous heat transfer problem. Apply separation of variables and use the methods of Brown and Churchill [75] and Guffy [76] for

transformations to spherical coordinates, to obtain the following solution for the temperature profile in the form of a Fourier series:

$$\xi(\psi, \sigma) = 1 - \frac{2}{n^2 \pi} \left[ \sum_{n=1}^{\infty} \frac{(-1)^n}{n} \left( 1 - e^{(-n^2 \sigma / \pi)} \right) \sin(n^2 \psi^2) \right] \quad (5.26)$$

where

$$\sigma = \lambda t / a^2_s \quad (5.27)$$

The Fourier series in Eq. (5.26) provides the temperature profile within the melting spherical particle. Higher order terms are neglected and then the temperature profile is applied to the Stefan boundary condition in Eq. (5.19). Following integral and differential numerical procedures as described by Mosally et al. [77], and applying a one-step Simpson's rule, the position of the transition surface is obtained as the solid particle melts. Figure 5.1 indicates the variables and conditions in the phase change analysis. Following the temperature profile, a step by step method was applied to obtain the position of the interface via a Matlab algorithm. At small Stefan number (i.e., large  $\Delta T$ ), the particle vanishes in almost linear proportion to the dimensionless time  $\theta$ . The rate of disappearance becomes asymptotic as the Stefan number becomes larger (i.e., small  $\Delta T$ ). The model represents the melting rate of a particle of  $\text{CuO} \cdot \text{CuCl}_2$ .

### 5.3 Resistances

The moving interface of the physical problem of phase change of a particle of  $\text{CuO} \cdot \text{CuCl}_2$  can be related to the conversion rate as the solid reactant produces molten

product. The resulting differences between this model and the rate of reaction of decomposition kinetics provide a measure of the resistances associated to the decomposition of  $\text{CuO} \cdot \text{CuCl}_2$ . A simultaneous heat and mass transfer process occurs while the particle decomposes. The time needed for the particle to decompose and melt completely is assumed to approximately match the time needed for oxygen gas to evolve out of the particle. Oxygen gas diffuses through the liquid layer of the particle, which is the same layer through which heat is conducted from the surface of the particle to the solid core.

At the particle surface, the overall resistance is a result of heat, chemical reaction and mass diffusion resistances. These resistances are higher at lower temperatures as indicated from experiments by lower conversions of  $\text{CuO} \cdot \text{CuCl}_2$ . Although the decomposition of  $\text{CuO} \cdot \text{CuCl}_2$  is assumed to be isothermal, the driving force for heat transfer is a temperature differential, which competes for dominance with the driving force for the movement of oxygen based on the gas concentration differential. Several past studies have analyzed the phenomenon of diffusion from a particle and assumed the bulk concentration to be zero, hence creating a driving force for gas evolution (Daggupati et al. [52]). Hindering effects produce an overall resistance that is a function of heat transport, mass transport and chemical reaction resistances as discussed in Cussler [79]:

$$r_A = r_p \left( \frac{1}{1/\mathbb{R}_1 + 1/\mathbb{R}_2 + 1/(\mathbb{R}_3 K_e)} \right) \quad (5.28)$$

where  $r_A$ ,  $r_p$  are the adjusted rate and the phase change rate, respectively. The resistances  $\mathbb{R}_1$ ,  $\mathbb{R}_2$ ,  $\mathbb{R}_3$  represent thermal, mass diffusivity and chemical reaction resistance,

respectively. The chemical reaction resistance is impacted by the equilibrium constant for the chemical reaction,  $K_e$ , resulting from the equilibrium between the forward and reverse reactions. Hence, assuming that all resistances of the chemical reaction, mass diffusion and thermal diffusion contribute to the thermal resistance, this yields the following general expression:

$$r_A = r_p \cdot f(\rho, L_c, C_p, \lambda) \quad (5.29)$$

The adjusted rate equals the phase change rate adjusted by a function of bulk density of the material  $\rho$ , the characteristic length of the sample,  $L_c$ , the specific heat capacity,  $C_p$ , and the thermal conductivity of the sample. The phase change model assumes a uniform temperature through the solid portion of the sample. Therefore, the spatial temperature variation is neglected and the overall thermal conductivity of the sample is represented by the thermal conductivity of CuCl. These variables contribute to the thermal diffusivity that may be interpreted in terms of a characteristic time  $\tau$  required to change the temperature of the particle. It is defined as:

$$\tau = \frac{L_c^2}{\lambda} \quad (5.30)$$

where  $L_c^2 = V_p / A_c$  is the characteristic length of the system (Naterer [120]). The overall resistance is impacted by the rate of heat transfer through the liquid phase into the sample.

## Chapter 6 - Model of Thermochemical Decomposition

---

### 6.1 Physical Problem Description

The model in this chapter starts from the general equations for the analysis of chemical transport phenomena (Froment and Bischoff [105]). A schematic of the physical phenomena of a solid particle under chemical decomposition and the released species of liquid and gaseous phases are shown in Fig. 5.1. It is assumed that the heat required for the reaction and the phase change is gained by thermal conductivity through the molten phase, then into the moving interface and the solid particle. Simultaneously, the gaseous phase with bubbles moves as a result of either density differential or concentration differential that promotes convective transport of gas and heat away from the reaction zone. The chemical decomposition of the solid occurs over a range of temperatures defined between  $T_m$  and  $T_o$ . For the thermal decomposition of  $\text{CuO} \cdot \text{CuCl}_2$ , these limits are known to be 430 °C and 530 °C, and decomposition beyond 530 °C is not favoured due to the exponential increase of the CuCl vapour pressure.

#### 6.1.1 Continuity Equation

The mass continuity equation applied to chemical reactors was thoroughly discussed by Froment and Bischoff [105]. The equation can be applied to a continuous, plug or batch reactor by following the appropriate simplifications. The assumptions and simplifications are discussed further down in this section. The general equation of mass continuity with reacting species is given as follows:

$$\frac{\partial C_j}{\partial t} + \nabla \cdot (C_j \vec{u}_j) + \nabla \cdot \left( -\bar{\rho}_f D_{jf} \nabla \frac{C_j}{\rho_f} \right) = Rr_j \quad (6.1)$$

where the terms in the equation from left to right represent the transient accumulation or depletion of species  $j$ ; the transport of species  $j$  by convective flow; the diffusion of species  $j$  in a binary system; and the total rate of change of species  $j$  due to a chemical reaction, respectively. The rate of reaction term is negative for reactants and positive for products.

Consider a particle initially at a temperature  $T_m$  suddenly immersed in a continuum at temperature  $T_o > T_m$ . The fluid is assumed quiescent such that heat transfer by convection is significantly smaller in comparison to the heat transfer by conduction, indicating a relatively low Peclet number, and low Reynolds numbers within the control volume due to radial diffusion of gas away from the solid particle. It is assumed that heat conduction inside the solid occurs faster than heat convection at the surface, and that spatial temperature gradients are negligible. Therefore, from Eq. (6.1):

$$\frac{\partial C_s}{\partial t} + \nabla \cdot (C_s u_s) + \nabla \cdot \left( -\bar{\rho}_f D_{sl} \nabla \left( \frac{C_s}{\rho_f} \right) \right) = -Rr_s \quad (6.2)$$

$$\frac{\partial C_l}{\partial t} + \nabla \cdot (C_l u_l) = Rr_l \quad (6.3)$$

$$\frac{\partial C_g}{\partial t} + \nabla \cdot (C_g u_g) = Rr_g \quad (6.4)$$

where the subscripts  $s$ ,  $l$ ,  $g$  refer to solid, liquid and gas phases respectively. It is assumed that there is convective and diffusive transport of solids in the liquid, and that diffusive transport of gas in the binary system of gas and liquid can be neglected. Assuming that the

particle decomposition occurs as a first order surface reaction, the concentrations within the control volume maintain the following relation:

$$\frac{\partial C_s}{\partial t} = 2 \frac{\partial C_l}{\partial t} = \frac{1}{2} \frac{\partial C_g}{\partial t} \quad (6.5)$$

Adding Eqns. (6.2- 6.4) and substituting:

$$-3.5 \frac{\partial C_s}{\partial t} + \nabla \cdot (C_s u_s) + \nabla \cdot (C_l u_l) + \nabla \cdot (C_g u_g) - \nabla \cdot \left( \bar{\rho}_f D_{sl} \nabla \left( \frac{C_s}{\rho_f} \right) \right) = -3.5 R r_s \quad (6.6)$$

where the total change of moles due to the rate of reaction of each species are related by

$$-R r_s = 2 R r_l = \frac{1}{2} R r_g \quad (6.7)$$

The transport phenomenon is directly correlated to the slip velocity at the surface of the particle. Using the procedure of Pfeffer and Happel [87] drag forces on a sphere falling in a fluid field produce a velocity field with vector components in the radial and angular directions. In the following analysis, the velocity field is decomposed into the undisturbed terminal velocity and the disturbed radial velocity due solely to the chemical decomposition of the solid core. Assume the velocity field is equal to the terminal velocity acting on the center of the particle and a radial velocity component that results from the radial mass transport of gas and liquid products as follows:

$$u_g = y_g \frac{\partial R}{\partial t} \quad (6.8)$$

$$u_l = y_l \frac{\partial R}{\partial t} \quad (6.9)$$

Daggupati et al. [48] analyzed the decomposition of  $\text{CuCl}_2$  into  $\text{CuCl}$  and  $\text{Cl}_{2(g)}$  and assumed that the rate of decomposition is controlled by the rate of desorption of gas

from the interface. They assumed that the principle of equi-molar counter diffusion applies and determine an equivalent binary diffusion term in order to calculate the gas concentration. They also applied a spherical geometry relationship to determine the concentration of solid as a function of the changing radius,  $r$ . In a similar approach, Pfeffer and Happel [87] analysed the dissolution of solid particles embedded in a spherical volume of larger size than the volume of the particle. The spherical control volume was used for the initial calculation of concentrations. This section uses a similar procedure and assumes that a perfect spherical shape of the solid is maintained during the chemical decomposition. The concentration of solid within a spherical volume of initial radius “ $b$ ” can be calculated as:

$$C_s = \frac{n_s}{V_o} = \tilde{\rho}_s \left( \frac{R}{b} \right)^3 \quad (6.10)$$

The concentration is estimated with respect to the fraction of each phase in the fluid as follows:

$$C_l = y_l \rho_f \frac{(b^3 - R^3)}{b^3} \quad (6.11)$$

$$dC_l = -3y_l \tilde{\rho}_f \frac{R^2}{b^3} dR \quad (6.12)$$

$$C_g = y_g \rho_f \frac{(b^3 - R^3)}{b^3} \quad (6.13)$$

$$dC_g = -3y_g \tilde{\rho}_f \frac{R^2}{b^3} dR \quad (6.14)$$

It is also assumed that the density remains uniform between phases. The average density of fluids in the decomposition phenomenon is estimated from the sum of densities

at equilibrium averaged over the total number of moles present. The overall density of the fluid is a function of the number of moles present at any time in each phase,

$$\tilde{\rho}_f = \sum_i n_i \tilde{\rho}_i / n_T \quad (6.15)$$

where the total number of moles is given by:

$$n_T = n_s + n_l + n_g \quad (6.16)$$

Assume that the density of each phase remains constant through the transient phenomena.

Thus, following Eq. (6.6):

$$n_s = (1-x)\bar{\rho}_s V_s; \quad n_l = 2x\bar{\rho}_l V_s; \quad n_g = \frac{1}{2}x\bar{\rho}_g V_s \quad (6.17)$$

Therefore, the fluid density can be approximated as:

$$\bar{\rho}_f = \frac{\frac{1}{2}x\bar{\rho}_g + 2x\bar{\rho}_l + (1-x)\bar{\rho}_s}{\frac{1}{2}x + 2x + (1-x)} \quad (6.18)$$

It is assumed that the reaction at the interface reaches instantaneous equilibrium during the transient process, such that the concentration of gas versus the average fluid density  $C_g/\rho_f$  can be approximated by the mole fraction of the gas at equilibrium, “ $y_g$ ”. Referring to the decomposition of  $\text{CuO}^*\text{CuCl}_2$ , it occurs according to the following stoichiometric equation:



The phenomenon under consideration occurs at a low pressure and therefore it is assumed that the gas phase follows ideal gas behaviour. Therefore, the equilibrium constant in terms of fugacity is based on the stoichiometric relation of the chemical decomposition as follows:

$$K = \frac{\left(\frac{f_l}{f_l^o}\right)^2 \left(\frac{f_g}{f_g^o}\right)^{1/2}}{\left(\frac{f_s}{f_s^o}\right)} \quad (6.20)$$

For low pressure systems, the terms for the solid and liquid phases become unity. Also, the fugacity for ideal gas behaviour can be equated to the partial pressure of the gas, where  $f_o$  is equal to the atmospheric pressure. Therefore, the equilibrium constant equals the square root of the partial pressure of oxygen, indicating that the solid dissociates until the partial pressure of oxygen reaches the square of the value of the equilibrium constant at a given temperature. The equilibrium constant is calculated based on the Gibbs free energy for the stoichiometric reaction. The equilibrium values in Table 6.1 were obtained based on the following expression:

$$\Delta_r G^o = \Delta H - T\Delta S = G_{prod} - G_{react} \quad (6.21)$$

Table 6.1: Partial pressure of oxygen at equilibrium

<b>T (K)</b>	<b><math>\Delta G_o</math> (kJ/mol)</b>	<b>K</b>	<b>P<sub>O2</sub> (bar, abs)</b>
298.15	68.7	9.07E-13	9.52E-07
400	56.1	4.71E-08	2.17E-04
600	29.8	2.54E-03	5.04E-02
703	15.5	7.04E-02	2.65E-01
723	12.0	1.34E-01	3.66E-01
773	3.4	5.81E-01	7.63E-01
803	-1.7	1.29E+00	1.14E+00

After expanding the differential operators in Eq. (6.1), the chain rule is applied to the first term, higher order terms are neglected, radial velocities are substituted from Eqns. (6.8, 6.9), and spatial velocity profiles are neglected to obtain the following form of mass continuity equation:

$$\begin{aligned}
& -10.5\tilde{\rho}_s \frac{R^2}{f^3 a^3} \frac{\partial R}{\partial t} + 3u_{ts} \tilde{\rho}_s \frac{R^2}{f^3 a^3} - 3 \left( y_l^2 \tilde{\rho}_f \frac{R^2}{f^3 a^3} \right) \frac{\partial R}{\partial t} - 3 \left( y_g^2 \tilde{\rho}_f \frac{R^2}{f^3 a^3} \right) \frac{\partial R}{\partial t} - 6\tilde{\rho}_s D_{sl} \frac{R}{f^3 a^3} \\
& = -3.5Rr_s
\end{aligned} \tag{6.22}$$

### 6.1.2 Energy Equation

The thermal energy change within a particle balances the energy gained through the liquid phase by conduction, energy transported by the released gas phase and the thermal energy of reaction. It is assumed that heat is transported by conduction through the liquid phase and convection through the gas bubbles. Also, it is assumed that the net exchange of thermal radiation between the liquid and solid bodies is relatively small and that radiation heat exchange can be lumped together with an equivalent heat transfer coefficient to arrive at the following expression:

$$\bar{\rho}_s C_{ps} \frac{\partial T_s}{\partial t} = \nabla \cdot (\lambda_l \nabla T_l) - \bar{\rho}_g C_{pg} u_g \nabla T_g - (\Delta H) Rr_s \tag{6.23}$$

Expanding the differential operators and disregarding higher order terms leads to the following form of the energy equation:

$$\bar{\rho}_s C_p \frac{\partial T_s}{\partial t} = 2 \frac{\lambda_l}{R} \frac{\partial T_l}{\partial R} + \bar{\rho}_g C_{pg} u_g \frac{\partial T_g}{\partial R} - (\Delta H) Rr_s \tag{6.24}$$

### 6.1.3 Momentum Equation

Consider the phenomenon of solid particles falling in a quiescent fluid and experiencing both phase change and chemical reaction in the range of mid Stefan numbers ( $Ste \approx 1$ ). The dynamics of the solid particle has characteristics similar to those observed by Gan et al. [98, 99]. The fluid surrounding the particle is assumed quiescent as the

particle shrinks. A variable velocity profile develops with time. In this analysis, assume that the particle remains spherical through the period of decomposition and the velocity of the particle is determined by the balance of drag and buoyancy forces due to the differences of the density of solid-liquid phases as described by the following Navier-Stokes equation:

$$\frac{\partial}{\partial t}(\bar{\rho}_f u_s) + u_s \nabla \cdot (\bar{\rho}_f u_s) = -\nabla s + \sum F \quad (6.25)$$

For steady flow at low Reynolds numbers, the transient term  $\rho(\partial u / dt)$ , convective acceleration and the second order tensor  $\nabla s$  (pressure gradient) are neglected, and the balance of momentum of the particle yields:

$$F_D + V_s(\rho_s - \rho_l)g + F_{PG} + F_{VM} + F_L = 0 \quad (6.26)$$

where the forces acting on the particle are drag, buoyancy, pressure gradient, virtual mass and lift.

The process of decomposition occurs fast enough for the force of hydrodynamic pressure gradient,  $F_{PG}$ , to be negligible. Since the particle is not accelerated at a high rate, the virtual mass force  $F_{VM}$  is neglected. Furthermore, since there is no component of fluid velocity perpendicular to the main particle displacement, the lift force  $F_L$  is neglected.

$$F_D + V_s(\rho_s - \rho_l)g = 0 \quad (6.27)$$

Using the solution to the Stokes equation in the flow regime of  $Re < 0.2$ , the drag coefficient is calculated by equating the drag equation to the Stokes equation:

$$6\pi\mu u_{st}R + \frac{4}{3}\pi R^3 \rho_s g = \frac{4}{3}\pi R^3 \rho_l g \quad (6.28)$$

leading to the following terminal velocity of the particle:

$$u_{st} = \left( \frac{2R^2}{9\mu} \right) (\rho_p - \rho_l) g \quad (6.29)$$

In order to complete the problem formulation, boundary and initial conditions are required.

#### 6.1.4 Boundary and Initial Conditions

The concentrations of products within the control volume are assumed zero at the moment when the particle reaches the terminal velocity. Also, a zero radial temperature gradient is assumed in the solid particle, and the Stefan condition applies to the liquid phase exclusively. The following initial and boundary conditions are obtained:

$$C_l = 0 \text{ at } t = 0 \quad (6.30)$$

$$C_g = 0 \text{ at } t = 0 \quad (6.31)$$

$$Rr = 0 \text{ at } t = 0 \quad (6.32)$$

$$T = T_m \text{ at } R = 0 \quad (6.33)$$

$$T = T_o \text{ at } R = a \quad (6.34)$$

$$\rho_l h_{st} \frac{\partial R}{\partial t} = -\lambda_l \frac{dT_l}{dR} \quad (\text{at } R(t)) \quad (6.35)$$

In the next section, these governing equations will be re-written in non-dimensional form.

### 6.1.5 Dimensional Analysis and Scaling

The dimensional analysis of transient decomposition of solid particles via equilibrium follows the methodology explained by Ruzicka [106]. Dimensional analysis of the governing equations provides the order of magnitude of individual terms. The mass continuity equation is characterized by the parameters ( $D$ ,  $\rho$ ) and the dimensional variables ( $t$ ,  $m$ ,  $R$ ,  $u$ ) that contain the fundamental physical units ( $m$ ,  $u$ ). There exist two dimensionless quantities that define the phenomena. In fundamental units, the mass continuity equation can be written as:

$$\rho \frac{L^2}{L^3} \frac{L}{t} + V \rho \frac{1}{L} - \rho \frac{L^2}{L^3} \frac{L}{t} - \rho \frac{L^2}{L^3} \frac{L}{t} - \rho \frac{DL}{L^3} = Rr \quad (6.36)$$

which simplifies to:

$$\frac{1}{Pe_m} = (Da)^2 \quad (6.37)$$

where  $Da = ((Rr*t)/\rho_0)^{1/2}$ . Hydrodynamic convection balances the rate of reaction and the diffusive transport by having similar impact in the overall phenomenon.

Similarly, the energy equation is characterized by the parameters ( $\Delta H$ ,  $C_p$ ,  $\rho$ ) and the dimensional variables ( $T$ ,  $t$ ,  $m$ ,  $R$ ,  $u$ ) that are constituted in the fundamental physical units ( $T$ ,  $m$ ,  $u$ ). This indicates that there exist two dimensionless quantities that define the phenomena. In fundamental units, the energy equation can be written as:

$$\frac{T}{t} = -\frac{\Delta H}{C_p} \frac{Rr}{\rho} + \frac{\lambda}{\rho C_p} \frac{T}{L^2} + V \frac{T}{L} \quad (6.38)$$

$$\frac{T}{t} = -\frac{RrT}{\rho} + \kappa \frac{T}{L^2} + V \frac{T}{L} \quad (6.39)$$

$$1 = -Da + \frac{1}{Pe_T} + 1 \quad (6.40)$$

Following the mass continuity analysis, the  $Pe_T$  term is also small and therefore neglected in the solution of the energy equations.

In scaling of the state equations, the following dimensionless variables are adopted:

$$t = \frac{\rho_s C_{ps} a^2}{\lambda} t^* \quad (6.41)$$

$$r = \frac{R}{a} \quad (6.42)$$

$$Da = \left( \frac{Rr_s a^2}{C_{so} D_{sl}} \right)^{1/2} \quad (6.43)$$

$$U^* = \frac{u_{st} a}{D_{sl}} \quad (6.44)$$

$$\theta = \frac{T_s - T_m}{T_o - T_m} \quad (6.45)$$

$$\xi = \frac{T_l - T_m}{T_o - T_m} \quad (6.46)$$

The mass, energy and momentum equations become:

$$(3y_i^2 \bar{\rho}_s + 3y_g^2 \bar{\rho}_s + 10.5)r^2 Lew \frac{\partial r}{\partial t^*} - 3U^* + 6r = 3.5Da^2 \quad (6.47)$$

$$\frac{\partial \theta}{\partial t^*} = -rr - \frac{1}{Ste} \frac{\partial r}{\partial t^*} \left( \frac{2}{\rho_s^* r} + y_g \frac{\rho_g^*}{\rho_s^*} \frac{\partial r}{\partial t^*} \right) \quad (6.48)$$

$$(Re)^2 = \frac{\rho_s (u_{st})^3}{(\Delta \rho) g \nu} \quad (6.49)$$

where  $\rho_s^* = \frac{\widetilde{\rho}_f}{\rho_s}$ ,  $\rho_g^* = \frac{\widetilde{\rho}_g}{\rho_s}$ , and  $rr = \frac{(\Delta H) Rr_s a^2}{\lambda (T_o - T_m)}$  are dimensionless variables. These

equations are solved subject to the following non-dimensional initial and boundary conditions:

$$\theta = 0 \quad \text{at} \quad t^* = 0 \quad (T_s = T_m) \quad (6.50)$$

$$x = 0 \quad \text{at} \quad t^* = 0 \quad (Rr_s = 0) \quad (6.51)$$

$$U^* = u_t \quad \text{at} \quad t^* = 0 \quad (V_s = V_t) \quad (6.52)$$

$$\xi = \theta \quad \text{at} \quad r = 0 \quad (T_l = T_s) \quad (6.53)$$

$$\xi = 1 \quad \text{at} \quad r = 1 \quad (T_l = T_o) \quad (6.54)$$

$$\frac{\partial \xi}{\partial r} = 0 \quad \text{at} \quad r = 1 \quad (T_l = T_s) \quad (6.55)$$

$$\frac{\partial r}{\partial t^*} = -Ste \frac{d\xi}{dr} \quad (\text{Stefan condition}) \quad (6.56)$$

Assume a quadratic profile for the liquid phase temperature  $\xi$  with the following conditions:

$$\xi = \theta \quad \text{at } r = 0 \quad (6.57)$$

$$\xi = 1 \quad \text{at } r = 1 \quad (6.58)$$

$$\frac{\partial \xi}{\partial r} = 0 \quad \text{at } r = 1 \quad (6.59)$$

Therefore, this leads to the following profile for the dimensionless liquid temperature:

$$\xi = (1 - \theta)r^2 + 2(1 - \theta)r + \theta \quad (6.60)$$

This completed the model of the transport phenomena. In the next chapter, a case study of hydrogen utilization and application to trains will be presented.

## Chapter 7 - Results and Discussions

---

### 7.1 Pathways of Chemical Decomposition

Two mechanistic approaches to the decomposition of copper oxychloride in prior chapter indicated that one of the paths may prevail depending on the temperature, pressure and side products/reactants present in the sample that result from the presence of unreacted products from hydrolysis. A potential mass imbalance occurs as undesirable side reactions arise in the oxygen reactor with chlorine leaving the reactor in gaseous form, and  $\text{CuCl}_2$  with the solids. In complete decomposition, the oxygen production reaction results in a pure liquid phase of molten  $\text{CuCl}$  and oxygen. Instead, the conversion rates obtained in experiments and measured from TGA conducted in this thesis indicated values between 65 and 95%, indicating that the conversion follows the competing reactions discussed (path A and path B) and results in a mix of  $\text{CuCl}$ ,  $\text{CuCl}_2$ ,  $\text{Cl}_2$  and  $\text{O}_2$  in the product streams. It was found in the experiments that a gas mixture with oxygen, chlorine and  $\text{CuCl}$  vapour was produced.

The decomposition of  $\text{CuO} \cdot \text{CuCl}_2$  appeared to start at different temperatures, depending upon the temperature of the environment. In batch reactor experiments, the sample released oxygen at an initially high rate, while semi-batch experiments indicated an initially low rate of oxygen formation, followed by a trend to steady state. This trend occurred at a later time in lower temperature experiments.

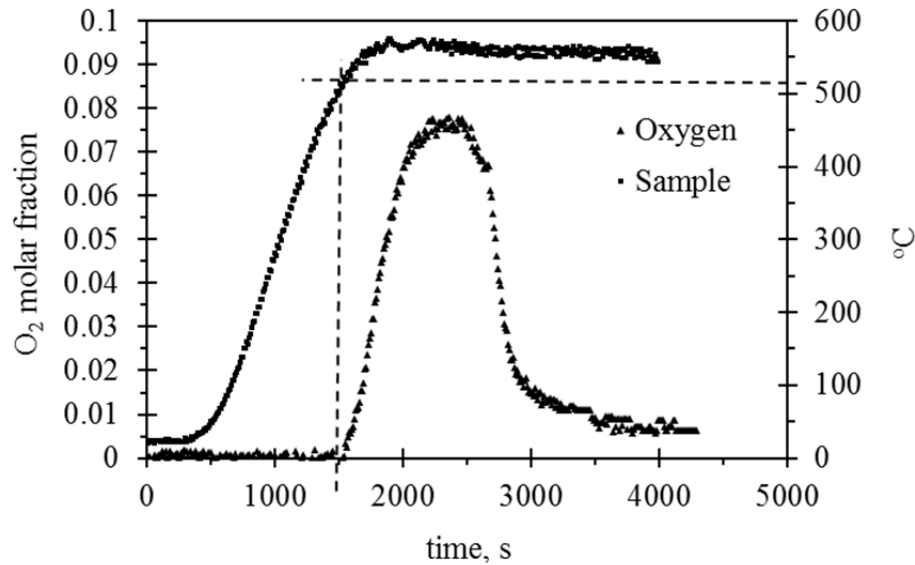


Fig. 7.1 Oxygen formation from decomposition of a 50 g. batch of  $\text{CuO}\cdot\text{CuCl}_2$  at 570 °C and 1.003 atm

Figure 7.1 illustrates the oxygen evolution vs. time from the batch reaction experiments. The readings corresponded to a decomposition experiment where a well-mixed sample of  $\text{CuO}$  powder and dehydrated  $\text{CuCl}_2$  powder was heated to 570 °C. Decomposition of the 50 g sample was monitored for one hour until the oxygen readings were undetectable. With the reactor temperature set to reach 570 °C in the sample, the decomposition appeared to start at 500 °C as indicated in Fig. 7.1. The decomposition of  $\text{CuO}\cdot\text{CuCl}_2$ , as measured from oxygen formation, occurred consistently in all experiments with three characteristic stages, 1) initial rush with high rate of oxygen generation; 2) a brief plateau where oxygen generation seemed to stabilize; and 3) an asymptotic decay of the rate of decomposition where oxygen generation slowly falls to close to zero. The time distributions of these phenomena indicated that the initial increase,

plateau and decay stages lasted for approximately 15%, 20% and 65% of the total time, respectively.

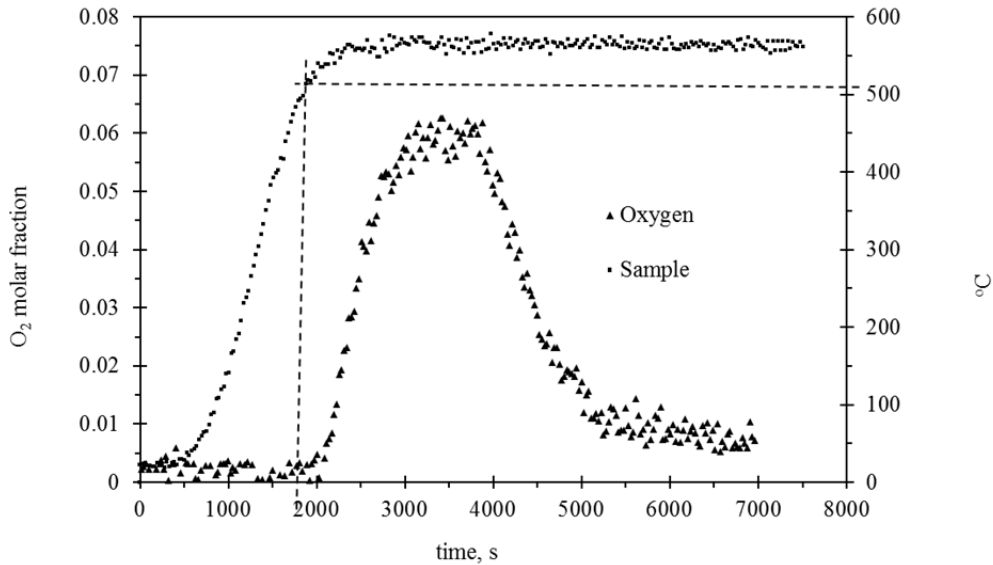


Fig. 7.2: Oxygen formation from decomposition of a 100 g. batch of  $\text{CuO} \cdot \text{CuCl}_2$  at average temperature of  $560^\circ\text{C}$  and 1.003 atm

At  $560^\circ\text{C}$ , the rate of formation of oxygen increases to reach an instantaneous peak of 0.06 moles. The sample continues to decompose at this peak rate for a long period and then decays asymptotically as indicated in Fig. 7.2. Up to 95% of the decomposition occurs within the first hour, with the remaining decomposition taking twice as much time to reach undetectable levels. A large amount of  $\text{CuCl}$  deposit on the walls and sample weight loss were observed from samples of experiments at  $570^\circ\text{C}$  and  $560^\circ\text{C}$ . The weight losses were approximately 10% of the initial weight after the weight of oxygen as indicated in Figs. 7.1 and 7.2 was removed from calculations.

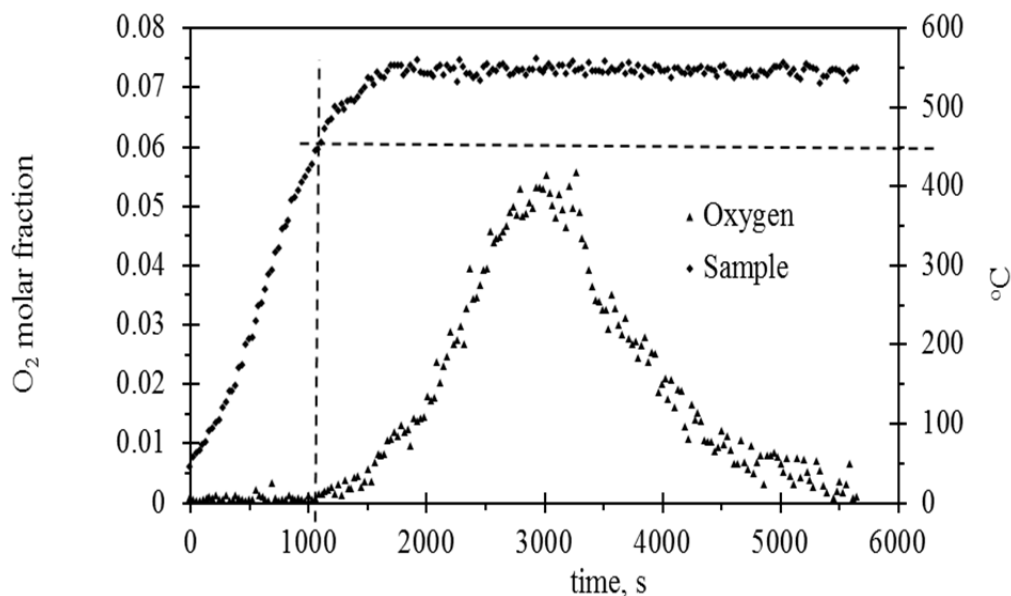


Fig. 7.3: Oxygen formation from decomposition of a 100 g. batch of  $\text{CuO}\cdot\text{CuCl}_2$  at average temperature of  $530\text{ }^\circ\text{C}$  and  $1.003\text{ atm}$

Heating of the sample to the average temperature of  $530\text{ }^\circ\text{C}$  initiated the formation of oxygen when the sample reached the average temperature of  $450\text{ }^\circ\text{C}$ , as indicated in Fig. 7.3. The curve of oxygen formation is nearly symmetric with a short lived peak at approximately  $0.055\text{ mol}$  of  $\text{O}_2$ . At this temperature, the asymptotic decay of oxygen formation seemed to be a shorter time when compared to the total time for decomposition at higher temperatures. The evaporation of  $\text{CuCl}$  is still high and a similar order of magnitude as the experiments at higher temperatures.

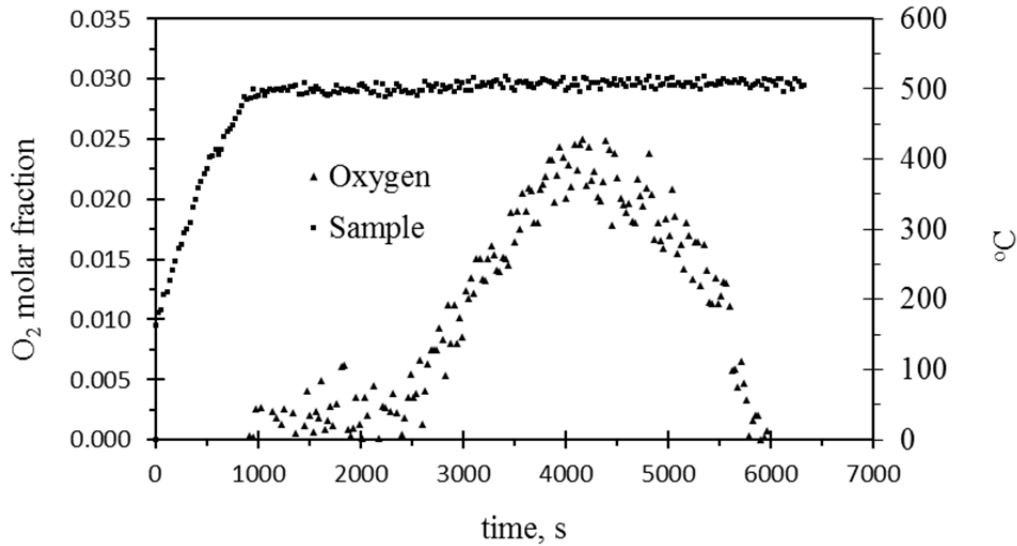


Fig. 7.4: Oxygen formation from decomposition of a 100 g batch of  $\text{CuO}\cdot\text{CuCl}_2$  at average temperature of  $490\text{ }^\circ\text{C}$  and  $1.003\text{ atm}$

At the average temperature of  $490\text{ }^\circ\text{C}$ , the formation of oxygen peaks at the instantaneous value of  $0.025\text{ mol}$ , as indicated in Fig. 7.4. The slope of the ascending rate of oxygen formation is lower when compared to experiments at higher temperatures. The evaporation of  $\text{CuCl}$  as measured from weight differences is also smaller. The curve decays rapidly to undetectable values after a short peak. The formation of oxygen started with sample reaching the average temperature of  $490\text{ }^\circ\text{C}$ . Although some  $\text{CuCl}$  evaporated and had deposits on the walls of the reactor, the amount is significantly less when compared with higher temperatures. Also, the curve of formation of oxygen is approximately symmetric and undetectable after one hour of the experiment.

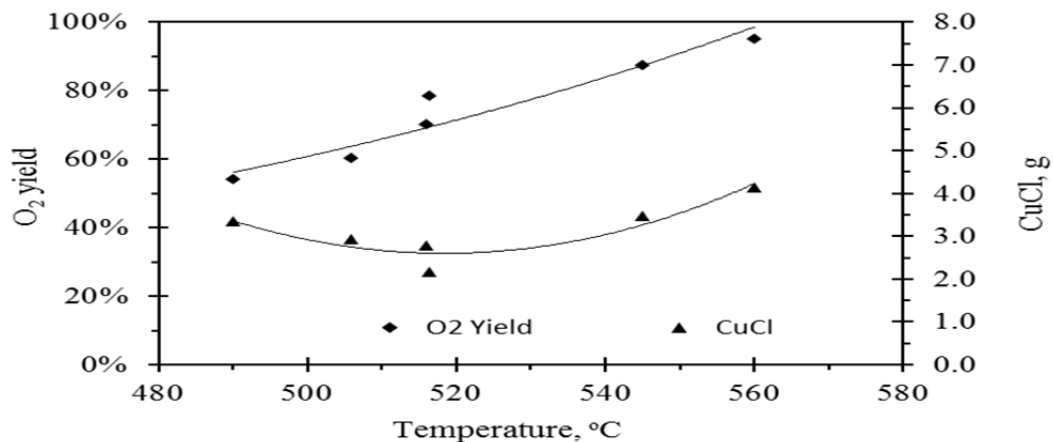


Fig. 7.5: Oxygen yield and CuCl weight loss due to evaporation from samples of 100 g of  $\text{CuO} \cdot \text{CuCl}_2$  at different temperatures

Higher oxygen yields from decomposition at higher average temperatures resulted in a trend of high CuCl evaporation as indicated in Fig. 7.5. The rate of evaporation does not decay in proportion to the yield as seen from the curve in Fig. 7.6. A trend to increase the net amount of CuCl evaporated at lower temperatures may be due to longer times required for decomposition. Thus, it was inferred that CuCl vapour is carried away with oxygen gas and also evaporated from the surface. Although less gas is produced at lower temperatures, still the weight losses of CuCl vapour are comparable to losses at high temperatures.

Figure 7.6 indicates the results of decomposition of a mix of  $\text{CuO} \cdot \text{CuCl}_2$  in a semi-batch reactor configuration. The sample was supplied into a molten bath containing 0.5 mol of CuCl at the average temperature of 490 °C. The data, averaged over periods of five minutes and three experiments at each temperature, were collected for a total of five to six hours. It provides an indication of the behaviour of the decomposition reactions with

increasing concentration. At 490 °C and an average feed rate of 0.085 mol of mixture of solid  $\text{CuO}\cdot\text{CuCl}_2$ , a high rate of decomposition was observed during the first hour of the experiment as indicated by the slope of the curve. A change in the slope of the curve suggests that additional resistances to the decomposition reaction appear with the increased concentration. The sample is fed in the form of fine particles distributed over the molten salt, such that the average values are an approximate representation for the phenomena. The experiment was stopped before conclusive behaviour was observed. However, the curve indicates that the rate of decomposition stabilizes at approximately 0.0006 mol/min.

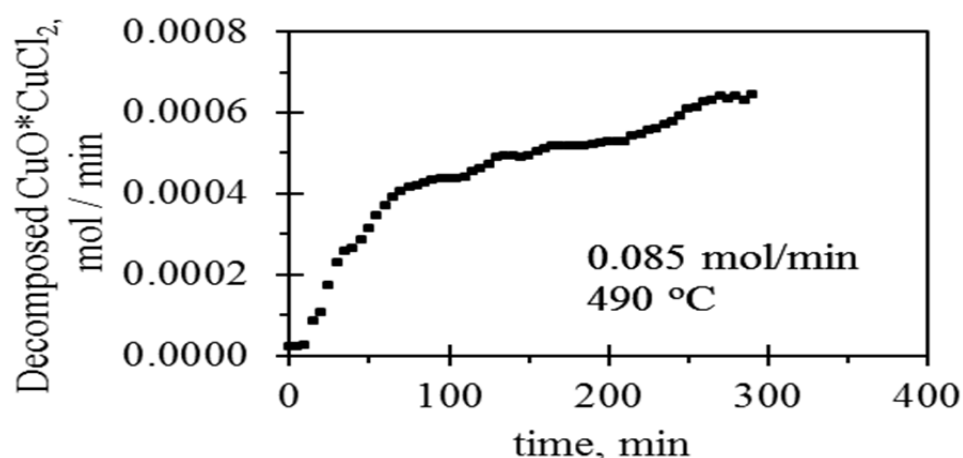


Fig. 7.6: Decomposition of  $\text{CuO}\cdot\text{CuCl}_2$  in a semi-batch operation with a feed rate of 0.085 mol/min and average bath temperature of 490 °C

At a higher temperature of the bath, the decomposition is fast during the first 40 minutes and then slows down to a steady, increasing rate as indicated by the slopes of the curve in Fig. 7.7. At 510 °C, and a feed rate of 0.085 mol/min of solid  $\text{CuO}\cdot\text{CuCl}_2$ , the rate of decomposition occurs approximately 1.5 faster than at 490 °C. No stabilization of

the decomposition rate was observed during the experiments. The data indicated the increased presence of resistances associated with the increased concentration of solids within the molten salt. However, the phenomenon did not indicate a steady state behaviour that allows a conclusive observation of the effect of increased concentration of solids on the rate of decomposition. The higher temperature of the experiment, compared to Fig. 7.7 suggested that to obtain a steady rate of decomposition, longer operation is required, thus indicating a critical ratio of concentration of solids vs. molten CuCl at which the rate of decomposition becomes steady.

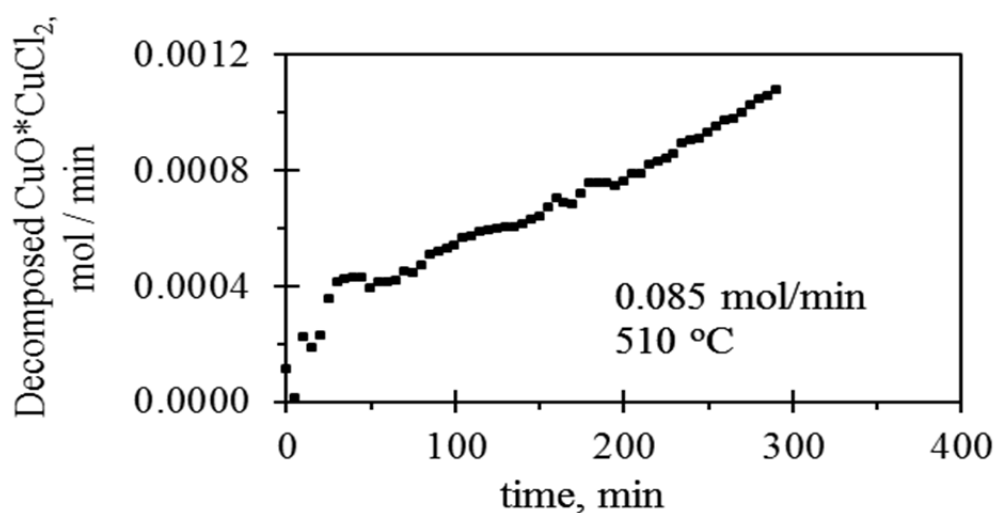


Fig. 7.7: Decomposition of CuO\*CuCl<sub>2</sub> in a semi-batch operation with a feed rate of 0.085 mol/min and average bath temperature of 510 °C

The data in Fig. 7.8 is the result of separate experiments conducted at 530 °C and an average feed rate of solids of 0.085 mol/min. The rate of decomposition is high during the first two hours of the experiment, with rates three to four times higher than the experiments at 490 and 510 °C. After approximately two hours, the system seems to reach

steady state conditions where the rate of oxygen and molten CuCl generation balances the rate of addition of solids at 0.085 mol/min. An approximation to a steady state condition can be observed between the second and fifth hours of experimentation. This observation indicates that the resistances to chemical decomposition reach a critical point due to the concentration of solids versus the molten liquid and gas evolution rates. After approximately the fourth hour, the slope of the curve started to change and became negative with a progressive accentuation of the effect. The change of slope is presumably due to the increased presence of solids fed into the molten salt that eventually inhibit the rate at which heat reaches the particles. This effect contributed to the increased presence of gas bubbles and led to reduced heat transfer within the system and longer time for heat to reach the solid particles.

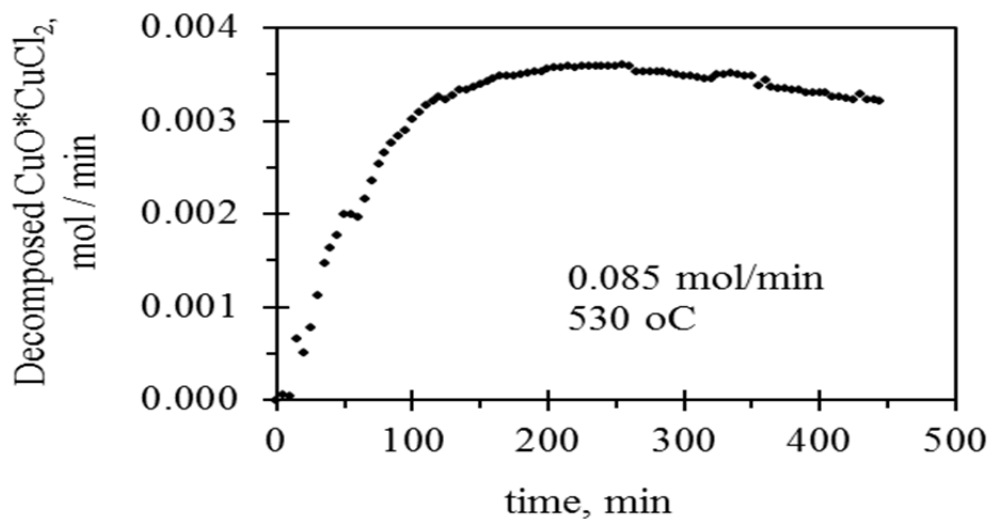


Fig. 7.8: Decomposition of  $\text{CuO} \cdot \text{CuCl}_2$  in a semi-batch operation with a feed rate of 0.085 mol/min and average bath temperature of 530 °C

At the average molten salt temperature of 490 °C, the formation of CuCl is initially characterized by a high rate as indicated by the slope of the curve within the initial 60 min in Fig. 7.9. As CuCl is formed, the amount of CuO\*CuCl<sub>2</sub> present in the crucible increases linearly with respect to the volume of molten salt. The slope of the curves indicates that the concentration of fed solids increases steadily in a linear manner, while the concentration of unreacted solids decays at a certain time and concentration value. This is presumably due to the additional volume of molten CuCl as inferred from the CuCl formation curve.

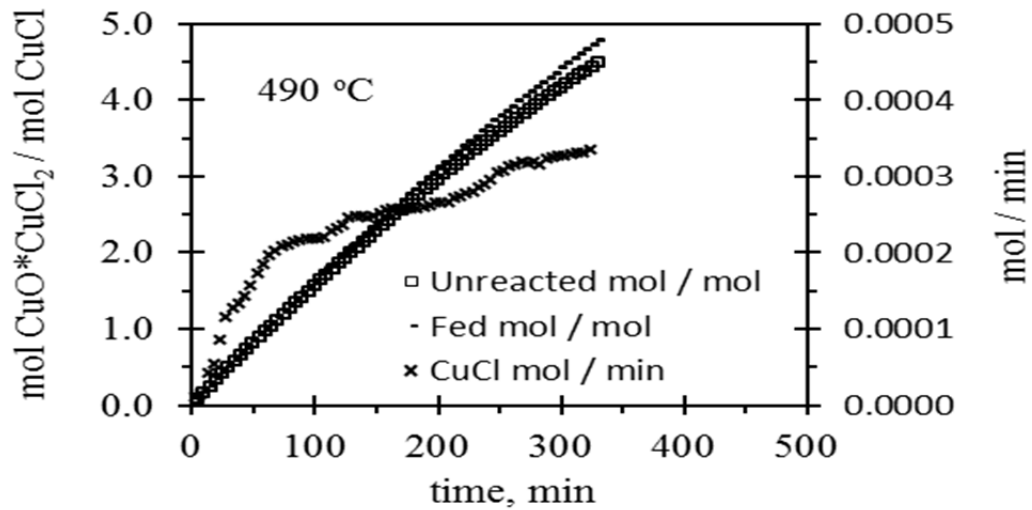


Fig. 7.9: Concentration of unreacted solids in molten salt at 490 °C vs. formation of molten CuCl

At the average molten salt temperature of 510 oC, the concentration of solids in the molten salt increases linearly, while the accumulation of unreacted solids increases linearly and decays slightly after two hours of the experiment. The decay, as indicated in Fig. 7.10 is more pronounced at the higher temperature of 510 °C compared to Fig 7.9. It

can be observed that  $\text{CuO} \cdot \text{CuCl}_2$  decomposes slightly faster at this higher temperature as indicated by a larger slope of the  $\text{CuCl}$  formation curve.

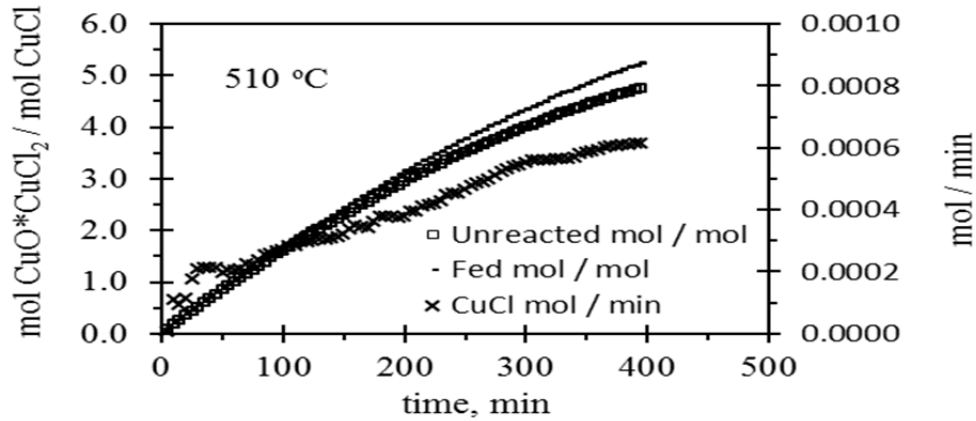


Fig. 7.10: Concentration of unreacted solids in molten salt at 510 °C vs. formation of molten  $\text{CuCl}$

The formation of  $\text{CuCl}$  reaches a steady state condition at approximately 0.0018  $\text{mol/min}$  with an average molten  $\text{CuCl}$  temperature of 530 °C. The rate of formation decays after some time with the addition of more  $\text{CuO} \cdot \text{CuCl}_2$  as indicated in Fig. 7.11. This is expected by the decomposition of solids indicated in Fig. 7.9. At this temperature, the concentration of solids fed to the reactor vs.  $\text{CuCl}$  is no longer linear, The accumulation of unreacted solids decays with the generation of  $\text{CuCl}$ . This decay is however due to the increased volume of molten salt since a plot of absolute accumulation of solids vs. time indicated that it remains linear. Thus, it can be inferred that the decomposition rate decays not only as a consequence of the concentration of solids increasing, and also, presumably as a result of the increased presence of gas bubbles in the molten salt.

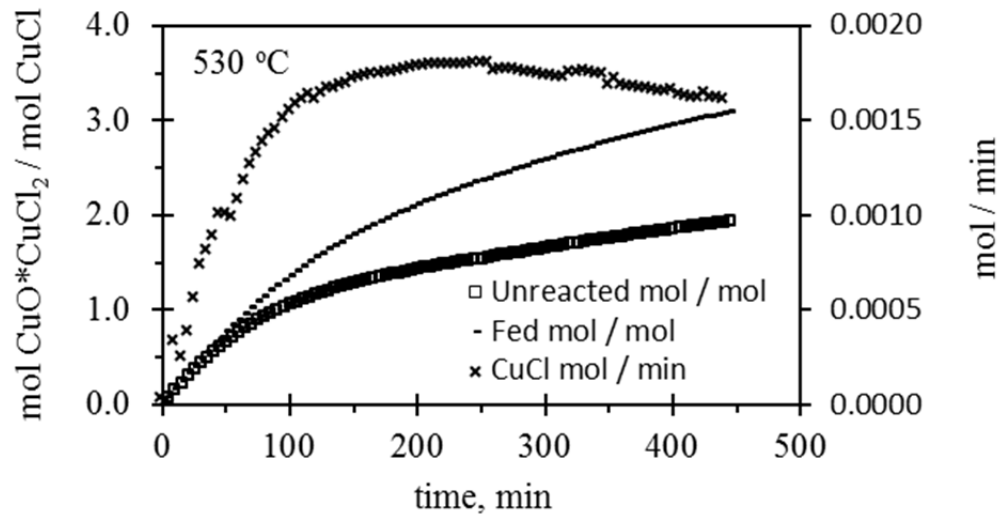


Fig. 7.11: Concentration of unreacted solids in molten salt at 530 °C with formation of molten CuCl

The accumulation of unreacted solid is higher with lower molten salt temperatures as indicated in Fig. 7.12. The ratio of unreacted to fed CuO\*CuCl<sub>2</sub> decays linearly with time and seems to reach steady state, indicating that a large portion of solids remains unreacted with average temperatures at 490 °C. At the higher temperature of 510 °C, the ratio of unreacted to fed solids continued to decay, with no indication of stabilization within the time of experiments. A large difference of the ratios of accumulation exists with respect to experiments at the average temperature of 530 °C. The ratio of unreacted solids decays rapidly and seemed to reach steady state after 350 min. There is also a trend to increase in the concentration of unreacted CuO\*CuCl<sub>2</sub> at the end of the experiments. This effect can be inferred from the decay in decomposition of solids and formation of molten CuCl as indicated in Figs. 7.8 and 7.11.

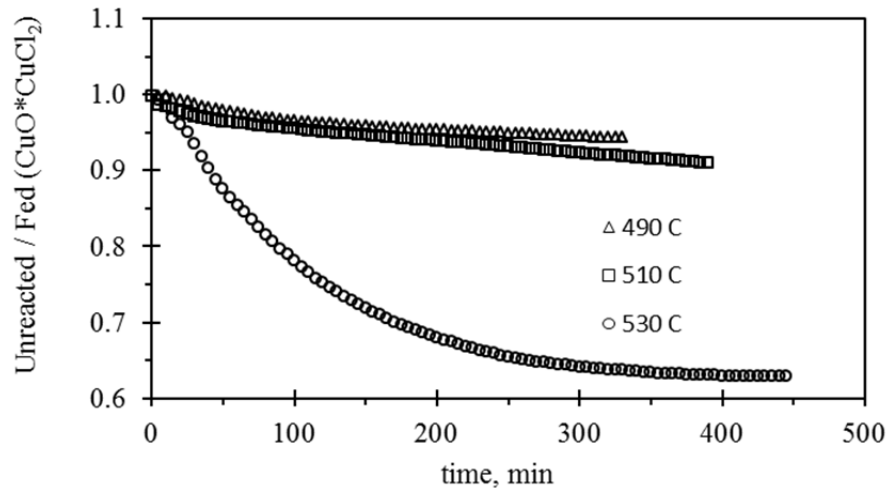


Fig. 7.12: Ratio of unreacted vs. fed  $\text{CuO} \cdot \text{CuCl}_2$  at several average temperatures of molten  $\text{CuCl}$

Figure 7.13 illustrates the behaviour of partial pressures of the gaseous product from the decomposition of  $\text{CuO} \cdot \text{CuCl}_2$  and  $\text{CuCl}_2$ , respectively in the range of temperatures up to 530 °C. The occurrence of  $\text{CuCl}$  vapour is anticipated because the melting point of  $\text{CuCl}$  is 430 °C, well below the temperature of experiments.  $\text{CuCl}$  vapours have also been observed in past research during decomposition experiments. However,  $\text{CuCl}$  vapours condense as soon as gases exit the reactor, given the high temperature differential between the ambient and phase change temperature of  $\text{CuCl}$ .

The results indicate that the overall impact of  $\text{CuCl}$  vapours in the evolution rate of gases is not obvious. The partial pressure of chlorine is several orders of magnitude larger than  $\text{CuCl}$  vapour. However, the partial pressure of  $\text{CuCl}$  rises rapidly beyond 430 °C. A sudden phase change may result in solid particles carried over with the oxygen gas stream.

The results of decomposition of  $\text{CuCl}_2$  are shown in Fig. 7.13 together with past results reported in the literature.

A significant volume of  $\text{Cl}_2$  in the gaseous products during decomposition of  $\text{CuO}\cdot\text{CuCl}_2$  is believed to be produced from the decomposition of  $\text{CuCl}_2$ , as suggested from the equations in Path B. Researchers have reported oxygen evolution above the amount indicated by equilibrium at the temperature of the experiment. Since the reactant for the oxygen production included  $\text{CuCl}_2$ , then chlorine gas was present in the products.

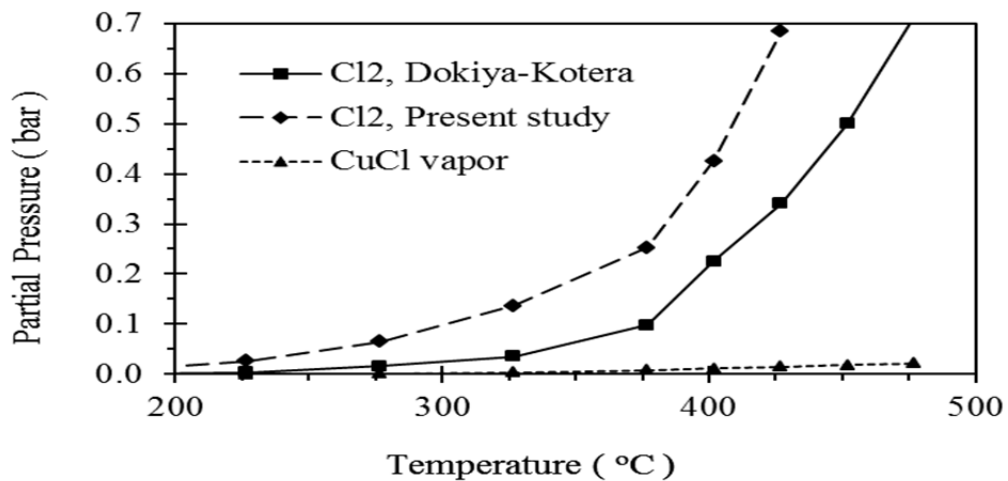


Fig. 7.13: Partial pressure of chlorine at equilibrium with the decomposition of  $\text{CuCl}_2$ .  
(Dokiya-Kotera at 92 mm Hg vs. Present study at atmospheric conditions)

From the aspect of integration with the upstream hydrolysis reaction, this means that if the extent of reaction in hydrolysis is below completion and the hydrolysis products contain un-reacted  $\text{CuCl}_2$ , when these hydrolysis products are decomposed in the downstream oxygen production reactor, it may also result in the release of undesirable chlorine gas together with oxygen. This becomes a safety and efficiency concern since

additional steps and energy are required to separate chlorine from the oxygen and recycle the gases back through the cycle. The experimental results are consistent with proof-of-principle tests performed by Serban et al. [59] in a thermogravimetric analysis of the decomposition of  $\text{CuCl}_2$ . The experiments used 50 mg of  $\text{CuCl}_2$  heated to temperatures of 600 °C and the authors reported weight losses of 8.6 mg, equivalent on a stoichiometric basis to a 63% chlorine release.

Figure 4.5 shows the thermodynamic analysis of the decomposition of  $\text{CuCl}_2$ . At the temperature of 430 °C, the Gibbs energy of decomposition of  $\text{CuCl}_2$  becomes negative and thereby the reaction becomes spontaneous. Within that same range of temperature, the reaction of copper oxide with chlorine is also spontaneous as indicated by the Gibbs energy in Fig. 4.5. To visualize the compositions in the output stream of oxygen production, the thermodynamic results for the competing reactions in paths A and B are also shown in Fig. 4.5. The Gibbs energy curves also provide a comparison with variations 1 and 2 of the Cu-Cl cycle, specifically for the decomposition of copper oxychloride. As  $\text{CuO}$  reacts with chlorine, some  $\text{CuCl}$  and  $\text{CuCl}_2$  form and oxygen is released. The negative Gibbs energy of reaction between  $\text{CuO}$  and  $\text{Cl}_2$  favors the formation of  $\text{CuCl}_2$  over  $\text{CuCl}$  as indicated in Fig. 4.6. When  $\text{CuCl}_2$  is entrained by the copper oxychloride in the products of hydrolysis, it continues to decompose spontaneously beyond 470 °C and beyond what can possibly react with the available  $\text{CuO}$ , resulting in chlorine gas evolution together with oxygen.

To study the effect of operating pressure on the chemical streams among integrated reactions, the Gibbs energy of the competing reactions is used at low and standard

pressures in Fig. 4.4. At 0.1 bar, the decomposition of  $\text{CuCl}_2$  reaches equilibrium at 370 °C and becomes spontaneous above that temperature. By comparison, the decomposition of  $\text{Cu}_2\text{OCl}_2$  at the same temperature and pressure is not spontaneous. Experimental results indicated that copper oxychloride is stable up to the temperature of 430 °C. Between 435 °C and 470 °C, it decomposes with the formation of  $\text{CuCl}$ ,  $\text{CuCl}_2$  and chlorine. The mechanistic analysis suggested by path B indicates that the released  $\text{Cl}_2$  then reacts with  $\text{CuO}$  to produce  $\text{CuCl}$  and  $\text{O}_2$ . The Gibbs free energy of reaction in Fig. 4.6 indicates that the second reaction occurs as soon as chlorine is available in the system. Also, the slope of the Gibbs curve in Fig. 4.7 indicates that more  $\text{CuCl}_2$  decomposes at low pressure and within the same temperature range compared to operating at atmospheric pressure. Operating at pressures below atmospheric pressure does not change the mechanics of the reactions. Figure 4.7 also shows (through the difference of slopes between the curves at 1 bar and 0.1 bar) that the advantages of lowering the temperature threshold of the oxygen production reactor may be compromised with the additional mechanical energy requirement and with the presence of more chlorine in the gas products.

The solid products of oxygen production from the mixture of  $\text{CuO}$  and  $\text{CuCl}_2$  appear as a black hard sintered material, as shown in Fig. 7.14. The solid product of decomposition of the  $\text{CuO} \cdot \text{CuCl}_2$  mixture has identical physical appearance samples from the decomposition of copper oxychloride. The solids are mildly hygroscopic, and they can be pulverized with the utilization of mechanical effort.

The products of decomposition have a fragile solid appearance once at ambient temperature. The solid is porous and breaks with medium effort, indicating that an

additional process must be introduced for the cycle integration before the downstream electrolysis reaction.



Fig. 7.14: Sample of products of copper oxychloride decomposition

The cake of solid  $\text{CuCl}$  must be mechanically removed from the oxygen production reactor and then pulverized. In this condition, the solids can be dissolved in water and  $\text{HCl}$  for the preparation of aqueous solution needed by the electrolytic hydrogen production cell. Since the  $\text{CuCl}$  must be first solidified, thermal energy recuperated from the phase change of molten salts from the decomposition reactor can be used elsewhere in the  $\text{Cu-Cl}$  cycle for thermal energy integration.

The analysis based on XRD powder techniques of the composition of the solid product of the oxygen production resulted in patterns of Fig. 7.15. The spectrum revealed a mixture of solids where copper oxide, copper (II) chloride and copper (I) chloride were present. The major product component is  $\text{CuCl}$  with mixed quantities of  $\text{CuCl}_2$  and  $\text{CuO}$ . The analysis of the relative amounts of XRD peaks with reference to standard samples

indicated an approximate composition of solids of 70% CuCl and 20% CuCl<sub>2</sub>. The results of XRD analysis appear to confirm the pathways of the decomposition reaction as discussed above with a combination of products of paths A and B.

From the aspect of the process integration, Fig. 7.16 shows that the un-reacted CuCl<sub>2</sub> in the hydrolysis reactor may not be fully decomposed in its downstream oxygen production reaction. Therefore, CuCl<sub>2</sub> may be further carried by CuCl to the downstream cell for the electrolytic hydrogen production. This same situation occurs with CuO present in the stream output from the oxygen reactor. This situation significantly reduces the possibility of adopting certain variations of integration of the Cu-Cl cycle.

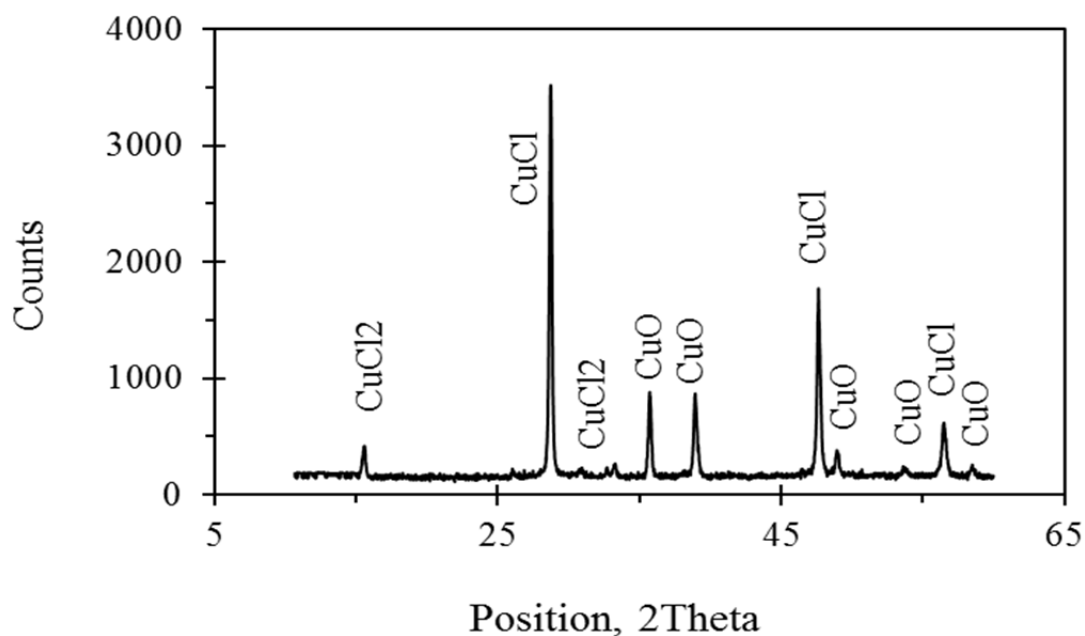


Fig. 7.15: XRD Reflections of products of decomposition of copper oxychloride at 550 °C.

Based on data in Fig. 7.15 if the residence time in the decomposition reactor is longer than the experiments reported in this thesis, chlorine gas will evolve out of the residual  $\text{CuCl}_2$ . The theoretical results and yields of  $\text{CuCl}_2$  decomposition were compared against experimental data of the decomposition of excess  $\text{CuCl}_2$  in the oxygen reactor, as shown in Figs. 7.15 and 7.16.

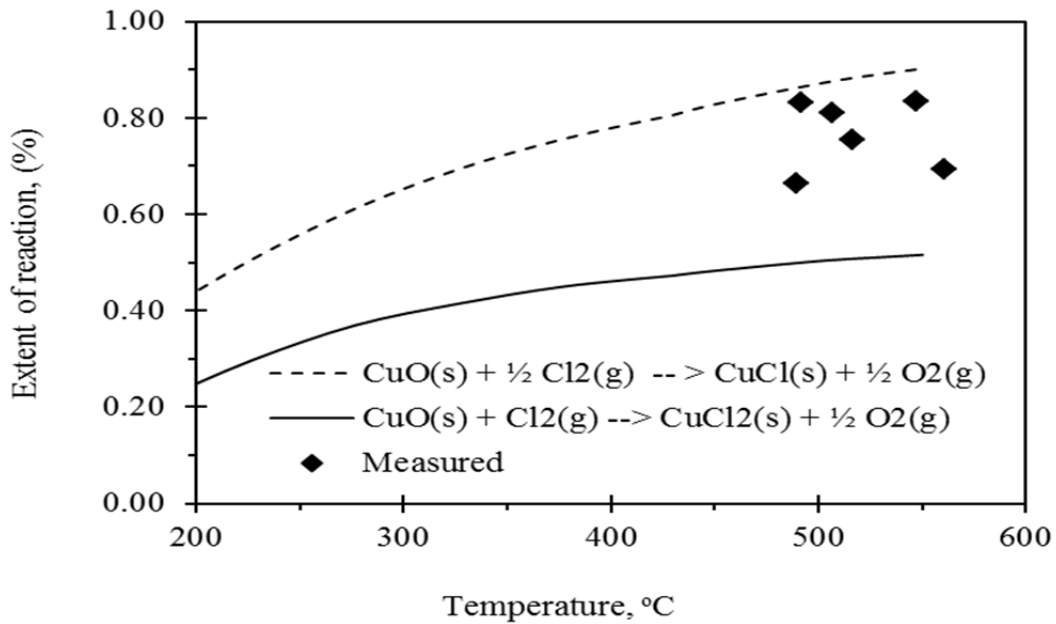


Fig. 7.16: Equilibrium analysis of extent of reaction vs. experimental results for the decomposition of copper oxychloride at temperatures from 450 °C to 560 °C, and atmospheric pressure

Figure 7.16 illustrates results of the equilibrium analysis and the extent of competing reactions under two separate approaches. At equilibrium, Fig. 7.8 indicated that the conversion of the mixture of  $\text{CuO} + \text{CuCl}_2$  is between 50% and 80% at 530 °C when operated at atmospheric pressure. The extent of reaction of decomposition of  $\text{CuO} \cdot \text{CuCl}_2$  falls within the predictions of the two individual competing reactions to the

predictions of the reaction paths A and B. In the analysis, the partial pressures of oxygen and chlorine in the reactor rise up to four orders of magnitude larger than the partial pressure of CuCl vapour at temperatures between 450 °C and 560 °C indicated in Fig. 7.13. The experimental results in Fig. 7.16 are based on decomposition of a mixture of CuO\*CuCl<sub>2</sub> and they provide an indication of the total amount of chlorine released during the decomposition. It can be seen from the experimental results that the total chlorine falls within the range of moles of gas reacted through the two paths in consideration. At thermodynamic equilibrium, Fig. 7.17 shows that the products of decomposition of the mixture of CuO and CuCl<sub>2</sub> contain from 5% to 15% chlorine at atmospheric pressure. Also, chlorine release was observed in regular experiments with CuO\*CuCl<sub>2</sub> at temperatures above 470°C, which is consistent with the analysis of Fig. 7.7.

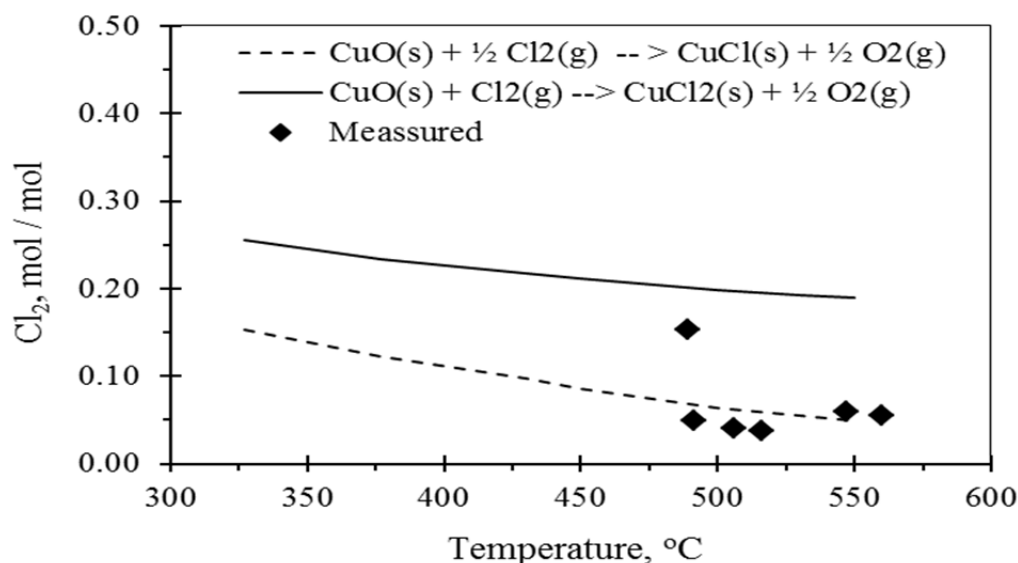


Fig. 7.17: Theoretical evolution of residual chlorine from excess CuCl<sub>2</sub> using proposed mechanistic analysis of reactions vs. experimental results in the range of 450 °C to 560 °C; 1 mol/L oxygen, and atmospheric pressure

The analysis indicates that at equilibrium, the decomposition reaction may result in a complex mixture of  $\text{CuO}\cdot\text{CuCl}_2$ ,  $\text{CuO}$ ,  $\text{CuCl}$ ,  $\text{CuCl}_2$ ,  $\text{O}_2$  and  $\text{Cl}_2$ , and other species that depend upon the contents of hydrolysis products. The results suggested that the reverse reaction must also be considered. Experiments to reproduce a reverse reaction with  $\text{CuCl}$  and oxygen did not result in production of copper oxychloride. However, the presence of  $\text{CuCl}_2$  and  $\text{CuO}$  may result in the formation of copper oxychloride that will decompose given the spontaneity of the decomposition reaction, according to the Gibbs energy of reaction, at temperatures beyond  $500\text{ }^\circ\text{C}$ . The standard Gibbs free energy of the reverse reaction in Fig. 4.3 suggests the spontaneity of the reaction in the temperature range, presumably due to the fact that the Gibbs free energy is negative for this reaction at the reaction conditions. This does not conflict with the experimental results because the oxygen partial pressure in the experiments was below the standard value with a partial pressure of  $\text{O}_2$  in the experiments below 1.0 bar, which may significantly lower the possibility of a reverse reaction based on the Gibbs free energy. This observation also suggests that the reverse reaction may be a function of the oxygen pressure in the reactor.

## **7.2 Reversibility of Decomposition Reaction**

The experiments of the reverse reaction did not result in detectable observations during preheating of  $\text{CuCl}$  and  $\text{O}_2$ . Furthermore, the XRD reflections (see XRD results in Figs. 7.18 – 7.21) did not show traces of  $\text{Cu}_2\text{OCl}_2$  after experiments. Several conditions can lead to these results. For example, the reverse reaction below  $450\text{ }^\circ\text{C}$  is too slow to be measured. The sensitivity of the oxygen sensor and XRD may not be sufficient to detect the composition change. Also, as suggested by the negative value of Gibbs free energy,

the reverse reaction did occur, and  $\text{Cu}_2\text{OCl}_2$  was produced. However, after heating to 450 - 510 °C, the  $\text{Cu}_2\text{OCl}_2$  decomposed back to  $\text{CuCl}$  and  $\text{O}_2$ , as indicated in Fig. 4.3 by the positive value of Gibbs energy within the temperature range. Under 430 °C,  $\text{CuCl}$  exists in the form of solid, and the mixing of oxygen and  $\text{CuCl}$  is not sufficient to facilitate the reverse reaction, indicating a mass transport limitation. This condition may also prevail in the mixture of molten  $\text{CuCl}$  and oxygen. Under normal operating conditions of 1 - 2 bars and 525 - 550 °C, and within the reaction time of interest, the reverse reaction can be neglected in the design and operation of the oxygen production reactor of the Cu-Cl cycle.

Table 7.1 summarizes the experimental results and reaction conditions. It can be observed that changes of the oxygen mass balance were below detectable levels in all experiments indicating that no reverse reaction can be detected at the temperatures of the experiment. This is expected based on the Gibbs energy of reaction. In order to have significant mixing and enhance the contact of  $\text{O}_2$  and  $\text{CuCl}$ , 2 to 3 times the oxygen quantity in excess of the stoichiometric balance was adopted in the experiments, and the operating time of each experiment was extended beyond one hour.

Table 7.1: Experimental conditions for the reaction of copper (I) chloride and oxygen

Set No.	T	Reactant purity <sup>(a)</sup>	Runtime	Ratio of total quantity <sup>(b)</sup>	Pressure	Inlet oxygen concentration	Oxygen decrease in reaction	Composition of product (by XRD)
	°C	%	hour	$\text{O}_2/\text{CuCl}$	bar	mole fraction	mole	% (+/- 3%)
1	450	99%	1	1.3	1.2	5%	0	$\text{CuCl}$
2	500	99%	1	1.3	1.2	5%	0	$\text{CuCl}$
3	500	99%	1	1.3	1.2	5%	0	5%wt $\text{CuO}$ 95%wt $\text{CuCl}$
4 <sup>(c)</sup>	500	99%	1	--	1.2	--	--	97% $\text{CuCl}$ 3% $\text{Cu(OH)Cl}$
(a) All sets of experiments used 0.5 mol of reactant and continuous air injection at 2 SLPM; (b) The stoichiometric ratio of $\text{O}_2$ to $\text{CuCl}$ is 0.5; (c) Baseline experiments with continuous nitrogen flow at 2 SLPM.								

Results from experiments at two temperatures were examined: 450 °C, just above the melting point of CuCl, and 500 °C, close to the transitional point of the Gibbs free energy of the reaction. Figures 7.18 – 7.21 show the XRD results that correspond to experiments No. 1 to 4 of Table 7.1. It can be noticed that no  $\text{Cu}_2\text{OCl}_2$  was produced in experiments that operated in the temperature range of 450 - 500 °C, although experiment No. 3 resulted in some produced CuO. As to the formation of CuO in experiment No. 3, it is believed that CuO may have been generated from moisture in the reactant CuCl during the preparation process because the purity of reactant CuCl is larger than 99%, but the CuO detected in the product is 5%.

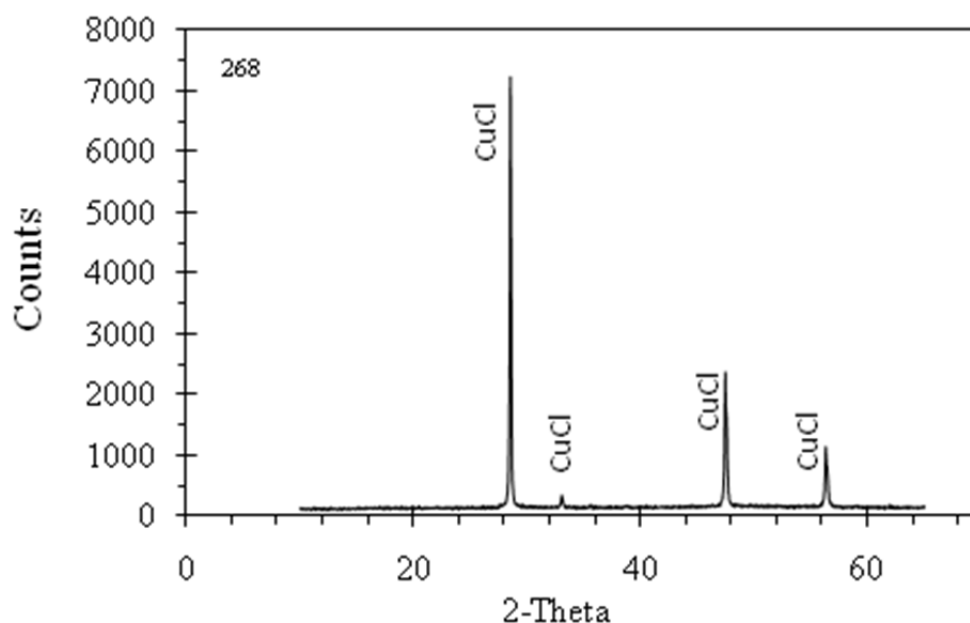


Fig. 7.18: XRD results of products of  $\text{CuCl} + \text{O}_2$  at 450 °C, 1-hour test (experiment set #1 in Table 7.1)

Experiment set # 2 at 500 °C confirms the predictions obtained from thermodynamic analysis, where the Gibbs energy of reaction becomes positive and the

reaction is not spontaneous. CuCl remained unchanged through the experiment as indicated from the XRD analysis in Fig. 7.18. No further experiments were performed at higher temperatures since the XRD and positive Gibbs energy of reaction from thermodynamic analysis did not indicate the probability of this path occurring at higher temperature.

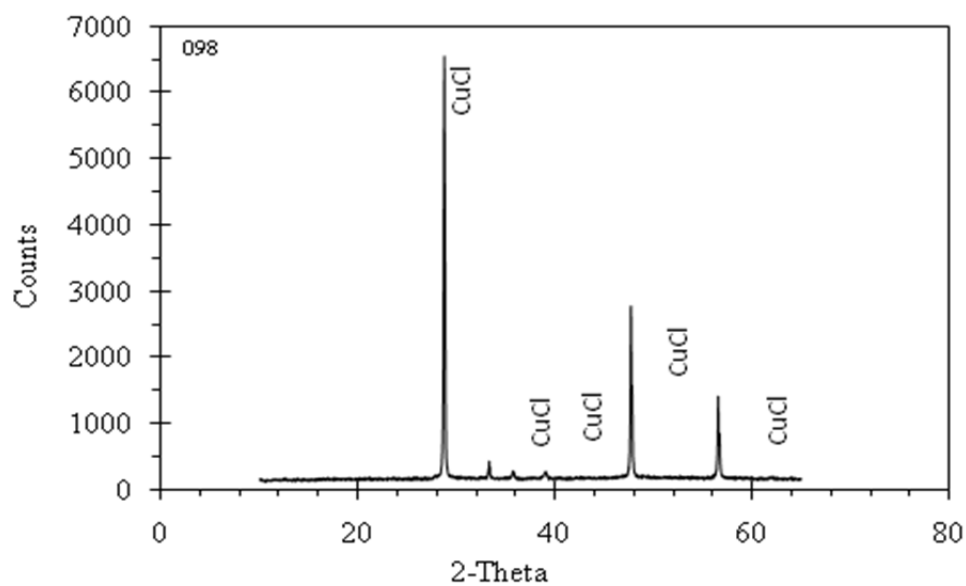


Fig. 7.19: XRD results of products of CuCl + O<sub>2</sub> at 500 °C, 1 hour test (experiment set #2 in Table 7.1)

The composition of the reactant CuCl for experiment No. 3 was analyzed to determine the level of impurity. As shown in Fig. 7.14, the only impurity in CuCl was found to be CuO-HCl, which may generate CuO through the following reaction discussed by Ramamurthy and Secco [63]:



It is believed that the hydrogen in CuOHCl occurred from moisture due to the presence of humidity when preparing the CuCl sample. It is unclear how the CuOHCl was formed in the CuCl during the process. However, past literature suggested that this compound may be the result of regular operation of the hydrolysis reaction.

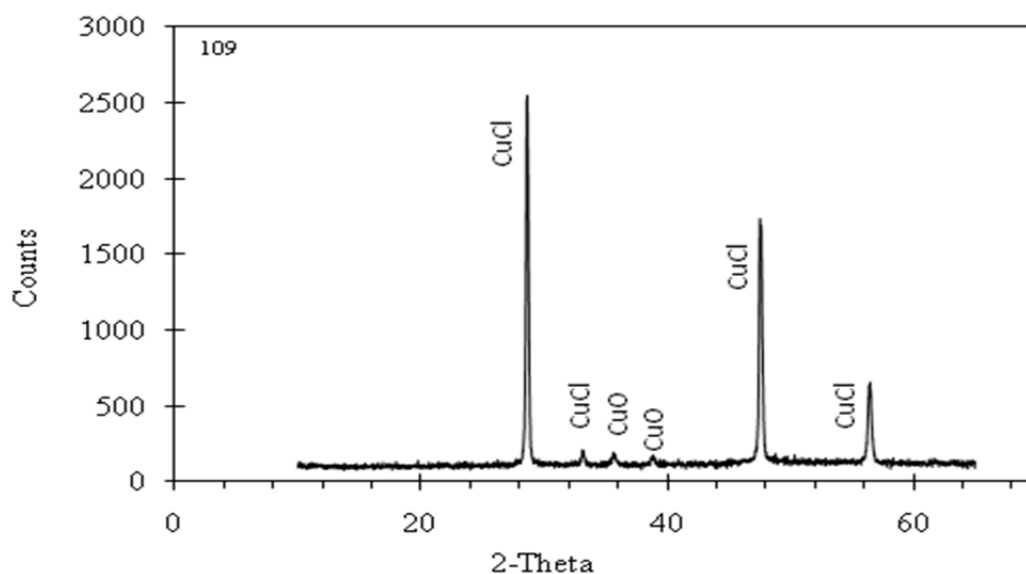


Fig. 7.20: XRD results of CuCl and O<sub>2</sub> at 500 °C, 1-hour test (experiment set #3 in Table 7.1)

The experimental results suggested that the reverse reaction in Eq. (4.4) has little likelihood to occur under the conditions in Table 7.1. The low likelihood of the reverse reaction to occur can be the result of two factors. First, the reverse reaction is not thermodynamically spontaneous within the range of temperatures proposed for the decomposition of copper oxychloride, and second, the reverse reaction is spontaneous, but the runtime for the reverse reaction is not long enough to produce significant amounts of Cu<sub>2</sub>OCl<sub>2</sub>; a direct consequence of mass transport limitations. If the reverse reaction is

spontaneous, then the run time must be very long, or the equipment size must be very large for the reverse reaction to produce measurable amounts of  $\text{Cu}_2\text{OCl}_2$ .

Experiment set # 4 resulted in solids with the presence of  $\text{CuCl}\cdot\text{OH}$  as indicated in Fig. 7.21. Since the samples are prepared from commercial grade species, it is believed that some humidity contamination may be present and this presumably is an explanation for the presence of OH.

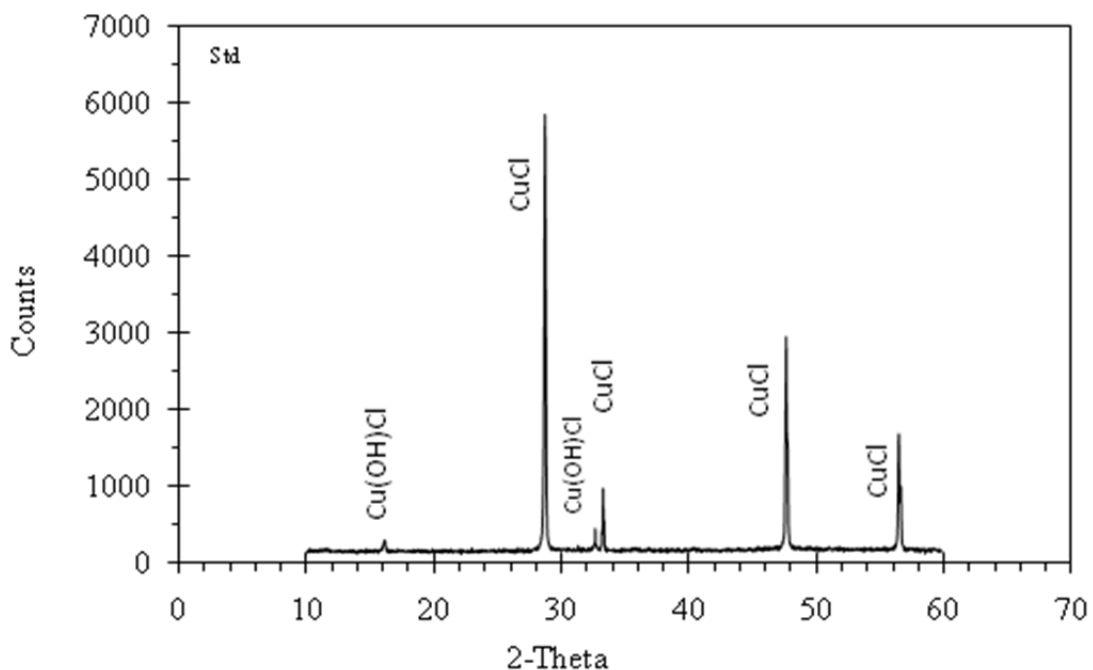


Fig. 7.21: Impurities in the  $\text{CuCl}$  reactant, molten at  $500\text{ }^\circ\text{C}$  (experiment set #4 in Table 7.1)

The above results and analysis of reaction paths, equilibrium and reverse reaction provide valuable information for the modeling of the multiphase reacting system. At the microscopic level, the system corresponds to the decomposition of solid reactant particles

and phase transition of a molten product at a gas-liquid-solid interface with kinetics determined through a reaction rate expression.

### 7.3 Rate of Reaction

The products of experimental decomposition of 100 g samples of  $\text{CuO}\cdot\text{CuCl}_2$  were first examined using XRD and Rietveld quantification. The quantification procedure yielded in errors of  $\pm 10\%$ . Figure 7.22 shows the spectrum obtained from XRD analysis of a sample of unreacted  $\text{CuO}\cdot\text{CuCl}_2$ . The sample was prepared from species of  $\text{CuO}$  and  $\text{CuCl}_2$  and well mixed in stoichiometric proportions. The Rietveld analysis from the XRD spectrum in Fig 7.22 resulted in 24.92%  $\text{CuCl}_2$  and 75.06%  $\text{CuO}$ . Applying this proportion to the original sample indicated a net error of  $\pm 7.5\%$ . This magnitude of error confirms the potential deviations expected from the analysis using a combination of XRD and Rietveld quantification.

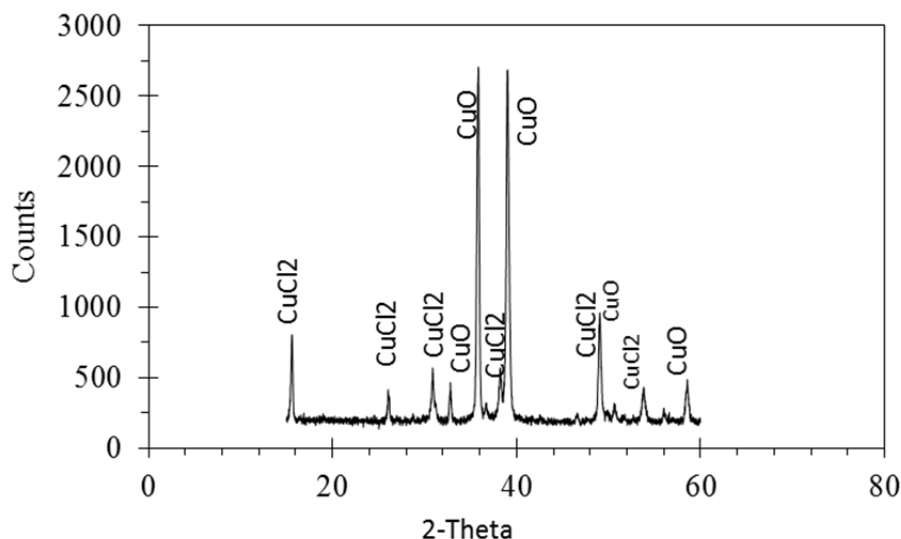


Fig. 7.22: X-Ray diffraction analysis of a standard sample of stoichiometric  $\text{CuO}\cdot\text{CuCl}_2$

The Rietveld quantitative analysis of samples was carried out using Bruker AXS Topas™ refinement software v 2.1 at the University of Toronto. The structural models for the identified components were taken from the Inorganic Crystal Structure Database (ICSD, 2005, Karlsruhe, Germany). The report indicated quantities calculated in percent weight by taking into account the chemical, structural and absorption properties of each one of the sample components. Fig. 7.23 indicates the ratio of solids found in the samples using XRD. The analysis indicated that CuO is present in all products of decomposition, with an increased ratio as the temperature of decomposition increased. This result suggests that chlorine is leaving the reaction zone before the chlorination of CuO can occur. This effect may be due to the presence of nitrogen as a carrier gas that facilitates the removal of gases from the reaction zone.

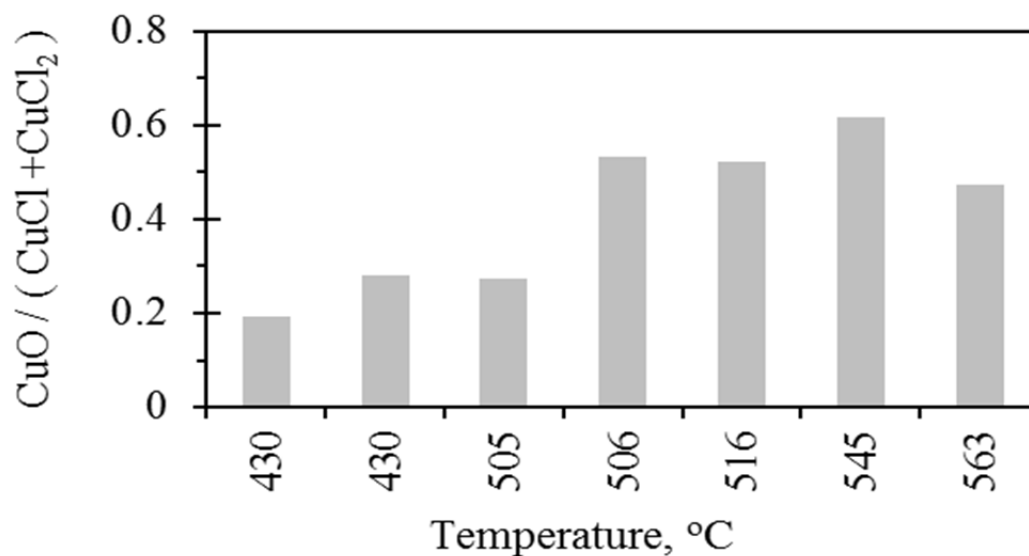


Fig. 7.23: Proportion of solids from Rietveld quantification of XRD analysis. Samples of decomposition of  $\text{CuO} \cdot \text{CuCl}_2$  at different temperatures.

The proportion of CuO was reduced at 563 °C. There are two reasons for this effect. First, the high temperature promotes the rapid decomposition and recombination of chlorine. Also, the vapour pressure of CuCl is high at this temperature, thus the total pressure of the system increases, reducing the mol fraction of nitrogen, oxygen and chlorine in the reactor. This effect presumably results in less chlorine escaping the reaction zone.

Experimental studies were performed separately in a batch-type vertical-split reactor and a thermogravimetric analyzer. A typical thermogravimetric experiment provided a weight curve with weight losses starting at between 425 to 430 °C, indicated by the change in the slope of the weight curve in Fig. 7.24. The rate of change of heat flow reaches a maximum peak and the weight curve experiences a sudden inflection at this same point. This is marked by a change of sign of the instantaneous change of heat flow versus time indicating that the sample has initiated a phase change process. Weight losses between 6% and 15% were measured following this event. The heat flow vs. time curve reaches a plateau and stabilizes, indicating that the decomposition has finished and a gradual phase change process at a constant heat flow rate has started, as can be observed from Fig. 7.24. The simultaneous decomposition and phase change with the presence of polymorphs of CuCl is indicated by the two successive peaks. The phase change of CuCl is accompanied by two different crystallographic structures.

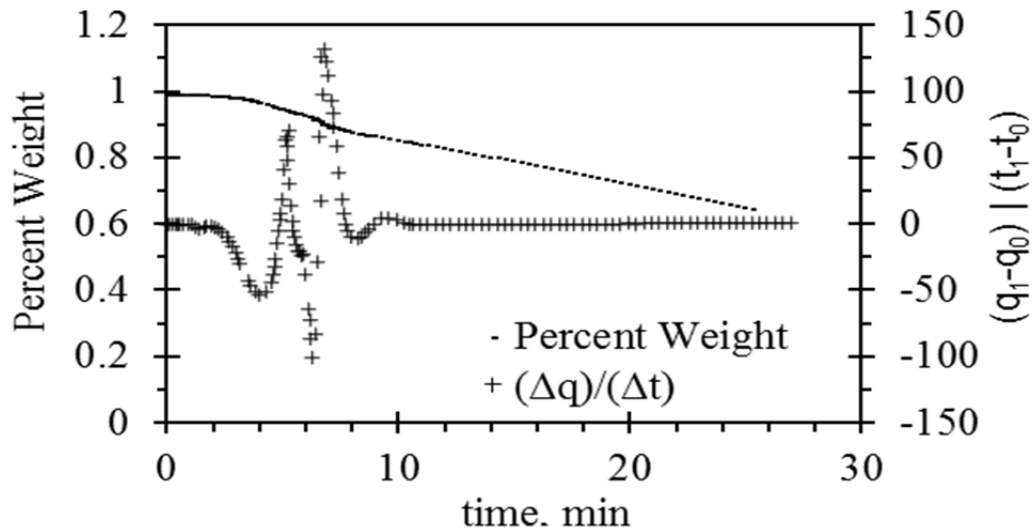


Fig. 7.24: Measured weight percent of thermogravimetric decomposition vs. change of heat flow.

The two structures appear at different levels of enthalpy of fusion and at temperatures from 420 to 430 °C. The analysis of such structures is beyond the scope of this thesis. This event is followed by a smooth curve of weight loss, indicative of CuCl evaporation.

Additional detail of composition of gases and vapour that result from a thermogravimetric decomposition can be obtained via a chromatographic analyser. The analysis in this research is based only on weight loss curves and therefore a series of stages are identified that represent characteristic phenomena of the decomposition. The stages are characterized by humidity evaporation, decomposition, and CuCl evaporation.

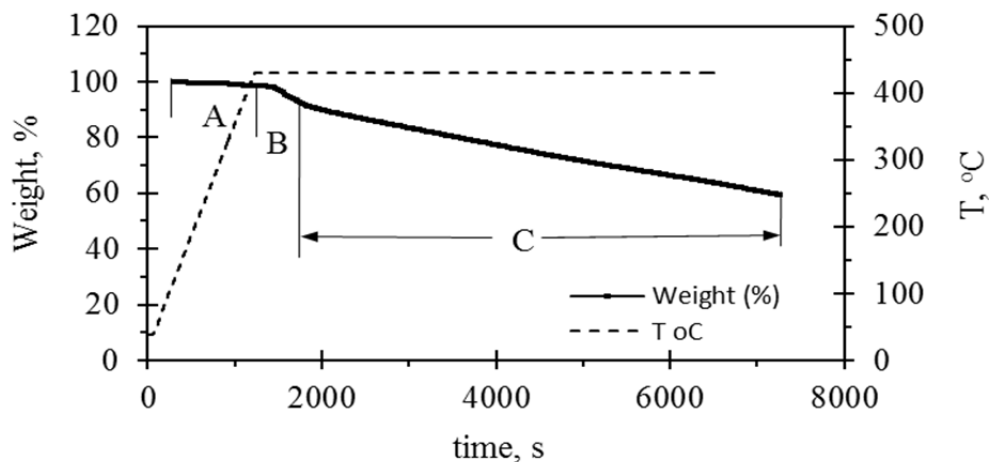


Fig. 7.25: Stages of weight losses from TGA experiments during decomposition of samples of  $\text{CuO}\cdot\text{CuCl}_2$  at  $430\text{ }^\circ\text{C}$

The TGA results were characterized by three stages as indicated in Fig 7.25. In stage A, the losses corresponded with the approximated water content of the samples. The samples of  $\text{CuO}\cdot\text{CuCl}_2$  were stored in the oven for at least 24 hours prior to the experiments. However, the highly hygroscopic properties of  $\text{CuCl}_2$  and the small size of the sample used in TGA increase the possibility of water being adsorbed during preparation of the sample before TGA experimentation. Stage B in Fig. 7.25 characterizes the fast decomposition of  $\text{CuO}\cdot\text{CuCl}_2$  with weight losses between 7 and 10% that closely corresponds with oxygen content. Finally, stage C corresponds to the evaporation of  $\text{CuCl}$ . Depending on the temperature of the experiment, when the remaining sample weight reaches between 28% and 12%, the weight losses have stopped, indicating that only non-volatile substances remain in the crucible.

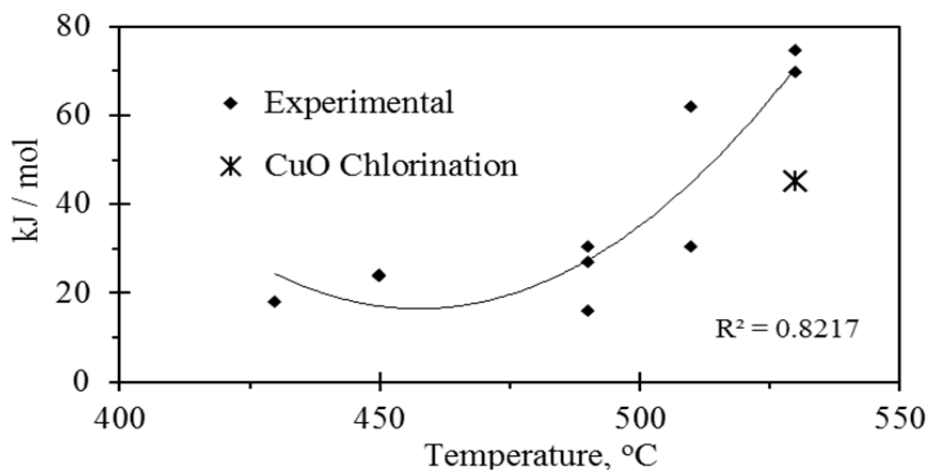


Fig. 7.26: Total experimental heat of decomposition of  $\text{CuO} \cdot \text{CuCl}_2$  and evaporation of  $\text{CuCl}$ , and energy of reaction of  $\text{CuO}$  chlorination as reported by Serban et al. [59]

Unless a chromatographic analyser is used in conjunction with TGA, the results of experiments can only be analysed in view of the weight change. Also, the isothermal conditions, and variations of heat flow provide indication of the phenomena. Fig. 7.26 indicates the heat adsorbed by the sample during the decomposition in stage B as shown in Fig. 7.25. The energy of reaction of the endothermic decomposition of  $\text{CuO} \cdot \text{CuCl}_2$  was estimated using the Arrhenius equation at 25 kJ/mol. Also, Serban et al. [59] experimented with chlorination of  $\text{CuO}$  and obtained a value for the energy of reaction at 45 kJ/mol. The total energy values shown in Fig. 7.24 are the result of the heat of reaction and heat of evaporation of  $\text{CuCl}$ . The values fall within the range of 19 kJ/mol and 69 kJ/mol, indicating agreement with previous research.

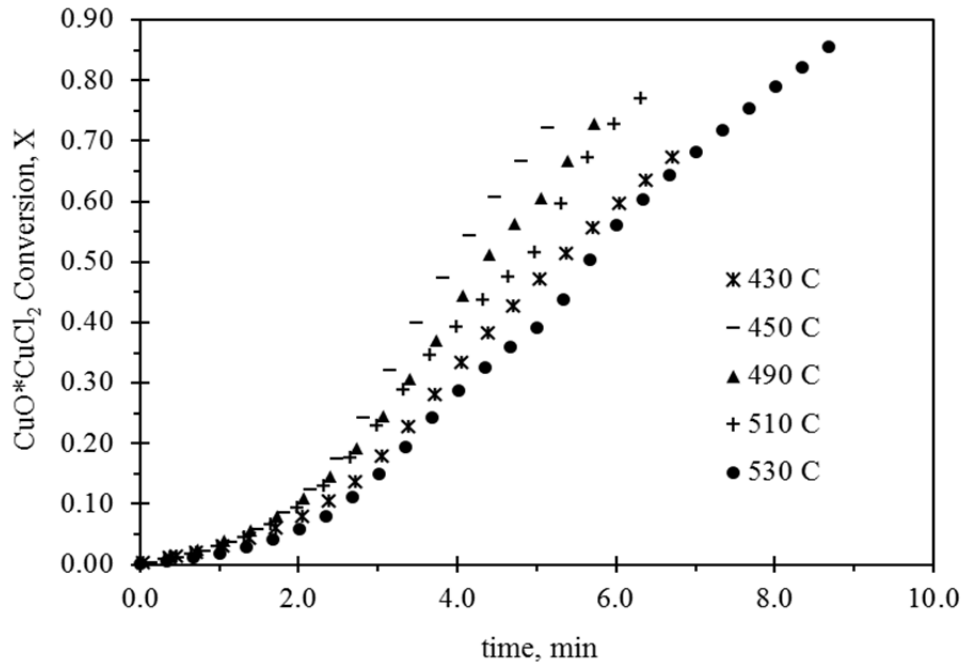


Fig. 7.27: Comparison of thermogravimetric decomposition of  $\text{CuO} \cdot \text{CuCl}_2$  at several temperatures

The thermogravimetric data corresponding to stage B in Fig. 7.25 is presented in detail for decomposition at several temperatures in Fig. 7.27. At high temperatures, the decomposition continues for a longer time to attain higher conversions. This is presumably one reason for the overall lower rate of decomposition at high temperature. Another possible reason is the increased presence of oxygen gas in the molten salt that inhibits the transport of heat. Except for decomposition at 430 °C, the overall rate of decomposition seems to be lower at higher temperatures, with a higher total conversion as the temperature is increased.

The non-volatiles are presumed to be un-reacted CuO (copper oxide). This occurs because solid CuO changes phase at 1326 °C and evaporates at 2000 °C. Experiments

conducted by Nixon et al. [43] indicated that O<sub>2</sub> is consumed by the products of decomposition to form CuO at higher temperatures and confirm the validity of this assumption. This possibility is also explained based on the mechanistic analysis of two parallel and competing reactions during decomposition as indicated in Eqns. (4.17) and (4.18). Serban et al. [59] measured the kinetics of the reaction between Cl<sub>2</sub> and CuO, and estimated the rates of reaction at four different temperatures of 480, 490, 500 and 515°C. The rate of reaction obtained for the reaction in Eq. (4.17) is a function of partial pressure of Cl<sub>2</sub> and O<sub>2</sub>, referring to the weight of CuO in the reactants.



The rate of reaction equation was applied to the volumes of reactants in the TGA experiments. Based on the results, given similar volumes of CuO, the decomposition of CuO\*CuCl<sub>2</sub> is slower than the reaction of CuO and Cl<sub>2</sub>. This can be observed from Fig. 7.28 where the rates of reaction are plotted at different temperatures. This also implies that the overall rate of reaction for CuO\*CuCl<sub>2</sub> decomposition is strongly impacted by the decomposition of CuCl<sub>2</sub>, which becomes the controlling reaction. Further experimental results by Marin et al. [44] confirmed the existence of at least two pathways for the decomposition reaction, with remaining CuO a result of incomplete CuCl<sub>2</sub> decomposition.

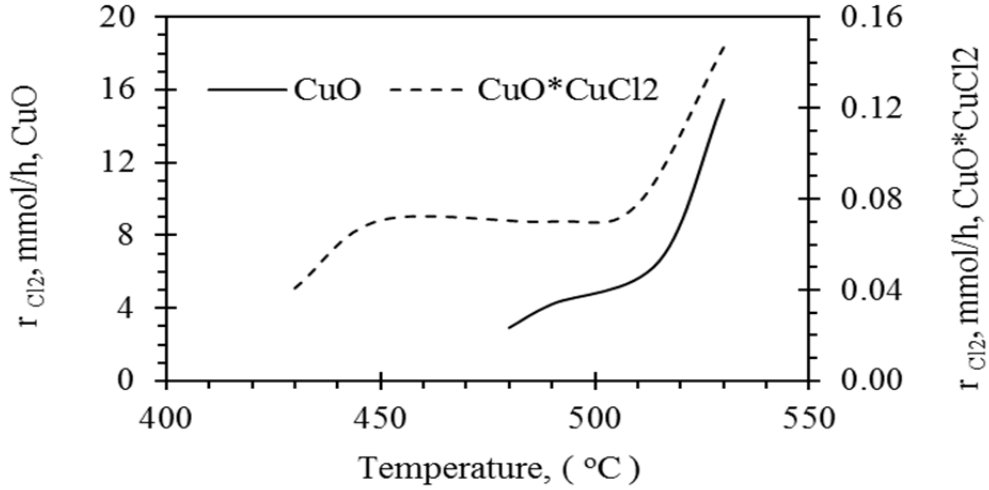
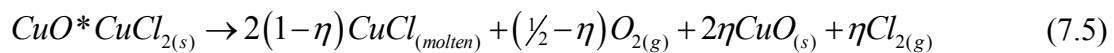


Fig. 7.28: Rate of reaction of CuO and Cl<sub>2</sub> vs. rate of release of Cl<sub>2</sub> from CuO\*CuCl<sub>2</sub>  
(TGA experiments [44, 55])

Readings from experiments at 450 °C, 490 °C, 510 °C and 530 °C resulted in the remaining weights of CuO of 26%, 24%, 24% and 15.1% of the initial sample, respectively. By performing a mass balance using the above mechanistic approach, the mol ratio of un-reacted CuO resulting from thermogravimetric experiments can be calculated based on the stoichiometric equation as follows:



With consideration of incomplete decomposition and residual reactants, the reaction is described by the following expression:



where the coefficient  $\eta < 0.5$  is the molar percent of residual CuO within the temperature range of experiments. The conversion rate of CuO\*CuCl<sub>2</sub> can then be calculated with

reference to un-reacted CuO. The weight losses in the decomposition and phase change at different temperatures are presented in Table 7.2. The initial weight losses during decomposition have a similar order to the theoretical oxygen content of 7.5%, with higher losses at higher temperatures, indicating a mixed loss of weight due to simultaneous CuCl evaporation. It can be assumed that the differences of weight losses are the result of Cl<sub>2</sub> and CuCl vapor exiting with the carrier gas argon or nitrogen. As the temperature of decomposition increases, the percent weight losses increase. With the partial pressure of CuCl vapour increasing exponentially beyond 430 °C, it is expected that weight losses are a result of O<sub>2</sub> and Cl<sub>2</sub> gas production and CuCl vaporization.

Table 7.2: Weight losses measured in TGA experiments

T (°C)	% weight phase change	% weight un-reacted CuO	Conversion CuO*CuCl <sub>2</sub> (average)
430	9.5%	24.0%	70.1%
450	9.0%	26.0%	74.0%
490	15.6%	24.0%	74.5%
510	16.0%	24.0%	76.5%
530	20.1%	15.1%	85.0%

Experiments in the batch reactor used an average of 0.3 moles of well mixed and dehydrated CuO\*CuCl<sub>2</sub>. The experiments were performed at temperatures of 470, 490, 510 and 530 °C. Prior to the experiment, the sample was heated in an oven for over 24 hours at 160 °C. Once placed in the reactor, the sample was heated to 200 °C and maintained at isothermal conditions for 10 minutes. The furnace was then set to the desired experimental temperature and measurements were started. Oxygen was first detected once temperatures of 420 to 430 °C were reached. To prevent further CuCl evaporation, heating was stopped and the carrier gas flow increased to cool down the

sample as soon as oxygen measurements fell below detectable levels. The weight losses were in the range of 8 to 10 %. Compared to the TGA experiments, the weight losses in the reactor were minimized and maintained within the time of detectable oxygen measurements. This approach provided an additional perspective in understanding the processes of the decomposition reaction.

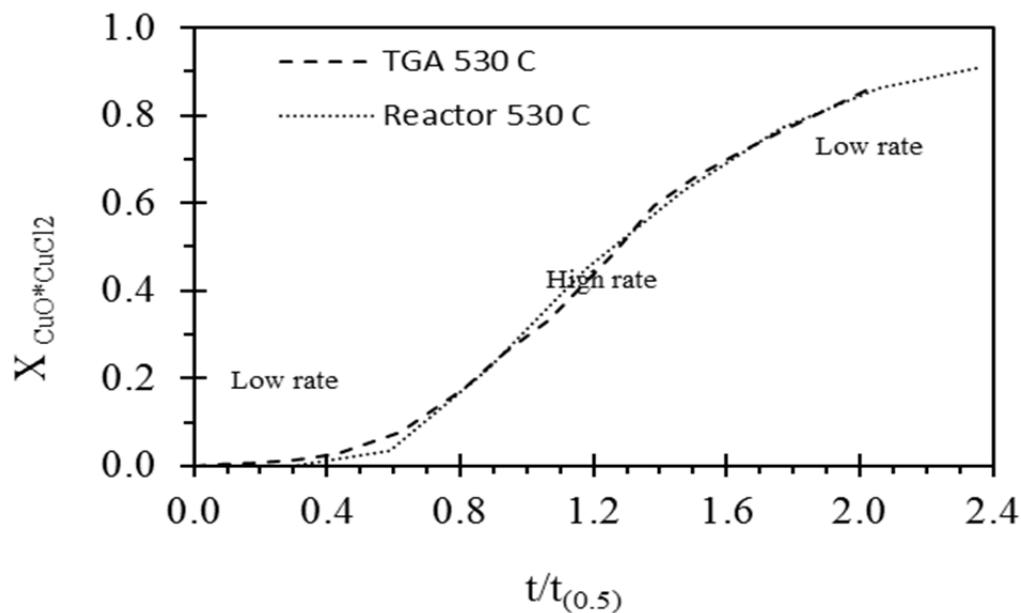


Fig. 7.29: Reduced time plot of decomposition rates of  $\text{CuO} \cdot \text{CuCl}_2$  at 530 °C (TGA and batch reactor experiments)

The decomposition of copper oxychloride is characterized by a slow rate at the beginning, followed by a high decomposition rate and then a slow rate again as shown in Fig. 7.29. In the analysis, the entire sample is assumed to be at a uniform temperature, so that the comparison of results at different temperatures illustrates the impact of heat transport on the rate of reaction. Time plots using experimental conversion data were

constructed and compared graphically between the high and low heat transfer situations (i.e., TGA and batch reactor experiments). The curves for high heat transfer (TGA situation) and the low heat transfer situation (batch reactor) are superimposed in Fig. 7.29, where some deviation is found at higher  $t/t_{0.5}$  values. Disregarding the nonlinear portion in the figure, the slope in the linear portion resulted in a value for  $k_1$  of approximately 1.098.

Fitting of the experimental data of conversion against time indicated that the best linear correlation was provided by the Avrami-Erofeev equation as shown in Fig. 7.30.

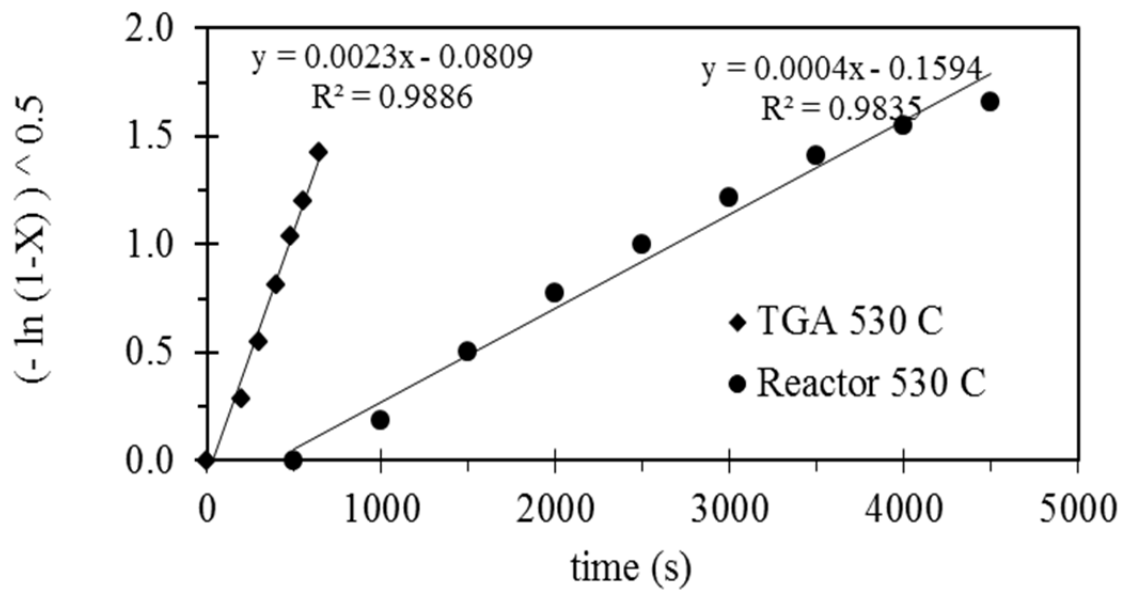


Fig. 7.30: Curve fitting of experimental data from conversion of  $\text{CuO} \cdot \text{CuCl}_2$  vs. time

The figures show a correlation of the experimental data for conversion of  $\text{CuO} \cdot \text{CuCl}_2$  vs. time, with an error of  $\pm 3.6\%$  and  $1.5\%$  for TGA and reactor experiments, respectively. The value  $k_1$  in Eq. (4.17) is validated by direct comparison with the conversion data of experiments in Table 7.3. The comparison indicates that the values of  $k_1$  deviate from the original value calculated at  $530^\circ\text{C}$  as the temperature of the

experiment decreases. The alternative to an Arrhenius relationship directly from data fitting to a non-isothermal model is difficult for this system. This observation suggests the need for a temperature dependent term as indicated in Eq. (4.17). The effect is more evident in the case of experiments performed in the reactor where heat transfer resistances are higher. The temperature dependence of decomposition of  $\text{CuO} \cdot \text{CuCl}_2$  according to Arrhenius' law is illustrated in Fig. 7.31.

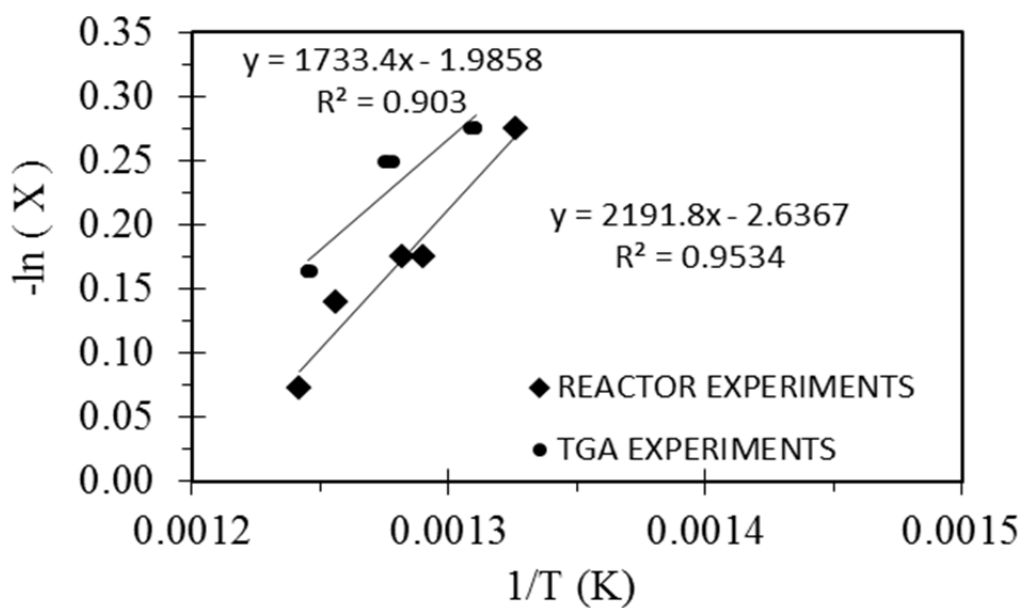


Fig. 7.31: Curve fitting of conversion data at different temperatures

The curves show the dependence of conversion versus temperature for experiments performed in the reactor and the thermogravimetric microbalance analyzer. Data from experiments at the same temperature was averaged in order to facilitate the analysis.

Table 7.3: Deviation of conversion dependent terms with temperature ( $k_1$ )

TGA Experiments					Reactor Experiments				
T (°C)	t(s)	X	$k_1$	Deviation	T (°C)	t(s)	X	$k_1$	Deviation
530	596	0.85	0.0023	-0.6%	532	4426	0.93	0.00037	7.9%
510	535	0.77	0.0022	2.2%	523	5552	0.87	0.00026	35.7%
490	538	0.75	0.0022	5.5%	507	5204	0.84	0.00026	35.0%
450	572	0.74	0.0020	11.8%	502	3777	0.84	0.00036	10.4%
430	682	0.70	0.0016	30.0%	481	4723	0.76	0.00025	36.8%
					469	6150	0.74	0.00019	52.8%

#### 7.4 Phase Change Decomposition

A comparison between the decomposition rate that results from an analysis of experiments and a theoretical phase change model provides an indication of the overall resistances that impact the conversion. Based on the phase change model (Stefan problem) and thermo-physical properties reported in Table 7.4, sample solutions of the phase interface movement are plotted at various times in Fig. 7.32. The results indicate the position of the interface for several Stefan numbers. Also, the position of the interface for a Stefan number of 2.0 is depicted based on a solution of the Stefan problem for spherical coordinates presented by Dewynne and Hill [69]. Reasonable agreement is achieved, to provide useful validation of the predictive model. At higher temperatures, the Stefan number is lower and the interface moves faster, resulting in an almost linear correlation of radius vs. time. At lower temperatures and larger Stefan numbers, the movement of the interface is slower and the radius reduces in an asymptotic manner.

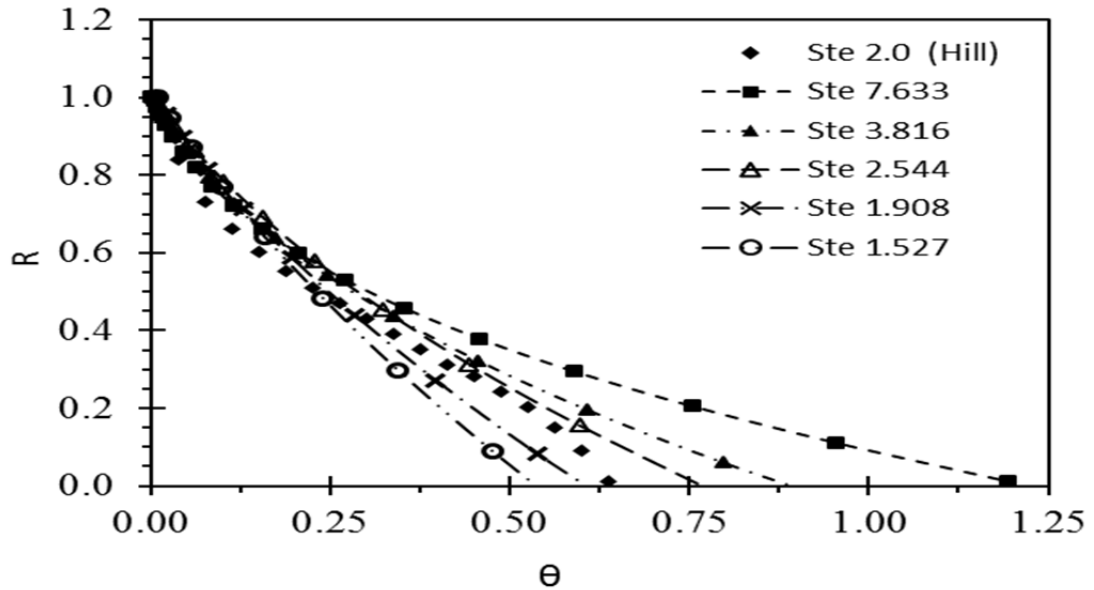


Fig. 7.32: Solid-liquid interface tracking for several Stefan numbers

At high Stefan numbers, the phase change model implies that the latent heat is the dominant thermal factor, and the shape of the curve is impacted by the ratio of latent to sensible heat of the system.

Tracking of the interface with the reaction kinetics and phase change model can be used to provide the ratio of the remaining solid to liquid mass and conversion rate for a coupled process. That rate is substantially higher than the conversion rate result of experimental measurements from calculations using the rate of reaction in Eq. (4.37). It is expected that the thermal resistance increases as the size of the sample becomes larger. By inserting the conversion and time values obtained through the phase change model into Eq. (4.37) at different Stefan numbers, the results indicated that the particle decomposes at a rate that is inversely proportional to the characteristic length. The phase change model indicates a trend to higher reaction rates at low Stefan numbers (high temperatures) and

higher thermal resistances at lower temperatures (high Stefan numbers). Similarly, the experimental data indicated that the high heat flux experimental data from TGA analysis yields higher decomposition rates. The analysis suggests a decomposition reaction limited by conduction heating of the sample. Slow heat transfer to the sample surface occurs due to the conduction resistance in the liquid and solid phases. The conduction heating is further hindered by the formation of gaseous oxygen at the interface and gas diffusion in the liquid phase. Using the values in Eq. (4.37) resulted in the curve of phase change in Fig. 7.33, where the characteristic lengths have been calculated based on spherical shapes.

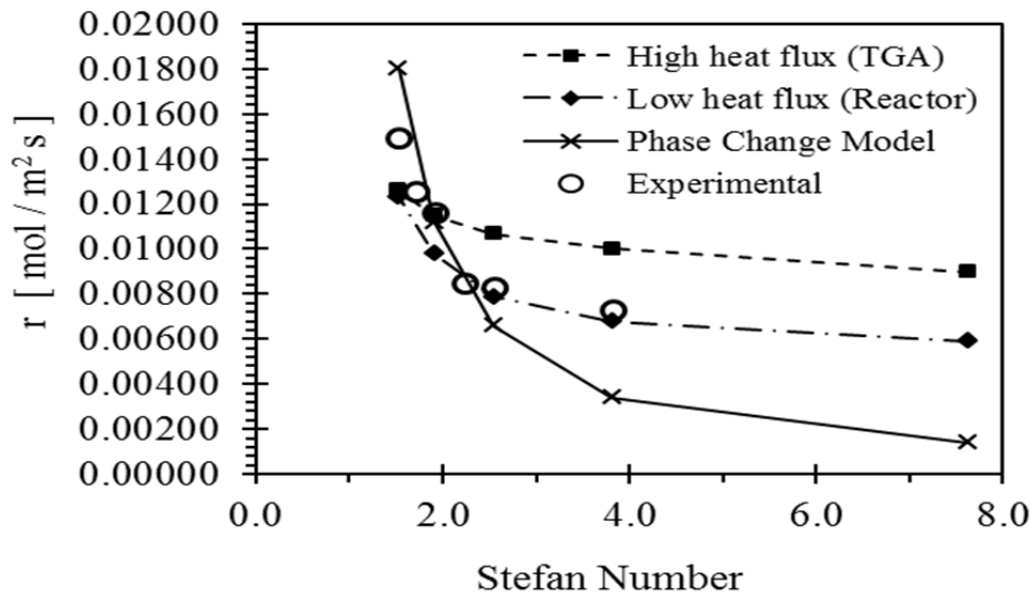


Fig. 7.33: Rates of reaction compared to experimental data

These results suggest a strong dependence of reaction kinetics on the dynamically varying shape and exposed surface area of the sample as indicated by the characteristic time, which indicates the importance of heat transfer area for both conduction and phase change.

The results indicate good agreement between the experimental results from the reactor and the low heat flux modeling. As expected, the predicted rates are higher for a typical environment of small analyzers (TGA) due to the high heat flux. The corrected model for reaction kinetics and phase change predicts an almost exponential increase of the rate with temperature increase beyond 530 °C. However, the thermodynamic analysis and experiments indicate a maximum conversion is achieved at this temperature; and operation beyond 530 °C is also not favoured in practice by an exponential increase of the vapour pressure of CuCl. Further details of rate values are shown in Table 7.4 with consideration for different temperatures. As indicated from Table 7.4 and Fig. 7.33, the rate of reaction is higher for a high heat flux reactor such as TGA when compared at the same Stefan number with a low flux reactor.

Table 7.4: Conversion rates at different temperatures

Stefan number	T [°C]	Experimental	Modeled values, $r$ [ $mol/m^2.s$ ]		
			Phase change model	High heat flux (TGA)	Low heat flux (Reactor)
1.527	530	$1.5 \times 10^{-2}$	$1.8 \times 10^{-2}$	$2.0 \times 10^{-2}$	$1.2 \times 10^{-2}$
1.717	523	$1.3 \times 10^{-2}$			
1.908	510	$1.2 \times 10^{-2}$	$1.1 \times 10^{-2}$	$1.5 \times 10^{-2}$	$9.8 \times 10^{-3}$
2.226	502	$8.5 \times 10^{-3}$			
2.544	490	$8.3 \times 10^{-3}$	$6.6 \times 10^{-3}$	$1.3 \times 10^{-2}$	$7.9 \times 10^{-3}$
3.816	470	$7.3 \times 10^{-3}$	$3.4 \times 10^{-3}$	$1.2 \times 10^{-2}$	$6.8 \times 10^{-3}$

This effect is expected given the dependence of the decomposition reaction on temperature. The phase change model is characterized by higher reaction rates at low Stefan numbers (high temperatures). Also, Fig. 7.32 indicates the presence of a higher thermal resistance at lower temperatures (higher Stefan numbers). The rate values are

approximately one order of magnitude higher at 530 °C when compared to values at lower temperatures. This observation was confirmed by the experimental data.

## 7.5 Reactor Dynamics

A dimensionless number that arises in the analysis of chemical reactions is the Damkohler number. It has a physical interpretation in terms of diffusion, rate of reaction and characteristic time of the system. It is also an indication of the residence time involving the ratio of fluid motion versus characteristic reaction time, with large Damkohler numbers associated more closely with irreversible reactions. The analysis is applicable to solid particles under chemical decomposition that leads to gas and liquid products. An additional complexity in the decomposition is that the sample may be entering the reactor contaminated with products of an incomplete upstream hydrolysis reaction such as CuCl, H<sub>2</sub>O and CuCl<sub>2</sub>. This thesis analyzes the decomposition of pure CuO\*CuCl<sub>2</sub> particles based on theoretical and experimental results that did not account for impurities. The analysis did not extend to the impact of impurities on the yield of decomposition, therefore the results must be used with care in terms of the effect that the presence of side products/reagents may have on the overall extent of reaction.

Numerical predictions of the rate of shrinkage and evolution of temperature with time are shown in Fig. 7.34 for two different initial diameters of the particle. For a maximum conversion of 90%, decomposition of the smaller particle essentially stops before reaching a temperature of  $\theta \approx 0.02$ . With larger particles of 0.6 mm in diameter, the decomposition rate approaches zero at approximately one tenth of  $r$ , while the solid temperature  $\theta$  reaches 0.21. A larger particle size impacts the overall decomposition rate

due to a larger time needed to achieve equilibrium as indicated from the figure, with a dimensionless time of 0.11, compared to 0.07 for a 0.2 mm particle. The inflection of the radius curve indicates a slower heated solid due to heat inhibited from reaching the particle by the high rate of gas generation. As more gas is generated, more heat is removed from the reaction zone and less heat is conducted towards the solid by the liquid phase due to agglomeration of bubbles, as well as a lower bulk density surrounding the particle that results in heat transfer from the solid to the endothermic reaction zone.

Figure 7.35 indicates the impact that the average liquid temperature has on the dynamics of the reaction where a lower average liquid temperature results in a slower rate of change in the Damkohler number. This confirms an effect previously observed in experimental work reported by Marin et al. [44] with small  $\text{CuO} \cdot \text{CuCl}_2$  samples.

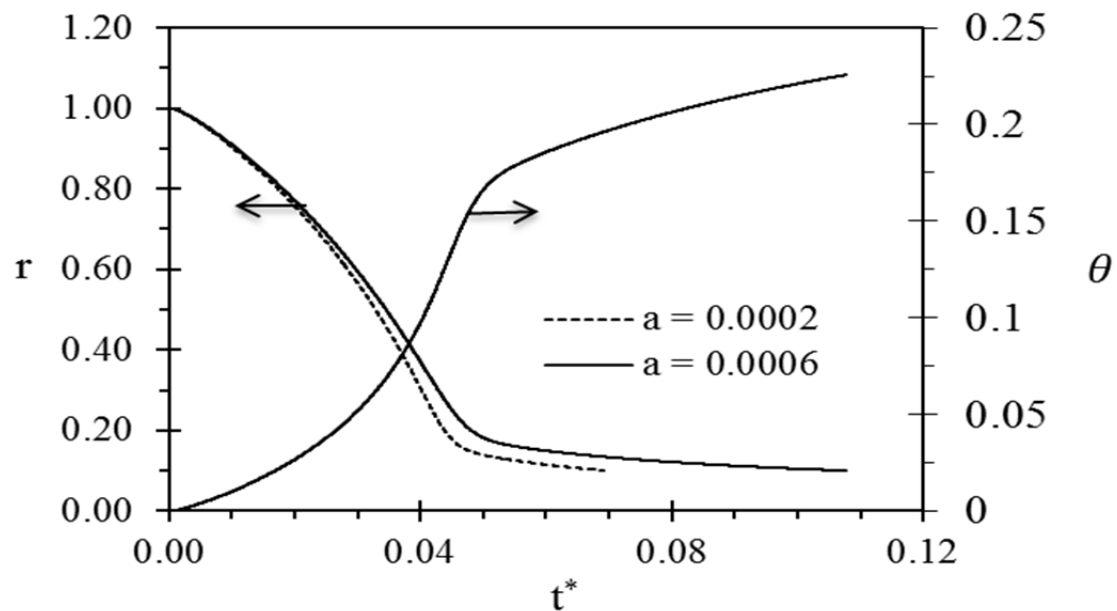


Fig. 7.34: Solid particle shrinking radius and temperature profile for several initial diameters

The decomposition is relatively fast when the low end of the temperature range is reached and the rate continues to increase as the temperature rises. The relation between the Damkohler number and the total time of reaction, however, indicated that high rates of decomposition are maintained for a short time, with most of the decomposition occurring in the range of  $Da \approx 1$ . The inflection of the curve confirms the phenomena of a slower heated solid which affects the dynamics of the reaction before reaching equilibrium.

The effect can be observed in experimental decomposition of  $\text{CuO} \cdot \text{CuCl}_2$ , where the rate of oxygen generation diminishes in an asymptotic manner towards the end of the decomposition in the reactor. This effect occurs from competing processes of heat and mass transfer due to gas diffusion away from the reaction zone.

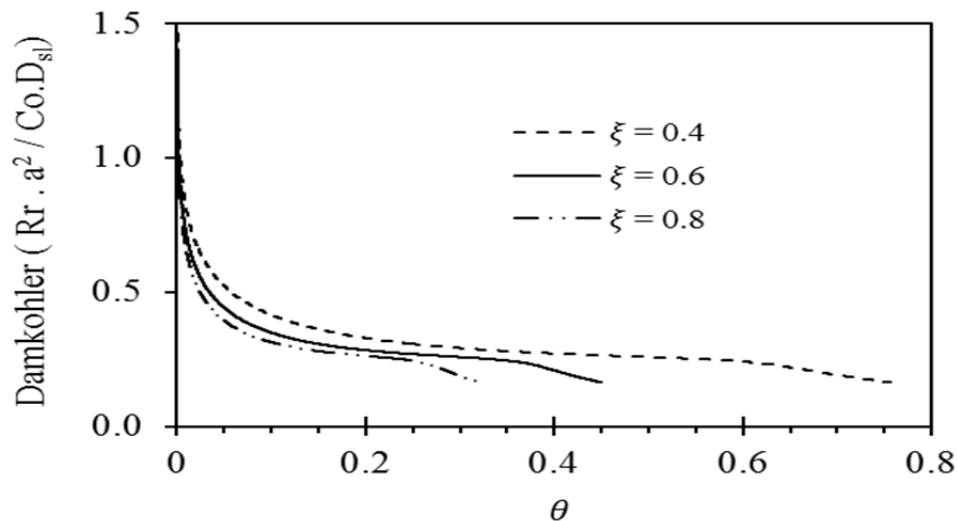


Fig. 7.35: Impact of liquid temperature on the dynamics of decomposition for 0.5 mm particles

The typical behaviour of gas evolution from the decomposition of small samples of  $\text{CuO} \cdot \text{CuCl}_2$  in Fig. 7.1 indicated that the amount of released gas increases in an

exponential manner to reach a plateau and then decreases asymptotically. This behaviour confirms the prior observations where a large Da number rapidly decreases to values below 1. The experimental results indicated a dependence of the reaction rate on concentration, as indicated by the correlation in Fig. 7.30 and represented by the Avrami-Erofeev linear regression for the average temperature of 530 °C.

The rate of decomposition varies at lower temperatures. A separate correlation was used for the reaction rate based on the Arrhenius equation as indicated in Fig. 7.31. The overall decomposition in batch operation takes longer and results in higher conversion of  $\text{CuO} \cdot \text{CuCl}_2$  at higher average molten CuCl temperatures. This effect is observed from experimental results in Fig. 7.27. At different temperatures of the molten salt, the model projected lower rates of decomposition for high temperatures as indicated in Fig 7.36.

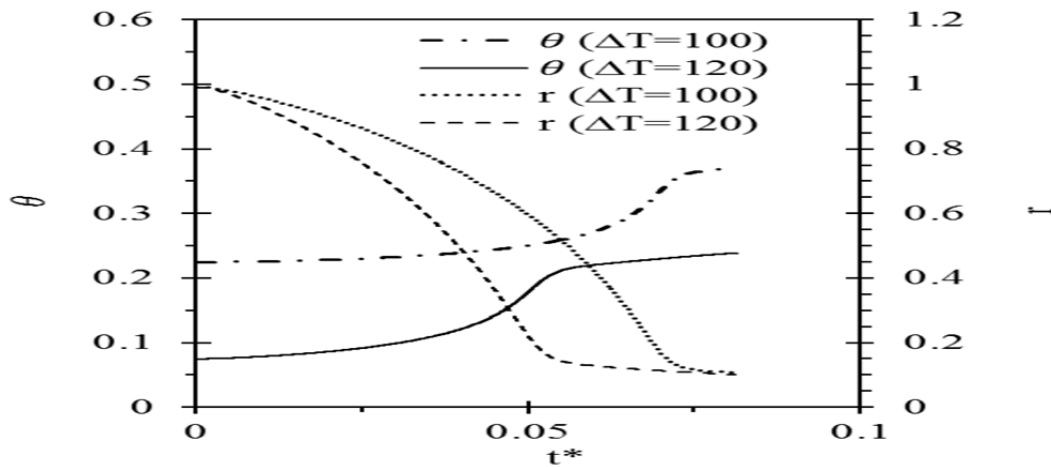


Fig. 7.36: Sensitivity to the differential of initial temperature of the solid particle and the molten continuum.

A larger temperature differential results in a higher heat flux into the particle, and faster decomposition. However, the total conversion is still lower than a smaller temperature differential. This sensitivity explains the behaviour discussed in relation to experimental results as indicated in Fig. 7.27.

A lumped capacitance model was used. These considerations were applied to the model of chemical decomposition and resulted in a rate of decomposition very sensitive to the initial temperature of the particle. When the size of the particle is too small, the dynamic of decomposition is impacted by the temperature differential between the particle and continuum as indicated in Fig. 7.37. The Damkohler number is lower for a larger temperature differential but the dynamics are equal at the extremes of the process of decomposition. First, as the particle enters the molten bath, the increase in temperature of the particle is relatively slow since the dynamics of the reaction decays asymptotically. The resistance imposed by the oxygen bubbles impacts the heat transport from the beginning. Towards the end of the decomposition, the dynamics are similar for both temperature differentials, presumably because the temperature of the particles is closer to the temperature of the molten continuum. Assuming the same conversion at the end of decomposition, the phenomenon takes longer for the lower temperature differential.

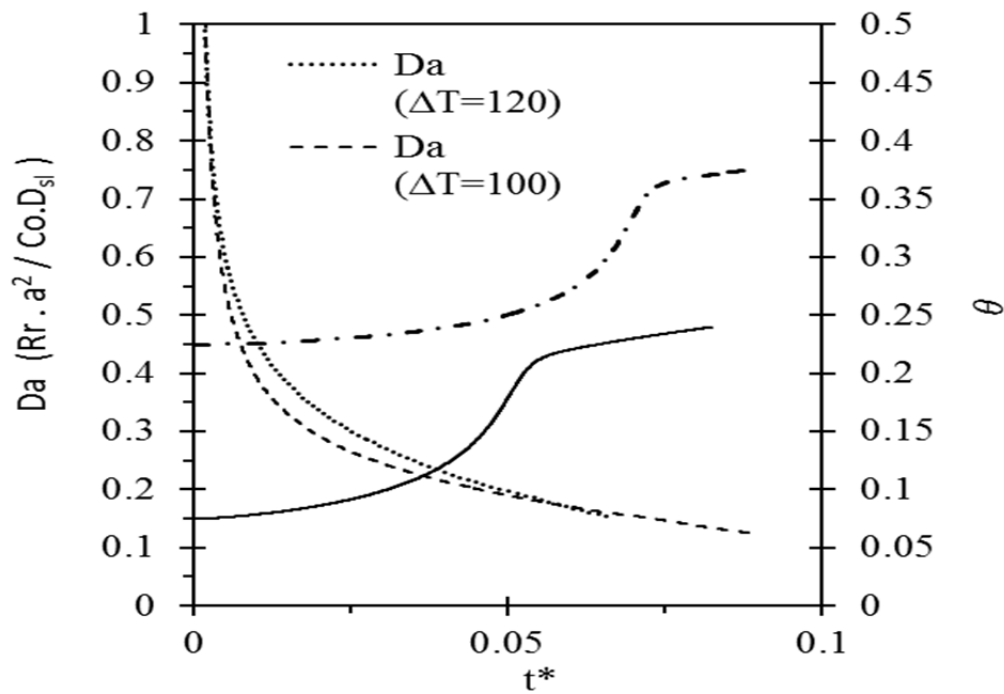


Fig. 7.37: Effects of the difference of temperature between the particle and the continuum on the dynamics of decomposition.

The decomposition in all cases started at Damkohler numbers close to 1 and rapidly decayed as indicated in Fig. 7.38. This is an indication of rapid chemical decomposition and a reaction driven process, impacted also by the slower rate of heat and mass transfer at the interface. After the reaction occurs with the Damkohler number falling below 1, the concentration of solids reduces rapidly with the Damkohler number over a long period of time. A curve of  $Da$  vs.  $t^*$  indicated that at least 95% of the decomposition occurs at or below  $Da \approx 1$ . At the inflection, the curve also indicates that full decomposition requires a longer residence time because of the particle descent. These observations suggest that equilibrium conversion can be achieved at lower temperatures. Total conversion, however, requires long residence times.

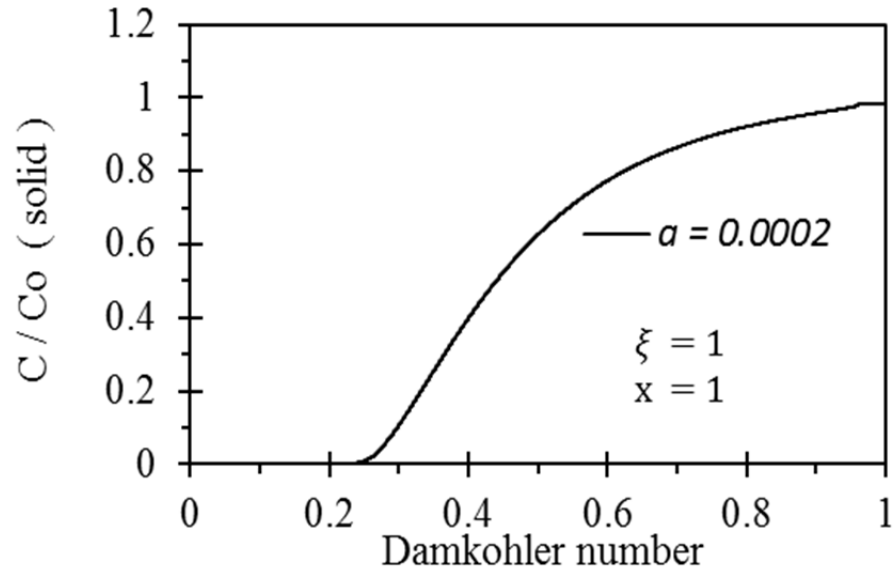


Fig. 7.38: Dynamics of reaction and concentration of solids for particles of 0.2 mm, at full conversion and average  $\xi = 1$

The predictive model shows relatively close agreement with experimental results at different average temperatures of the bulk liquid as indicated in Fig. 7.39. The curve indicates the characteristic dimensionless time of decomposition obtained from the Damkohler number. The markers in the figure indicate the normalized times of experimental decomposition at different average temperatures of molten CuCl. The experimental data has been normalized at 50% decomposition to obtain the dimensionless characteristic half-life time of the reaction, while the smooth curve represents the total dimensionless time of decomposition.

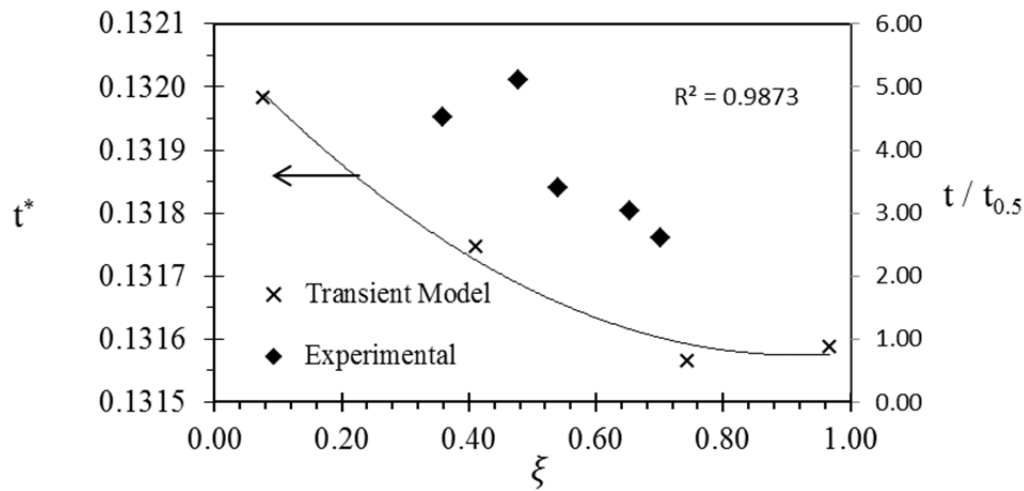


Fig. 7.39: Dimensionless residence time of decomposition of particles and experimental results of the normalized time at 50% conversion, versus average temperature of the molten medium.

Observation of the trend of the Damkohler number with time indicated that the dynamics of reaction falls in exponential manner as the particle radius is reduced. With time, the curve becomes asymptotic around values of Damkohler characteristic of reverse reactions. This behaviour is confirmed by the experimental results where the maximum conversion achieved at 530 °C is between 90 and 95%. Although the reaction dynamics are high at the beginning, it slows down as the area of contact is reduced and the relative size of gas bubbles to core particle increases, resulting in increased residence times. The predicted and experimental results have provided important data and physical insight for the design of larger scale operations of decomposition reactors that will eventually be needed when the Cu-Cl cycle is scaled up to a pilot plant.

The decomposition occurs through a succession of stages in which the heat flux towards the particle is impacted by the transport phenomenon itself. As more gas is generated, more heat is removed from the reaction zone and less heat is conducted towards the solid by the liquid phase due to agglomeration of bubbles. The bulk density of liquid surrounding the particle is lower and the overall phenomenon results in heat transfer from the solid to the endothermic reaction zone.

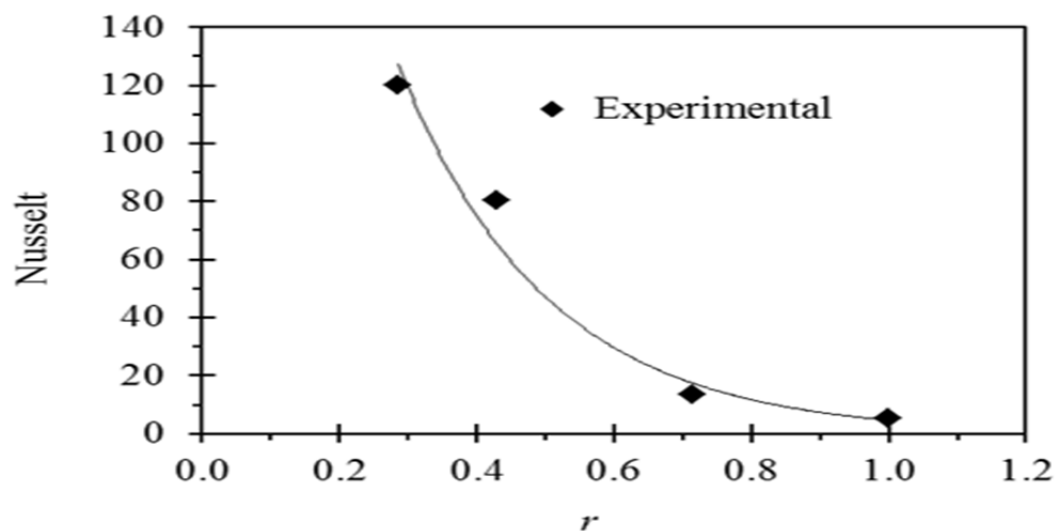


Fig. 7.40: Evolution of the overall Nusselt number as a result of varying radius of a particle of  $\text{CuO}\cdot\text{CuCl}_2$  undergoing chemical decomposition

The heat transfer occurs mainly as a result of conduction through the liquid phase. As the gas phase molar fraction increases, the liquid becomes less dense and the heat transport results from a combination of convection and conduction. This effect is indicated in Fig. 7.40 by the higher Nusselt number as the particle radius decays.

## Chapter 8 - Conclusions and Recommendations for Future Research

### 8.1 Conclusions

---

This research provided a significant improvement to the understanding of the chemical decomposition of copper oxychloride in the Cu-Cl cycle. The decomposition process is impacted by the number of particles per unit volume. The analysis indicated that the residence time increases by 60% with an increase of particle size from 0.0002 to 0.0005 m. When accounting for losses, this increase of residence time will result in a lower overall cycle efficiency. High concentration of solids promotes a higher rate of reaction but the dynamics decays faster when the concentration is above approximately 40%. Therefore, it is desirable to maintain concentrations between 20 and 40% such that the average dynamics of the reaction promotes a steady rate of decomposition. These results are useful for providing operational parameters of future scaled-up reactors.

An analysis of the chemical streams of neighboring reactions and their interactions within the Cu-Cl cycle indicated that if  $\text{CuCl}_2$  is not fully converted to  $\text{Cu}_2\text{OCl}_2$  in the hydrolysis reactor, it will release up to 0.15 moles of chlorine per mole of oxygen produced in the downstream decomposition reactor. The residual  $\text{CuCl}_2$  in the oxygen production reactor will enter the electrolytic reaction, causing a potential loss of efficiency in the electrolysis process. In addition, the processes for separation of oxygen and chlorine may require additional energy and reduce the efficiency of the Cu-Cl cycle.

The complexity of the chemical streams also influences the thermal energy integration of the Cu-Cl cycle. The decomposition reactor operates at the highest temperature of the cycle implying a potential for heat recovery. The low density of gases

at atmospheric pressure makes difficult the implementation of heat recovery strategies. As more gases exit the reactor, further heat losses occur, increasing the need for thermal energy input to the cycle, potentially reducing the overall efficiency. It was found that reducing the pressure in the reactor does not result in significant reduction of the amount of chlorine produced, although the high temperature threshold of the Cu-Cl cycle is reduced when operating at lower pressures. The results indicated that the amount of CuCl vapor in the gas stream of the oxygen production reaction is much less significant than chlorine gas. This observation is confirmed by both experimental results and analysis of molar fractions and partial pressures of chlorine and oxygen versus CuCl vapour.

Experimental results and thermodynamic analysis indicated that a reverse reaction has little probability of occurring when the molten bath is maintained at temperatures above 500 °C. Thus, the reactor should be designed in a way such that the preheating time of the solid particles is minimized as to prevent the occurrence of decomposition and a reverse reaction that may result in additional formation of CuCl<sub>2</sub> during the preheating period. This observation was confirmed by the theoretical models. Further research should be conducted to understand the impact of the presence of humidity in the reagents in the oxygen reactor. This aspect has critical importance since a portion of experimental results had to be discarded because the XRD analysis indicated the presence of Cu-hydrates. Also, the products of hydrolysis may contain some humidity that is fed to the decomposition reactor.

Thermodynamic models were designed in order to utilize data available of elementary species at standard conditions. Data was then projected to the desired

temperatures of operation by using regressions based on the specific heat of reagents and products. The data included the standard entropy, enthalpy and Gibbs free energy of formation at different temperatures. The lack of experimental calorimetric data at the high range of temperature added uncertainty to the analysis. However, the experimental results indicated the expected behavior to a reasonable extent. Analysis of the combined effects of pressure and temperature on the Gibbs free energy of the reaction indicated that the optimum operating conditions correspond to pressures in the range of 1 - 2 bars, and temperatures within 525 - 550 °C. Furthermore, a three-phase thermochemical model confirmed the experimental observation that the decomposition reaction is highly dynamic in the range of temperatures below 530 °C. However, the thermodynamic analysis indicates that the reverse reaction of CuCl and oxygen becomes spontaneous with a negative Gibbs free energy below 500 °C. Therefore, the ideal range of operation for decomposition falls between these two limits of temperature. Higher temperatures promote the evaporation of CuCl and they are not desirable. Similarly, low pressures below atmospheric disfavor the reverse reaction. Thus, at lower pressures the reactor can reduce the temperature of the decomposition. However, the thermal balance does not compensate the mechanical energy required to maintain vacuum in the reactor. Thus, within the residence time of reactants in the decomposition reactor, at temperatures above 500 °C and atmospheric pressure, it is reasonable to expect conversions in the order of 65% and higher.

The decomposition of  $\text{CuO}\cdot\text{CuCl}_2$  is an endothermic reaction coupled with phase change, mass diffusion, and heat transport by convection and conduction. The rapid dynamics of the reaction undergoes resistance by various mechanisms that include the

agglomeration of particles and the slow removal of oxygen gas from the reacting zone. A rate of reaction expression indicated a complex logarithmic relation of time and concentration of solids in the reactor in batch operation. Experiments conducted in a semi-batch environment with continuous addition of solids and continuous removal of gases indicated, as expected, that the rate of reaction is reduced as the rate of addition of solids is increased. Thus the number of solid particles available at any time with the level of energy of decomposition depends on the spatial concentration of solids, and the dispersion rate that depends on contact area between solid particles and molten CuCl. Furthermore, the contact area is reduced as oxygen evolves and creates void volumes between the liquid and the solid particles. A phase change model based on the experimental rate of reaction indicated that the overall thermal resistance is the result of a surface factor in addition to other factors. The resistances occur as a result of coupled heat and mass transfer, and chemical phenomena.

Small Reynolds and Peclet numbers imply that heat transfer in the direction of the core particle is mainly due to conduction through the liquid phase that dominates over convective phenomena. The rate of reaction is compromised with the evolution of the temperature and concentration fields as indicated by a relatively low Damkohler number. Simultaneously, the heat transfer phenomenon is hindered by the diffusion of gas away from the decomposing solid particle. Thus, the net result is a shrinking solid particle with a reduced heat flow due to the resistance imposed by a large number of gas bubbles moving away from the core.

The results of this research suggest that solid concentration has a key role in the dynamics of the reaction. It is expected that the presence of more solids results in larger area of contact and therefore more heat transferred to the reaction zone. However, with more solids present in the molten liquid, more gas is produced and more heat is removed from the reaction zone. Also, as more gas is produced, the mole fraction of liquid is reduced and a net hindering effect results in the conduction of heat through the molten species. These two effects produce a reaction system that must balance the requirement of heat for chemical decomposition and the losses of heat with the product, with a reduced capacity to transfer heat towards the particle. Therefore, in addition to maintaining a given concentration of solids according to the heat flux, it is critical to promote a well distributed dispersion of particles within the molten continuum.

The dynamics of the reaction is indicated by Damkohler numbers in the order of 10 at the beginning of the decomposition of a particle. As heat conduction is obstructed with the flow of oxygen generated, the dynamics of the reaction are reduced as indicated by a falling Damkohler number. With the Damkohler number falling asymptotically to values typical of reversibility, the residence time to achieve high conversions becomes too large for practical applications. Thus, other means are necessary to reduce the residence time while increasing conversion. It is unknown if mechanical aids such as agitation will minimize the effect that appears when the core particle radius has been reduced beyond conversion rates of 90 or 95%.

The observations provide insight for the effective design of an oxygen reactor in the thermochemical cycle of Cu-Cl for hydrogen generation. Since hydrogen must

compete with existing technologies, an efficient reactor ultimately contributes to make hydrogen more competitive.

## **8.2 Recommendations for Future Research**

The experiments of this research were conducted in TGA, batch and semi-batch experiments. It is believed that the most viable operation of the decomposition reactor for an initial scale-up of the Cu-Cl cycle will be a batch reactor. However, the experimental results indicated that the best operation resulted from a semi-batch operation with continuous addition of solids and continuous removal of oxygen. The kinetics of reaction should be researched under dynamic conditions. The experimental results in this thesis were obtained from reactors where the molten salt remained quiescent. Mechanical agitation and experiments in a continuously stirred reactor may result in better dynamics at higher Damkohler number. A reaction environment with higher Damkohler number allows also for higher concentration rates. Furthermore, the experiments were conducted with the injection of a carrying gas. The presence of a carrying gas results in lower probability of a reverse reaction occurring as oxygen is rapidly evacuated from the reaction zone. This effect confirms the predictions of Le'Chatelier phenomenon. Thus, a higher Damkohler and a reduced Le'Chatelier phenomenon may counteract each other in the desirable situation of not using a carrying gas. Experiments are recommended where oxygen is allowed to exit the reaction zone without the utilization of a carrying gas. This is a condition that is desirable for the scale-up of the cycle without the extra expense of a carrying gas.

The experiments in this research were conducted with a stoichiometric mixture of CuO-CuCl<sub>2</sub> since the mixture is a more stringent situation for testing the decomposition

reaction. Furthermore, the decomposition mechanisms indicated that at some intermediate step, the reaction is the result of competing reactions that include  $\text{CuCl}_2$  and  $\text{CuO}$  separately. It is recommended that experiments be conducted with the utilization of products of hydrolysis as they become available and that composition of products be carefully monitored via gas analysers, and XRD. Non-isothermal TGA experiments should be conducted and experiments with a variable heat flux are recommended. The results should be compared to a theoretical model of heat and mass transfer. Experiments need to be conducted to validate the observations of  $\text{CuCl}$  vapour with oxygen gas and determine the mechanisms to return the condensed matter back to the reactor bed. Finally, further measurements of chlorine gas from decomposition of hydrolysis products should provide a better understanding of the phenomenon in an integrated environment.

The dynamics of reaction indicated that the conversion of solids falls asymptotically around non-zero values, impacting the residence time in the reactor. Mechanical means of reducing this time while increasing the conversion should also be explored.

## References

---

- [1] New York State Energy Research and Development Authority (NYSERDA), February 2012, Hydrogen Fact Sheet, retrieved March 1<sup>st</sup> from <http://www.fuelcelleducation.org/wpcontent/themes/sandbox/pdf/History%20of%20Hydrogen.pdf>
- [2] BP Statistical review of world energy June 2011, retrieved Feb 2012 from <http://bp.com/statisticalreview>
- [3] BP Statistical review, Energy outlook 2030, January 2011, retrieved Feb 2012 from [http://search.babylon.com/?q=BP+Statistical+review&s=web&as=0&rlz=0&babsrc=SP\\_ss](http://search.babylon.com/?q=BP+Statistical+review&s=web&as=0&rlz=0&babsrc=SP_ss)
- [4] International Energy Agency, World Energy Outlook 2011, executive summary, retrieved Feb 2012 from [http://www.iea.org/weo/docs/weo2011/executive\\_summary.pdf](http://www.iea.org/weo/docs/weo2011/executive_summary.pdf)
- [5] M. Ball and M. Wietschel, The future of hydrogen – opportunities and challenges, International Journal of Hydrogen Energy, 34 (2009) 615-627
- [6] Air Liquide, Gas Encyclopaedia, March 2011, retrieved Feb 2012 from <http://encyclopedia.airliquide.com/encyclopedia.asp>
- [7] Hydrogen Properties, College of the Desert, Hydrogen Fuel Cells and Related Technologies, Rev 0, Dec 2001, retrieved March 2012 from

[http://www1.eere.energy.gov/hydrogenandfuelcells/tech\\_validation/pdfs/fcm01r0.pdf](http://www1.eere.energy.gov/hydrogenandfuelcells/tech_validation/pdfs/fcm01r0.pdf)

- [8] S.O. Mert, I. Dincer, Z. Ozcelik, Performance investigation of a transportation PEM fuel cell system, *International Journal of Hydrogen Energy*, 37 (2012) 623-633.
- [9] Economy and Energy No 79, Oct/Dec 2010, Ministerio da Ciencia e Tecnologia, retrieved Feb 2012 from [http://www.ecen.com/eee79/eee79e/ecen\\_79e.htm](http://www.ecen.com/eee79/eee79e/ecen_79e.htm), <http://www.ecen.com/content/eee7/motoref.htm>
- [10] M. Hooks, M. Jackson, Hydrogen and FCV implementation storyline, TIAX LLC, May 24 2007
- [11] G. Frenette, D. Forthoffer, Economic and commercial viability of hydrogen fuel cell vehicles from an automotive manufacturer perspective, *International Journal of Hydrogen Energy*, 34 (2009) 3578-3588
- [12] International Energy Agency Task 16: Hydrogen from carbon-containing materials, 2006, retrieved Feb 2012 from <http://ieahia.org/pdfs/finalreports/Task16FinalReport.pdf>
- [13] M.A. Rosen, Advances in hydrogen production by a thermochemical water decomposition: A review, *Energy Journal* 35 (2010) 1068-1076
- [14] R. Elder, R. Allen, Nuclear heat for hydrogen production: Coupling a very high/high temperature reactor to a hydrogen production plant, *Progress in Nuclear Energy*, 51 (2009) 500-525

- [15] J.C. Molburg, R.D. Doctor, Hydrogen form steam methane reforming with CO<sub>2</sub> capture, Argonne National Labs, 20<sup>th</sup> Annual International Pittsburgh Coal Conference, Sept 2003, retrieved Dec 2011 from [http://www.netl.doe.gov/technologies/hydrogen\\_clean\\_fuels/refshelf/papers/pgh/hydrogen%20from%20steam%20methane%20reforming%20for%20carbon%20dioxide%20cap.pdf](http://www.netl.doe.gov/technologies/hydrogen_clean_fuels/refshelf/papers/pgh/hydrogen%20from%20steam%20methane%20reforming%20for%20carbon%20dioxide%20cap.pdf)
- [16] P.C. Mannes, J. Yu, C. Eckert, M.L. Ghirardi, Photobiological hydrogen production prospects and challenges, American society of microbiology, June 2009, retrieved Jan 2012 from [http://www.microbemagazine.org/index.php?option=com\\_content&view=article&id=309:photobiological-hydrogen-productionprospects-and-challenges&catid=132:featured&Itemid=196](http://www.microbemagazine.org/index.php?option=com_content&view=article&id=309:photobiological-hydrogen-productionprospects-and-challenges&catid=132:featured&Itemid=196)
- [17] D. Mohan, C.U. Pittman, P.H. Steel, Pyrolysis of wood / biomass for bio – oil: A critical review, Energy and Fuels Journal, 20 (2006) 848 – 889
- [18] K. Zeng, D. Zhang, Recent progress in alkaline water electrolysis for hydrogen production and applications, Progress in Energy and Combustion Science, 36 (2010) 307 – 326
- [19] G.A. Długa, J.R. Slage, L.D. Schnidt, X.E. Verykios, Renewable hydrogen from ethanol by autothermal reforming, Science, 303 (2004) 993 – 996
- [20] P.J. de Wild, M.J. Verhaak, Catalytic production of hydrogen from methanol, Catalysis Today, 60 (2000) 3 -10

- [21] H. Watanabe, M. Otaka, Numerical simulation of coal gasification in entrained flow coal gasifier, *Fuel*, 85 (2006) 1935 – 1943
- [22] Y.H Jung, Y.H Jeong, Development of the once-through hybrid sulphur process for nuclear hydrogen production, *International Journal of Hydrogen Production*, 35 (2010) 12255 – 12267
- [23] G. Naterer, G. Suppiah S, Lewis M, Gabriel K, Dincer I, Rosen MA, et al. Recent Canadian advances in nuclear-based hydrogen production and the thermochemical Cu–Cl cycle. *Int J Hydrogen Energy*, 34 (7) (2009) 2901–2917
- [24] Z. Wang, V. N. Daggupati, G. Marin, K. Pope, Y. Xiong, E. Secnik, G. F. Naterer, K. S. Gabriel, Towards System Integration of the Cu-Cl Thermochemical Hydrogen Production Cycle, *International Conference on Hydrogen Production*, Thessaloniki, Greece, June 19-22, 2011
- [25] C.M. Stoots, J.E. O’Brien, K.G. Condie, J.J. Hartvigsen, High temperature electrolysis for large-scale hydrogen production from nuclear energy – Experimental investigations, *International Journal of Hydrogen Energy*, 35 (2010) 4861 – 4870
- [26] S.D. Ebbesen, J. Hegh, K.A. Nielsen, J.U. Nielsen, M. Mogensen, Durable solid oxide cell stack for production of Hydrogen and synthesis gas by high temperature electrolysis, *International Journal of Hydrogen Energy*, 36 (2011) 7363 – 7373
- [27] E. Broda, Utilization of solar radiation for water photolysis, *International Journal of Hydrogen Energy*, 5 (1980) 453 – 454

- [28] G.E. Beghi, A decade of research on thermochemical hydrogen at the joint research centre, Ispra, International Journal of Hydrogen Energy, 11 (12) (1986) 761 -771
- [29] L.C. Brown, G.E. Besenbruch, , R.D. Lentsch, K.R. Schultz, J.F. Funk, P.S. Pickard. A.C. Marshall, S.K. Showalter, High efficiency generation of hydrogen fuels using nuclear power, GA A23451, Final technical report prepared under the Nuclear Energy Research Initiative (NERI), San Diego, CA, 2003. Retrieved Jan 2011 from [http://www.energy.ca.gov/ab1007/documents/2007-05-31\\_joint\\_workshop/2007-05-31\\_HYDROGEN\\_FUEL\\_CELL\\_SCENARIO.PDF](http://www.energy.ca.gov/ab1007/documents/2007-05-31_joint_workshop/2007-05-31_HYDROGEN_FUEL_CELL_SCENARIO.PDF)
- [30] M.A. Lewis, J.G. Masin, P.A. O'Hare, Evaluation of alternative thermochemical cycles. Part I: The methodology, International Journal of Hydrogen Energy, 34 (9) (2009) 4115 - 4124
- [31] M.A. Lewis, J.G. Masin, P.A. O'Hare, Evaluation of alternative thermochemical cycles. Part II: The down-selection process, International Journal of Hydrogen Energy, 34 (2009) 4125-4135
- [32] M.A. Lewis, J.G. Masin, R.B. Vilim, Development of the low temperature Cu-Cl cycle. Proceedings of 2005 International congress on advances in nuclear power plants, ICAPP '05, May 15-19, 2005, Seoul, Korea, American Nuclear Society, May 2005
- [33] B. Russ, P. Pickard, S. Kung, Sulfur-Iodine thermochemical cycle, Project PD-12, 2009 DOE Hydrogen Program Review, Albuquerque, NM, USA

- [34] G.F. Naterer, M. Fowler, J. Cotton, K. Gabriel, Synergistic Roles of Off-Peak Electrolysis and Thermochemical Production of Hydrogen from Nuclear Energy in Canada, *International Journal of Hydrogen Energy*, 33 (23), (2008) 6849-6857
- [35] Hydrogen Posture Plan, an Integrated Research, Development and Demonstration Plan, United States Department of Energy, United States Department of Transportation, December 2006, from [http://www.hydrogen.energy.gov/pdfs/hydrogen\\_posture\\_plan\\_dec06.pdf](http://www.hydrogen.energy.gov/pdfs/hydrogen_posture_plan_dec06.pdf)
- [36] Z. L. Wang, G. F. Naterer, K. S. Gabriel, S. Supphia, SCWR-hydrogen plant thermal integration, paper presented at the 2<sup>nd</sup> Conference Canada-China Joint Conference on Super-Critical Water-Cooled Reactors, Nuclear Engineering International, Toronto, April 2010
- [37] G. Naterer, S. Suppiah, M. Lewis, K. Gabriel, I. Dincer, M.A. Rosen, M. Fowler, G. Rizvi, E.B. Easton, B.M. Ikeda, M.H. Kaye, L. Lu, I. Pioro, P. Spekkens, P. Tremaine, J. Mostaghimi, J. Avsec, J. Jiang, Recent Canadian advances in nuclear based hydrogen production and the thermochemical Cu-Cl cycle, *international Journal of Hydrogen Energy*, 34 (2009) 2901-2917.
- [38] Z. L. Wang, G. F. Naterer, K. S. Gabriel, R. Gravelins, V. N. Daggupati, Comparison of different copper–chlorine thermochemical cycles for hydrogen production, *International Journal of Hydrogen Energy*, 34 (2009) 3267 – 3276
- [39] G.F. Naterer, S. Suppiah, L. Stolberg, M. Lewis, Z. Wang, V. Daggupati, K. Gabriel, I. Dincer, M.A. Rosen, P. Spekkens, S.N. Lvov, M. Fowler, P. Tremaine, J. Mostaghimi, E.B. Easton, L. Trevani, G. Rizvi, B.M. Ikeda, M.H. Kaye, L. Lu, I. Pioro, W.R. Smith, E. Secnik, J. Jiang, J. Avsec, Canada's program on nuclear

- hydrogen production and the thermochemical Cu-Cl cycle, *International Journal of Hydrogen energy*, 35 (20) (2010) 10905-10926
- [40] D. Dokiya, Y. Kotera, Hybrid cycle with electrolysis using a Cu-Cl system. *International Journal of Hydrogen Energy*, 1(1976) 117-121
- [41] G.F. Naterer, V.N. Daggupati, G. Marin, K.S. Gabriel, Z.L. Wang, Thermochemical hydrogen production with a copper–chlorine cycle, II: Flashing and drying of aqueous cupric chloride, *International Journal of Hydrogen Energy*, 33 (2008) 5451-5459
- [42] Carty RH, Mazumder MM, Schreider JD, Pangborn JB. Thermochemical hydrogen production, vols. 1–4. Chicago, IL: Gas Research Institute for Gas Technology, GRI-80/0023, 1981.
- [43] A. Nixon, M. Ferrandon, M. H. Kaye, L. Trevani, Thermochemical production of hydrogen, Synthesis, characterization, and decomposition of copper oxychloride, *Journal of Thermal Analysis and Calorimetry*, Nov 2011.
- [44] G.D. Marin, Z. Wang, G.F. Naterer, K. Gabriel, By-products and reaction pathways for integration of the Cu–Cl cycle of hydrogen production, *International Journal of Hydrogen Energy*, 36 (2011) 13414-13424
- [45] G.F. Naterer, S. Suppiah, L. Stolberg, M. Lewis, M. Ferrandon, Z. Wang, I. Dincer, K. Gabriel, M.A. Rosen, E. Secnik, E.B. Easton, L. Trevani, I. Pioro, P. Tremaine, S. Lvov, J. Jiang, G. rizvi, B.M. Ikeda, L. Lu, M. Kaye, W.R. Smith, J. Mostaghimi, P. Spekkens, M. Fowler, J. Avsec, Clean hydrogen production with the Cu-Cl cycle-Progress of International consortium. I: Experimental unit

- operations, *International Journal of Hydrogen Energy*, 36 (24) (2011) 15486-15501
- [46] G.F. Naterer, S. Suppiah, L. Stolberg, M. Lewis, M. Ferrandon, Z. Wang, I. Dincer, K. Gabriel, M.A. Rosen, E. Secnik, E.B. Easton, L. Trevani, I. Pioro, P. Tremaine, S. Lvov, J. Jiang, G. rizvi, B.M. Ikeda, L. Lu, M. Kaye, W.R. Smith, J. Mostaghimi, P. Spekkens, M. Fowler, J. Avsec, Clean hydrogen production with the Cu-Cl cycle-Progress of international consortium. II: Simulations, thermochemical data and materials, *International Journal of Hydrogen Energy*, 36 (24) (2011) 15486-15501
- [47] Z. Wang, G.F. Naterer, K.S. Gabriel, E. Secnik, R. Gravelins, V. Daggupati, Thermal designs of a solar hydrogen plant with a copper-chlorine cycle and molten salt energy storage, 36 (17) (2011) 11258-11272
- [48] V.N. Daggupati, G.F. Naterer, K.S. Gabriel, R.J Gravelins, Z.L. Wang, Effects of atomization conditions and flow rates on spray drying of cupric chloride particle formation, *International Journal of Hydrogen Energy*, 36 (17) (2011) 11353-11359
- [49] L. Stolberg, H.A. Boniface, S. McMahon, Electrolysis of the CuCl/HCl system for the production of nuclear hydrogen, presented at the Fourth International Topical meeting on High temperature Reactor Technology, ASME, Sept 2008, Washington, USA
- [50] S. Ranganathan, E. B. Easton, Ceramic carbon electrode based anodes for use in the copper chlorine thermochemical cycle, *Proceedings of the International*

Conference on Hydrogen Production, May 2009, Canada, from <http://faculty.uoit.ca/easton/17018.pdf>

- [51] M. Lewis, M. Ferrandon, S. Nigoyi, S. Ahmed, C. Fan, R. Sharna, M. Fedkin, M. Hickner, S. Lvov, D. Tatterson, L. Nitsche, L. Wedgwood, Membrane / Electrolyzer development in the Cu-Cl thermochemical cycle, presented at the Hydrogen Program Annual Merit Review Meeting, Arlington VA, May 12, 2011
- [52] V.N. Daggupati, G.F. Naterer, K.S. Gabriel, R.J. Gravelsins, Z.L. Wang, Solid particle decomposition and hydrolysis reaction kinetics in Cu-Cl thermochemical hydrogen production, *International Journal of Hydrogen Energy*, 35 (2010) 4877-4882
- [53] M.S. Ferrandon, M.A. Lewis, F. Alvarez, E. Shafirovich, Hydrolysis of  $\text{CuCl}_2$  in the Cu-Cl thermochemical cycle for hydrogen production: Experimental studies using a spray reactor with an ultrasonic atomizer, *International Journal of Hydrogen Energy*, 35 (2010) 1895 – 1904
- [54] V. N. Daggupati, G. F. Naterer, K. S. Gabriel, R. J. Gravelsins, Z. L. Wang, Equilibrium conversion in Cu-Cl cycle multiphase processes of hydrogen production, *Thermochimica Acta*, 496 (2009) 117 – 123
- [55] M. L. Walter-Levy, M Goreaud, Sur la Formation des Chlorures Culvriques par Vola Seche. II.- Thermolyse des Chlorures Neutras et Basiques, *Laboratoire de Chimie Minerale de la Faculte des Sciences de Caen*, 1971, 22.7.70
- [56] M. A. Lewis, M. S. Ferrandon, D. F. Tatterson, P. Mathias, Evaluation of alternative thermochemical cycles – Part III, further development of the Cu-Cl cycle, *International Journal of Hydrogen Energy*, 34 (2009) 4136 – 4145

- [57] A. Lindbråthen, M.B. Hagg, Membrane separation of chlorine gas, *Chemical Engineering and Processing: Process Intensification*, 48 (2009) 1-16
- [58] G.F. Naterer, K. Gabriel, Z.L. Wang, V.N. Daggupati, R. Gravelins, Thermochemical hydrogen production with a copper–chlorine cycle. I: oxygen release from copper oxychloride decomposition, *International Journal of Hydrogen Energy*, 33 (2008) 5439-5450
- [59] Serban, M. A. Lewis, J. K. Basco, Kinetic Study of the Hydrogen and Oxygen Production Reactions in the Copper-Chloride Thermochemical Cycle, American Institute of Chemical Engineering, Spring National Meeting, New Orleans, LA, April 25-29, 2004
- [60] National Institute of Standards and Technology. Chemistry WebBook. NIST, February 1, 2010, retrieved Oct 2010 from <http://webbook.nist.gov/chemistry/>.
- [61] C. Lamberti, C. Prestipino, L. Capello, S. Bordiga, A. Zec, G. Spotto, S. Diaz, A. Marsella, B. Cremaschi, M. Garilli, S. Vidotto, G. Leofanti, The  $\text{CuCl}_2/\text{Al}_2\text{O}_3$  Catalyst Investigated in Interaction with Reagents, *International Journal of Molecular Science*, 2 (2001) 230-245
- [62] G.D. Marin, Z. Wang, G.F. Naterer, K. Gabriel, X-ray diffraction study of multiphase reverse reaction with molten  $\text{CuCl}$  and oxygen, *Thermochimica Acta*, 524 (2011) 109-116
- [63] P. Ramamurthy, E.A. Secco, Studies on metal hydroxyl compounds IX. Kinetics of thermal decomposition of twelve copper halides derivatives, *Canadian Journal of Chemistry* 47 (20) (1969) 3915 - 3918

- [64] A. Chatterjee and S. Chaturvedi, Heat transfer in a reaction–diffusion system with a moving heat source, *International Journal of Heat and Mass Transfer*, 54 (2011) 326-337
- [65] C. Vuik, Some historical notes on the Stefan problem. Faculty of Electrical Engineering, Mathematics and Computer Science, Delft University of Technology, Nov. 13, 2003, Delft, The Netherlands
- [66] M. N. Ozisik, *Heat Conduction*, second edition, Department of Mechanical and Aerospace Engineering, North Carolina State University, Wiley, New York, 1993
- [67] J. Caldwell, Y.Y. Kwan, Numerical methods for one-dimensional Stefan problems, *Communications in Numerical Methods Engineering*, 20 (2004) 535-545
- [68] V. Voller, M. Cross, Accurate solutions of moving boundary problems using the enthalpy method, *International Journal of Heat and Mass Transfer*, 24 (1981) 545-556
- [69] J.N Dewynne, J. Hill, *On a Multiphase Stefan Problem*, first edition, Department of Mathematics, University of Wollongong, Wollongong, Australia, May 1985
- [70] C.K. Hsieh, Exact solution of Stefan problems for a heat front moving at constant velocity in a quasi-steady state, *International Journal of Heat and Mass Transfer*, 38 (1) (1995) 71-79

- [71] O. Levenspiel (1999) Elements of Chemical Reaction Engineering, 3<sup>rd</sup> ed., Prentice Hall, New York
- [72] M. Ishida, C.Y. Wen, Comparison of kinetic and diffusional models for solid-gas reactions. American Institute of Chemical Engineering Journal, 14 (1968) 311-317
- [73] M Ishida and Wen, C. Y. (1971). Comparison of zone-reaction model and unreacted-core shrinking model in solid-gas reactions - Isothermal analysis. Chemical Engineering Science, 26, 1031-1041
- [74] M. Ishida, C.Y. Wen, T. Shirai, (1971). Comparison of zone reaction model and unreacted-core shrinking model in solid-gas reactions - II Non-isothermal analysis. Chemical Engineering Science, 26 (1971) 1043-1048
- [75] J. W. Brown, R.V. Churchill, Fourier Series and Boundary Value Problems, sixth edition, McGraw Hill, New York, 2008
- [76] D.G. Guffy, Transform Methods for Solving Partial Differential Equations, second edition, Chapman and Hall / CRC, London, 2004
- [77] F. Mosally , A.S. Wood, A. Al-Fhaid, An exponential heat balance integral method, Applied Mathematics and Computation, 130 (2002) 87-100
- [78] C.Y. Hoon, L.C. Tin, External mass transfer model for a re-circulated packed-bed batch reactor on the hydrolysis of palm olein using immobilized lipase, Proceedings of the 1<sup>st</sup> International Conference on Natural Resources Engineering & Technology 2006, Putrajaya, 24-25 July 2006, Malaysia, 500-509

- [79] E.L. Cussler, Diffusion Mass Transfer in Fluid Systems, third edition, Cambridge University Series, 2009
- [80] R. Leyva-Ramos, J. Rivera-Utrilla, N.A. Medellin Castillo, M.Sanchez-Polo, Kinetic modeling of fluoride adsorption from aqueous solution onto bone char, Chemical Engineering Journal, 158 (2010) 458-467
- [81] W.H. Cheung, J.C.Y. Ng, G. McKay, Kinetic analysis of the sorption of copper II ions on chitosan, Journal of Chemical Technology and Biotechnology, 78 (2003) 562-571
- [82] F.W. Wilburn, J.H. Sharp, The influence of heat transfer on reduced time plots, Journal of Thermal Analysis, 41 (1994) 483-492
- [83] G. Singh, P. Srivastava, J. Srivastave Kinetics of thermal decomposition of dichloroanilinium bromide salts, Journal of Thermal Analysis and Calorimetry 89 (2007) 181 - 189
- [84] G. Singh, I.P. Singh, K. Jain, M. Jain, Kinetics of thermal decomposition of Arylammonium Sulfates, Part 2: m-Ditoluidinum Sulfate, Journal of the Chemical Society Perkins Translations, 2 (1993) 1521 - 1524
- [85] M. Avrami, Kinetics of phase change I, General Theory, Journal of Chemical Physics, 7 (1939) 1103-1112
- [86] M Avrami, Kinetics of phase change. II Transformation time relations for random distribution of nuclei, Journal of Chemical Physics, 8 (1940) 212-224

- [87] R. Pfeffer, J. Happel, Analytical study of heat and mass transfer in multi-particle system at low Reynolds number, *American Institute of Chemical Engineering*, 10 (5) (1964) 605
- [88] M. Sussman, K.M. Smith, M.Y. Hussaini, M. Ohta, R. Zhi-Wei, A sharp interface method for incompressible two-phase flows, *Journal of Computational Physics*, 221 (2007) 469-505
- [89] H. Wang, Z. Zhang, Y. Yang, Z. Hui-sheng, Viscosity effects on the behaviour of a rising bubble, *Journal of Hydrodynamics*, 22 (1) (2010) 81-89
- [90] G. Bazbauers, Experimental investigation of low Damkohler number in turbulent reaction, (Master Thesis), Department of Mechanical Engineering, Massachusetts Institute of Technology, Cambridge, Massachusetts, USA. (1995)
- [91] H.S. Fogler (2011) *Essentials of chemical reaction engineering*, Prentice Hall International Series in the Physical and Chemical Engineering Sciences, Upper Saddle River, NJ
- [92] M. Doichinova, O. Lavrenteva, Chr. Boyadjiev, Non-linear mass transfer from a solid spherical particle dissolving in a viscous fluid, *International Journal of Heat and Mass Transfer*, 54 (2011), 2998-3003
- [93] R. Krishna, Mass transport from a spherical body into a multicomponent fluid stream, *Letters in Heat and Mass Transfer*, Vol. 3 (1976) 257-266.

- [94] L.W. Smith, Ross Taylor, Film models for multi-component mass transfer: A statistical comparison. *Industrial Engineering Chemistry Fundamentals*, 22 (1983) 97-104
- [95] W.J. Yang, Transient heat transfer in a thick thermal boundary layer with spherical symmetry, *Letters on Heat and Mass Transfer*, University of Michigan, 4 (1977) 75-84,
- [96] M. Cruchaga\* and D. Celentano, Numerical analysis of thermally coupled flow problems with interfaces and phase change effects, *International Journal of Computational Fluid Dynamics*, 16 (4) (2002) 247-262
- [97] G.A. Hughmark, Heat and mass transfer for spherical particles in a fluid field, *Industrial Engineering Chemical Foundations Journal*, 19 (1980) 198-201
- [98] H. Gan, J Feng, H.H. Hu, Simulation of the sedimentation of melting solid particles, *International Journal of Multiphase Flow*, 29 (2003) 751-769
- [99] H. Gan, J. Chang, J. Feng, H.H. Hu, Direct numerical simulation of solid particles with thermal convection, *Journal of Fluid Mechanics*, 481 (2003) 385-411
- [100] F. Grevrin, O. Masbernat, Numerical study of solid-liquid fluidization dynamics, *American Institute of Chemical Engineering Journal*, 56 (11) (2010)
- [101] T.V. Thelen, W.F. Ramirez, Modeling of solid-liquid fluidization in the stokes flow regime using two phase flow theory, *American Institute of Chemical Engineering Journal*, 45 (4) (1999) 708-723

- [102] M. Zastawny, G. Mallouppas, F. Zhao, B. van Wachem, Derivation of drag and lift force and torque coefficients for non-spherical particles in flows, *International Journal of Multiphase Flow*, in press, (2011)
- [103] J Happel, Viscous flow in multiparticle systems: Slow motion of fluids relative to beds of spherical particles, *American Institute of Chemical Engineering Journal*, 4 (2) (1958) 197-201
- [104] P.A. Nelson, T.R. Galloway Particle to fluid heat and mass transfer in dense systems of fine particles, *Chemical Engineering Science*, 30 (1975) 1-6
- [105] G. F. Froment, K. B Bischoff, J. De Wilde (2011) 3<sup>rd</sup> ed., *Chemical reactor analysis and design*, John Wiley and Sons, New York
- [106] M.C. Ruzicka, Review on dimensionless numbers, *Chemical Engineering Research and Design Journal*, 86 (2008) 835–868
- [107] G. Astarita, Dimensional analysis, scaling, and orders of magnitude, *Chemical Engineering Science*, 52 (24 (1997) 4681 - 4698
- [108] R.P.W. Scott, *Physical Chemistry Resources*, Book 5, Thermal Analysis, (on line) retrieved Sept. 2011 from [http://physicalchemistryresources.com/Book5\\_Thermal\\_Analysis.pdf](http://physicalchemistryresources.com/Book5_Thermal_Analysis.pdf)
- [109] R.J. Moffat, Some experimental methods for heat transfer studies, *Experimental Thermal and Fluid Science*, 3 (1990) 14 - 32

- [110] Kline, S. J., and F. A. McClintock, "Describing Uncertainties in Single-Sample Experiments," *Mechanical Engineering*, 75 (1) (1953)
- [111] T Parry, *Thermodynamics and Magnetism of Cu<sub>2</sub>OCl<sub>2</sub>*, Department of Chemistry and Biochemistry, Brigham Young University, 2008, Provo, Utah, USA
- [112] G.A. Slack, P. Anderson, Pressure and temperature effects on thermal conductivity of CuCl, *American Physics Society, Physical Review B*, 26 (4) (1982)
- [113] *Introduction to X-ray Diffraction*. PANalytical Speciris, 2010, Panalytical B.V., Almelo, The Netherlands
- [114] J. Leroux, D.H. Lennox, K. Kay. Direct Quantitative X-Ray Analysis by Diffraction-Absorption Techniques, *Journal of Analytical Chemistry*, 25 (1953) 740-743.
- [115] W.T. Vetterling, S.A. Teukolsky, W.H. Press, B.P. Flannery, *Numerical Recipes in C: The art of scientific computing* (1992) Cambridge University Press, 2<sup>nd</sup> ed., New York
- [116] Cash, J.R., and Karp, A.H. 1990, *ACM Transactions on Mathematical Software*, 16 (2) (1990) 201–222
- [117] S.V. Krivovichev, S.K. Filatov, The cuprite-like framework of OCu<sub>4</sub> tetrahedra in the crystal structure of synthetic melanothallite, Cu<sub>2</sub>OCl<sub>2</sub> and its negative thermal expansion, *The Canadian Mineralogist*, 40 (2002) 1185-1190
- [118] L. Brewer, N. L. Lofgren, The Thermodynamics of Gaseous Cuprous Chloride, Monomer and Trimer, *Journal of the American Chemical Society*, 72 (1950) 3038

- [119] S. Mizuno, K. Nakayama, T. Kawachi, Y. Kojima, F. Watanabe, H. Matsuda, and M. Takada, Enhancement of Chloride Volatilization of Zn, Pb and Cu from Molten Fly Ash under Reduced Pressure, The Society of Chemical Engineers Japan, 32 (2006) 99–102.
- [120] G.F. Naterer, Heat Transfer in Single and Multiphase Systems, Mechanical Engineering Series, CRC Press, 2003
- [121] Y Haseli, G.F. Naterer, I. Dincer, Comparative assessment of greenhouse gas mitigation of hydrogen passenger trains, International Journal of Hydrogen Energy 33 (7) (2008) 1788-1796
- [122] GO Transit Lakeshore Corridor 2031, addendum to April 08, October 20, 2008, Final Report, Toronto
- [123] GO Transit Lakeshore Express Rail Benefits Case, June 2009, Metrolinx. 20 Bay Street, Suite 901, Toronto, ON M5J 2N8
- [124] Alistair I. Miller, Hydrail: An adaptable, Low Cost Alternative to Electrification, Hydrogen and Fuel Cells Conference Vancouver, April 2007.
- [125] J. Marcinkoski, J. P. Kopasz, T. G. Benjamin, Progress in the DOE fuel cell subprogram efforts in polymer electrolyte fuel cells, International Journal of Hydrogen Energy, 33 (14) (2008) 3894-3902
- [126] Rail Safety Standards Board, T 531 Feasibility study into the use of hydrogen fuel – Final Report, Rail Safety and Standards Board, AEA Technology Rail, 2005

- [127] Locomotive Emissions Monitoring Program, Environment Canada, EPS 2/TS/20, 978-09734044-8-7, Catalogue Number EN 49-1/2-17, Railway Association of Canada/Environment Canada 2006
- [128] Air Quality Assessment Report for GO Transit Georgetown, Ortech Environmental, , 804 Southdown Road, Mississauga, ON, L5J 2Y4, April 2009, appendix C1
- [129] M. Balat, Potential importance of Hydrogen as Future Solution to transportation and Environmental Problems, International Journal of Hydrogen Energy 33 (15) (2008) 4013- 4029
- [130] M. Orham, M. Wietschel, The Future of Hydrogen Opportunities and Challenges, International Journal of Hydrogen Energy, 34 (2), (2009) 615-627
- [131] National Renewable Energy Laboratory, Costs of Storing and Transporting Hydrogen, Report number NREL/TP-570-25106, 1998
- [132] The European Hydrogen Train, feasibility study, main report, July 2005-August 2006
- [133] Michael Ball, Martin Wietschel, The future of Hydrogen, opportunities and Challenges, International Journal of Hydrogen Energy, 34 (2) (2009) 615-627
- [134] H. Tsuchiya, O Kobayashi, Mass production cost of PEM fuel cell by learning curve, International Journal of Hydrogen Energy, 29 (2004) 985-990,
- [135] National Research Council, The hydrogen economy, opportunities, constraints, barriers and R&D needs, Committee on Alternatives and Strategies for Future Hydrogen Production, National Academies Press, 2004

- [136] Jones L.E, Hayward G.W, Fuel Cell Alternative for Locomotive Propulsion, International Journal of Hydrogen Energy, 10 (7-8), (1985) 505-516
- [137] Roadmap on Manufacturing R&D for the Hydrogen Economy, Proceedings from the Workshop on Manufacturing R&D for the Hydrogen Economy, Washington, D.C., July 14-15, 2005
- [138] S. Butterworth, AEA Technology Rail, Feasibility Study into the Use of Hydrogen Fuel, Final Report, T531
- [139] Go Transit fleet facts, <http://www.go transit.com/public/en/aboutgo/fleet.htm>
- [140] L.C Brown et al, High Efficiency Generation of Hydrogen Fuels Using Nuclear Power, Nuclear Energy Research Initiative Program, DOI, DE-FG03-99SF21888, June 2003
- [141] Nuclear production of hydrogen, technologies and perspectives for global deployment / International Nuclear Societies Council (INSC), LaGrange Park, Illinois.
- [142] Supply mix advice report, OPA, Dec 2005, 1339 part 1-2, Toronto
- [143] Ontario News room, Move-Ontario 2020, June 15 2007 The cost of congestion, Government of Ontario, Toronto.
- [144] F. Aube, Guide for Computing CO<sub>2</sub> Emissions Related to Energy Use. CANMET, Energy Diversification Research Laboratory.
- [145] W. A. Amos, Costs of Storing and Transporting Hydrogen, National Renewable Energy Laboratory, Report number NREL/TP-570-25106, 1998, Golden, Colorado

- [146] Y Haseli, G.F. Naterer, I. Dincer, Comparative assessment of greenhouse gas mitigation of hydrogen passenger trains, *International Journal of hydrogen Energy*, 33 (7), (2008) 1788-1796
- [147] IESO Weekly Market Report, IESO Customer Relations, Oct 7 - Oct 13, 2009, Independent Electricity System Operator, Toronto
- [148] P. L. Spath, M.K. Mann, Life Cycle Assessment of Hydrogen Production via Natural Gas Steam Reforming, National Renewable Energy Laboratory, Report number NREL/TP-570-27637, 2001, Golden, Colorado